UNIVERSITY OF CALIFORNIA
Santa Barbara

Alternative Approaches to Group IV Thermoelectric Materials

A Dissertation submitted in partial satisfaction
of the requirements for the degree of

Doctor of Philosophy

in

Chemistry

by

Matthew Loren Snedaker

Committee in Charge:

Professor Galen D. Stucky, Chair

Professor Martin Moskovits

Professor Songi Han

Professor Ram Seshadri

March 2015

The Dissertation of
Matthew Loren Snedaker is approved:

Professor Martin Moskovits

Professor Songi Han

Professor Ram Seshadri

Professor Galen D. Stucky, Committee Chairperson

December 2014

Alternative Approaches to Group IV Thermoelectric Materials

by

Matthew Loren Snedaker

"Santa Barbara looked very much as it did when I left it five months before: the long sand beach, with the heavy rollers, breaking upon it in a continual roar, and the little town, imbedded on the plain, girt by its amphitheatre of mountains. Day after day, the sun shone clear and bright upon the wide bay and the red roofs of the houses; everything being as still as death, the people really hardly seeming to earn their sun-light. Daylight actually seemed thrown away upon them."

–R.H. Dana, Jr. *Two Years Before the Mast* (1835)

This thesis is dedicated to my dad, Robert Eric Snedaker

July 14, 1960 – June 18, 2012

to my grandpa, Louis John DeMarco

September 3, 1918 – March 13, 2013

and to my cousin, Nicholas Chase Bornholdt.

January 1, 1989 – May 10, 2013

Acknowledgements

It has been a privilege to work with such modest and generous scientists-engineers, who dedicate their lives to improving our world yet receive little public recognition. Thank you Prof. Galen D. Stucky and Prof. Martin Moskovits for your intellectual and emotional support.

Thank you Prof. Ram Seshadri for opening up your lab to me and hiring the Birkels, who became great friends of mine. Thank you Dr. Christina Birkel for making me appreciate solid state chemistry and crystallography. Thank you Dr. Alex Birkel for the sociopolitical conversations. Thank you Prof. Syed Mubeen and Dr. Sylvia Joun Lee for your friendship, hard work, and modesty. Thank you Prof. Songi Han for being on my committee and the enjoyable TA experiences for your physical chemistry courses.

Thank you Tristan Day and Prof. G. Jeffrey Snyder, of Caltech, for the rewarding collaborations. Thank you to the CEEM Thermoelectrics Group and especially Dr. Ben Curtin, Dr. Peter Burke, Prof. Hong Lu, Dr. Alex Sztein, Dr. Rachel Koltun, Prof. Gossard, Prof. Bowers, and Prof. Palmstrøm for teaching me how to measure and analyze thermoelectrics.

Thank you Deryck Stave, John English, Dr. Stephan Kraemer, and Dr. Tom Mates for your technical expertise and enthusiastic problem-solving personalities.

Thank you to Dr. Lauren Misch, Dr. Kim See, Jason Douglas, Michael Gaultois, Sara Nownes, and Damien Kudela. Thank you to the members of the Stucky Group & and the Moskovits Group for your support.

Thank you to my friends that I've made in Santa Barbara. Thank you to KCSB-FM. Thank you to everybody that has provided me with the opportunity to be here. Thank you DOE CEEM for the financial support and Graduate Division for the fellowship.

Thank you to my family for their sacrifices and their love that made me who I am today.

Matthew Loren Snedaker

Background

Born (Fontana) and raised (Rancho Cucamonga) in California.

Education

Ph.D. in Chemistry, University of California Santa Barbara, *expected* January 2015.

Advisors: Galen D. Stucky & Martin Moskovits

GPA: 3.97/4.00

B.S. in Chemical Physics, Revelle College: University of California San Diego, June 2009.

Advisor: Michael J. Sailor

Graduate Research

Thermoelectric Properties of Silicon Germanium Alloys Prepared from the Magnesiothermic Reduction of Silica-Germania Nanocomposites, 2009–present

Undergraduate Research

Porous Silicon-Based Remote Chemical Sensors on an Airborne Platform, 2008–2009

Gold–Decorated Porous Silicon for Sensing of Thiols, 2008–2009

Porous Silicon Rugate Filters for Sensing of Volatile Organic Compounds, 2007–2008

Honors & Awards

Graduate Division Dissertation Fellowship, 2014

Revelle College Provost's Honors: Winter 2008, Spring 2008, Winter 2009, Spring 2009

Chancellor's Research Scholarship, 2008

Governor's Scholars Award, 2005

Publications

Y-S. Jun, **M. L. Snedaker**, D. T. Horvath, B. Wu, G. D. Stucky. High Capacity Silica-Germania Nanocomposite Batteries. (in preparation)

H. Wang, J. Hwang, **M. L. Snedaker**, I. Kim, C. Kang, J. Kim, G. D. Stucky, J. Bowers, W. Kim. High Thermoelectric Performance of a Heterogeneous Nanocomposite. (submitted)

K. Ding, H. Lu, Y. Zhang, **M. L. Snedaker**, D. Liu, J. A. Maciá-Agulló, G. D. Stucky. Microwave Synthesis of Microstructured and Nanostructured Metal Chalcogenides from Elemental Precursors in Phosphonium Ionic Liquids. *J. Am. Chem. Soc.* (published online 21 October 2014) [DOI: 10.1021/ja508628q]

Y. Zhang, J. Bahk, J. Lee, C. S. Birkel, **M. L. Snedaker**, D. Liu, H. Zeng, M. Moskovits, A. Shakouri, G. D. Stucky. Hot carrier filtering in solution processed hetero-structures: a paradigm for improving thermoelectric efficiency. *Adv. Mater.* (published online 28 January 2014) [DOI: 10.1002/adma.201304419]

M. L. Snedaker, Y. Zhang, C. S. Birkel, H. Wang, T. Day, Y. Shi, X. Ji, S. Kraemer, C. E. Mills, A. Moosazadeh, M. Moskovits, G. J. Snyder, G. D. Stucky. Silicon-based thermoelectrics made from a boron-doped silicon dioxide nanocomposite. *Chem. Mater.* **25**, 4867-4873 (2013). [DOI: 10.1021/cm401990c]

Y. Zhang, T. Day, **M. L. Snedaker**, H. Wang, S. Kraemer, C. S. Birkel, X. Ji, D. Liu, G. J. Snyder, G. D. Stucky. Mesoporous anisotropic n-type Bi_2Te_3 monolith with low thermal conductivity as an efficient thermoelectric material. *Adv. Mater.* **24**, 5065-5070 (2012). [DOI: 10.1002/adma.201201974]

C. S. Birkel, W. G. Zeier, J. E. Douglas, B. R. Lettiere, C. E. Mills, G. Seward, A. Birkel, **M. L. Snedaker**, Y. Zhang, G. J. Snyder, T. M. Pollock, R. Seshadri, G. D. Stucky. Rapid microwave preparation of thermoelectric TiNiSn and TiCoSb half-Heusler compounds. *Chem. Mater.* **13**, 2558-2565 (2012). [DOI: 10.1021/cm3011343]

Y. Zhang, **M. L. Snedaker**, C. S. Birkel, M. Syed, X. Ji, Y. Shi, D. Liu, X. Liu, M. Moskovits, G. D. Stucky. Silver based intermetallic heterostructures in Sb_2Te_3 thick films with enhanced thermoelectric power factors. *Nano Lett.* **12**, 1075-1080 (2012). [DOI: 10.1021/nl204346g]

Y. Zhang, H. Wang, S. Kraemer, Y. Shi, F. Zhang, **M. L. Snedaker**, K. Ding, M. Moskovits, G. J. Snyder, G. D. Stucky. Surfactant-free synthesis of Bi_2Te_3–Te micro–nano heterostructure with enhanced thermoelectric figure of merit. *ACS Nano* **5**, 3158-3165 (2011). [DOI: 10.1021/nn2002294]

Poster Presentations

American Chemical Society National Meeting, San Diego, CA, March 2012

Materials Research Outreach Symposium, Santa Barbara, CA, January 2012

UCSD ACS–SA Undergraduate Research Symposium, La Jolla, CA May 2009

American Chemical Society National Meeting, Salt Lake City, UT, March 2009

Teaching

Research Mentor at Center for Energy Efficient Materials, UCSB

Mentored Armin Moosazadeh, a Mechanical Engineering student, in his undergraduate research (January 2011–September 2011).

Mentored Nicholas Harvey, a Chemistry student, in his undergraduate research (June 2013–August 2013).

Teaching Assistant at University of California, Santa Barbara

Upper-Division Physical Chemistry sequence– Thermodynamics (Fall 2009), Quantum Chemistry (Winter 2010), Statistical Mechanics & Kinetics (Spring 2010), Solid State Chemistry (Fall 2012)

Teaching Assistant at University of California, San Diego

General Chemistry sequence, Spring 2007– Spring 2009

Extracurricular Activities

KCSB 91.9 FM in Santa Barbara, Winter 2013 – Spring 2014.

Programmed a weekly show that included discussion of UCSB's science research breakthroughs along with emerging hip hop and electronic music and I produced PSA's.

Vice President of Outreach, American Chemical Society– Student Affiliates, University of California San Diego, 2008–2009.

Organized demonstrations at local, disadvantaged schools and community events including the Sally Ride Festival. Prepared the chemistry demonstrations, organized volunteers, and insured that viewers had fun learning about chemistry. Established a mentor-mentee program to increase undergraduate involvement and improve the academic experience for chemistry majors.

Miscellaneous

Computer Skills

Microsoft Office Suite, *Mathematica*, Origin, LaTeX, Adobe Photoshop, Gimp, L-Edit, PyGSAS.

Technical Skills

Cleanroom experience, basic circuitry, licensed amateur radio operator (KG6CCC).

Abstract

Alternative Approaches to Group IV Thermoelectric Materials

Matthew Loren Snedaker

In the pursuit of energy efficiency, there is a demand for systems capable of recovering waste heat. A temperature gradient across a thermoelectric material results in the thermal diffusion of charge carriers from the hot side to the cold side, giving rise to a voltage that can be used to convert waste heat to electricity. Silicon germanium (SiGe) alloys are the standard materials used for thermoelectric generators at high temperatures.

We report an alternative method for preparing p-type $Si_{1-x}Ge_x$ alloys from a boron-doped silica-germania nanocomposite. This is the first demonstration of the thermoelectric properties of SiGe–based thermoelectrics prepared at temperatures below the alloy's melting point through a magnesiothermic reduction of the $(SiO_2)_{1-x}(GeO_2)_x$. We observe a thermoelectric power factor that is competitive with the literature record for the conventionally prepared SiGe. The large grain size in our hot pressed SiGe limits the thermoelectric figure of merit to 0.5 at 800 °C for an optimally doped p-type $Si_{80}Ge_{20}$ alloy.

A phosphorus-doped oxide can yield n-type $Si_{1-x}Ge_x$; however, the current processing method introduces a background boron content that compensates ~10% of the donor impurities and limits the thermoelectric power factor.

Spark plasma sintering of the nano-$Si_{1-x}Ge_x$ yields a heterogeneous alloy with thermal conductivity lower than that of the hot pressed homogeneous alloy due to a reduction in the average crystallite size. Magnesiothermic reduction in the presence of molten salts allows some control over crystallite growth and the extent of Si–Ge alloying.

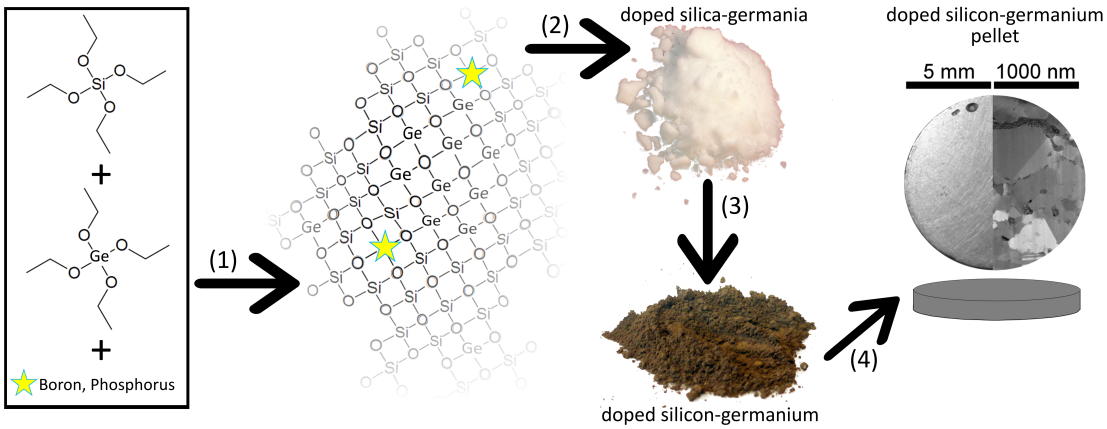

Figure 0.1: Synthesis and processing scheme to yield a pellet for thermoelectric characterization: (1)–(2) The sol-gel synthesis of a doped silica-germania nanocomposite, (3) magnesiothermic reduction to a doped silicon-germanium nanocomposite, (4) consolidation into a doped silicon-germanium pellet by hot pressing or spark plasma sintering.

Contents

List of Figures

List of Tables

Chapter 1

An introduction to thermoelectrics

1.1 The heat engine

The combustion of fossil fuels for power generation is an inefficient process, introducing waste heat into the environment well beyond the energy premium predicted by thermodynamics for an ideal Carnot engine. In the pursuit of energy efficiency, the demand for systems capable of recovering waste heat is increasing.

Figure 1.1 shows a schematic of a heat engine which produces work (W) due to the differential in thermal energy of a reservoir at high temperature (T_H) and a reservoir at a colder temperature (T_C). In the theoretical thermodynamic cycle shown in the temperature–entropy diagram (Figure 1.2), the system is always in a state that is totally reversible to a previous state. This perfect cycle is called the Carnot cycle and a heat engine that follows this cycle is called a Carnot engine.

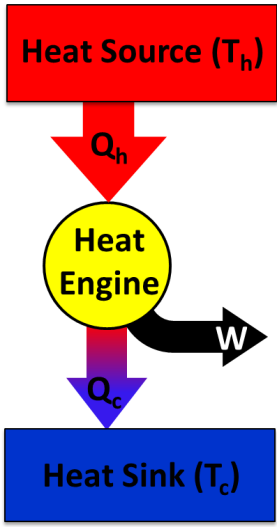

Figure 1.1: Schematic of a heat engine.

The efficiency of a heat engine is defined by the ratio of work output (W) to heat flow into the engine (Q_H), as shown in equation 1.14. Calculating the work done by the Carnot engine during the Carnot cycle and the heat flow into the Carnot engine, we obtain the efficiency of the Carnot cycle shown in equation 1.8.

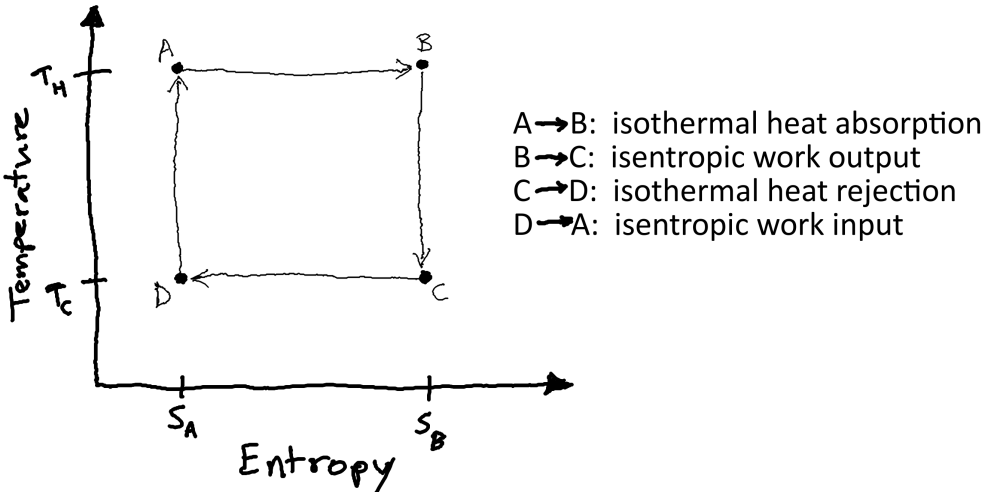

Figure 1.2: The Carnot cycle.

$$\eta \equiv \frac{W}{Q_H} \tag{1.1}$$

$$W_{Carnot} = \oint (dQ - dU) \tag{1.2}$$

$$= \oint dQ \tag{1.3}$$

$$= \oint T\ dS \tag{1.4}$$

$$= (T_H - T_C)(S_B - S_A) \tag{1.5}$$

$$Q_H = \int_A^B T\ dS \tag{1.6}$$

$$= T_H\ (S_B - S_A) \tag{1.7}$$

$$\eta_{Carnot} = \frac{T_H - T_C}{T_H} \tag{1.8}$$

Real heat engines stray from the totally reversible cycle that the Carnot cycle idealizes because heat is lost to the surroundings; thus, a real heat engine performs less work than a Carnot engine and the efficiency of a real heat engine is always less than the efficiency of a Carnot engine.

1.2 The thermoelectric effects

1.2.1 The Seebeck effect

In 1821, Thomas Johann Seebeck observed the deflection of a compass needle from a closed loop of two metals, when there was a temperature difference between

the two junctions. Seebeck incorrectly believed that this was a thermomagnetic effect; however, Hans Christian Ørsted identified that there was a thermally induced voltage and current involved and so the first thermoelectric effect was discovered. A temperature gradient across a material results in the thermal diffusion of charge carriers from the hot side to the cold side, giving rise to an open-circuit voltage (ΔV) that is proportional to the temperature difference (ΔT), as described by the Seebeck coefficient (α) in equation 1.9:

$$\alpha = -\frac{\Delta V}{\Delta T} . \tag{1.9}$$

1.2.2 The Peltier effect

In 1834, Charles Athanase Peltier observed that a current flow flow between two dissimilar materials generated a temperature difference at the junction of the materials. This effect is called the Peltier effect, where the heat flux ($\dot{Q}$) is proportional to the applied current (I) by the difference of Peltier coefficients (Π) of the materials in contact:

$$\dot{Q} = (\Pi_1 - \Pi_2)\, I . \tag{1.10}$$

The Peltier effect allows heat to be pumped to or away from a junction of dissimilar materials.

1.2.3 The Thomson effect

In 1854, William Thomson (aka Lord Kelvin) discovered that an electrical conductor that has a temperature gradient will have a gradient in the Seebeck coefficient that is proportional to the temperature by the Thomson coefficient (τ):

$$\tau = T \left(\frac{d\alpha}{dT} \right) . \tag{1.11}$$

1.2.4 The caveat

Lord Kelvin was able to establish relations between the three thermoelectric effects. The Thomson relations are:

$$\tau = \frac{d\Pi}{dT} - \alpha \tag{1.12}$$

and

$$\Pi = T \, \alpha \ . \tag{1.13}$$

The Thomson relations connect a material's heat transport properties to its charge transport properties, which allow thermoelectrics to be used as heat engines; however, the transport processes that connect heat current to charge current are interrelated and place limitations on the maximum efficiency of a thermoelectric heat engine.

1.3 Thermoelectrics as heat engines

NASA has successfully employed radioisotope thermoelectric generators (RTGs) for power generation in their space missions, where alternative power generation methods are not viable.[1] The RTGs employ $^{238}PuO_2$ as their heat source and the coldness of space (or Mars) as the sink.

Figure 1.3a shows how the Seebeck coefficient for a material may be evaluated and Figure 1.3b shows one configuration for a thermopile and thermoelectric module, where the thermopile is an n-type (i.e. electron conducting) semiconductor and a p-type (i.e. hole conducting) semiconductor that are electrically in series but thermally in parallel. The existence of a temperature gradient, results in the diffusion of the charge carriers from the hot side to the cold side, giving rise to a current and voltage, which are delivered as power to the load that is connected to the thermoelectric device. By the Peltier effect, the opposite may occur too, where an applied current may produce a temperature gradient useful for refrigeration applications.

1.3.1 Efficiency of a thermoelectric power generator

The efficiency of the conversion process in a thermoelectric power generator has been discussed by Nolas et al. [2] and Curtin [3]. The efficiency is expressed

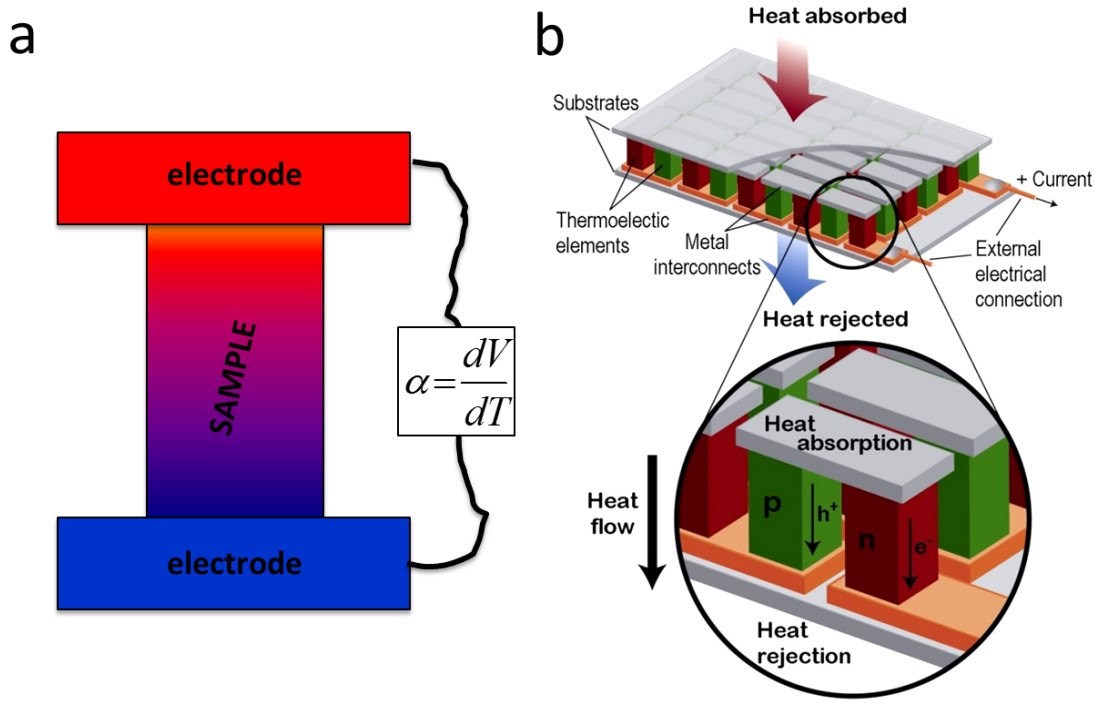

Figure 1.3: Schematic of a thermopile and thermoelectric device: (a) The Seebeck coefficient for a material and (b) a thermopile and thermoelectric device (Reprinted by permission from Macmillan Publishers Ltd: *Nature Materials*, Ref. [1], Copyright 2008. doi:10.1038/nmat2090).

by equation 1.15:

$$\eta \equiv \frac{W}{Q_H} \tag{1.14}$$

$$= \frac{\alpha^2 \ (\Delta T)^2 \left(\frac{R_L}{R_L + R_{TE}} \right)}{\kappa \ \Delta T + I \ \alpha \ T_H - \frac{1}{2} I^2 \ R_{TE}} \ , \tag{1.15}$$

where R_L is the load resistance, R_{TE} is the resistance of the thermoelectric material, ΔT is the temperature drop across the thermoelectric (i.e. $\Delta T = T_H - T_C$),

and κ is the material's thermal conductivity. If equation 1.15 is maximized with respect to the current, then the maximum efficiency of the thermoelectric power generator is:

$$\eta_{max} = \frac{T_H - T_C}{T_H}\left(\frac{\sqrt{1+zT_{ave}}-1}{\sqrt{1+zT_{ave}}-T_C/T_H}\right) , \tag{1.16}$$

where the prefactor is the Carnot efficiency, $T_{ave} = \frac{1}{2}(T_H - T_C)$, and z is a dimensionless quantity that is useful for discussing the thermoelectric conversion efficiency of a material.

The thermoelectric figure of merit, zT

The product of z and the absolute temperature (T), are referred to as the thermoelectric figure of merit, zT:

$$zT = \frac{\alpha^2\,\sigma}{\kappa}T \ . \tag{1.17}$$

Efficiency: thermoelectrics vs. mainstream heat engines

Vining compared the standard heat engine efficiencies to a model thermoelectric heat engine operating at different zT's. An adaptation of his comparison is shown in Figure 1.4. The zT improvements necessary to make thermoelectrics competitive with the standard heat engines used in power generation are extremely challenging. Improving the figure of merit is a significant materials engineering problem due to the interdependence of these properties.

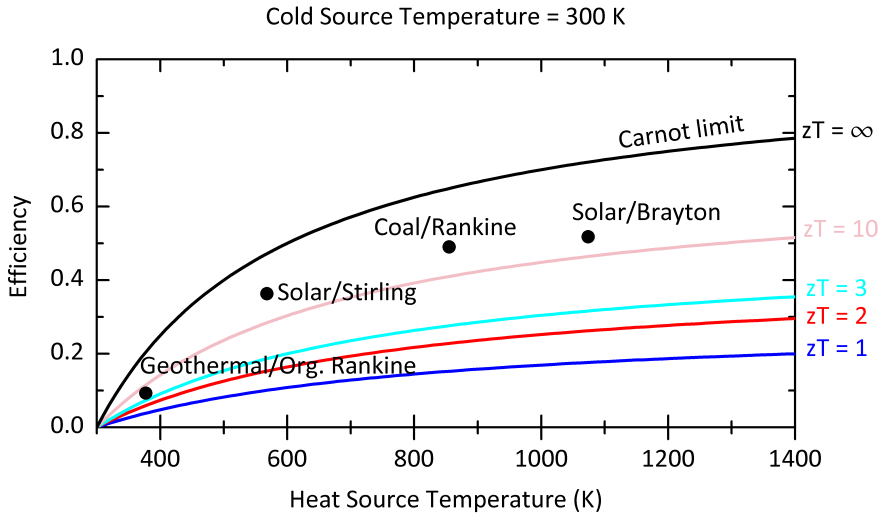

Figure 1.4: Heat engine efficiencies and zT requirement. (Reprinted by permission from Macmillan Publishers Ltd: *Nature Materials*, Ref. [4], Copyright 2009. doi:10.1038/nmat2361)

1.3.2 Interdependence of the material properties in zT

We see that the efficiency of a thermoelectric power generator (and a thermoelectric refrigerator) is dependent upon the material's Seebeck coefficient, electrical conductivity, and thermal conductivity. To maximize the thermoelectric conversion efficiency, the material must approach the behavior of a phonon-glass, electron-crystal, where the thermal conductivity is low and the charge transport is like that in a crystal. It is a challenge to realize a phonon-glass, electron-crystal because as seen in Figure 1.5 from Snyder and Toberer since the power factor ($\alpha^2\ \sigma$) is maximized at a different carrier density than that of the zT– the material properties that define zT are interdependent.

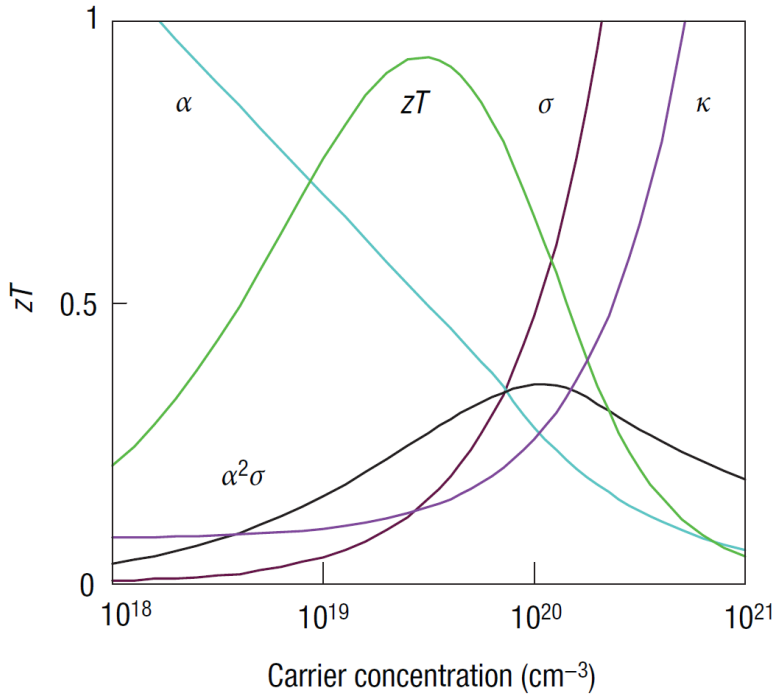

Figure 1.5: Thermoelectric properties for a model of Bi_2Te_3. (Reprinted by permission from Macmillan Publishers Ltd: *Nature Materials*, Ref. [1], Copyright 2008. doi:10.1038/nmat2090)

The electrical conductivity

The electrical conductivity describes how well a material conducts charge. It is the reciprocal of the electrical resistivity ($\rho = \sigma^{-1}$), which is defined as:

$$\rho \;=\; R\,\frac{A}{l} \quad , \tag{1.18}$$

where R is the resistance measured between the electrical contacts, A is the cross sectional area, and l is the distance between the electrical contacts. The electrical

conductivity depends on the carrier density (n) and carrier mobility (μ):

$$\sigma = n\, e\, \mu \quad . \tag{1.19}$$

The thermal conductivity

The thermal conductivity describes how well a material conducts heat; however, the heat is transported by lattice vibrations known as phonons as well as the charge carriers themselves. Thus, the total thermal conductivity is:

$$\kappa = \kappa_{ph} + \kappa_{el} \tag{1.20}$$

$$= \kappa_{ph} + \sigma\, L\, T \quad , \tag{1.21}$$

where κ_{ph} and κ_{el} are the lattice and electronic contributions to the thermal conductivity in equation 1.20 and the Wiedemann-Franz Law (i.e. $\kappa_{el} = \sigma\, L\, T$), where L is the Lorenz number, yields equation 1.21, showing the interdependence between electrical conductivity and thermal conductivity.

The lattice thermal conductivity may be significantly reduced by increasing the phonon scattering rate by one of the mechanisms shown in Figure 1.6a. These phonon scattering processes affect the phonon mean free path distribution, such that point defect scattering reduces the number of phonons that have very short mean free paths and phonon scattering at grain boundaries disrupts the phonon number at a larger mean free path– the consequence is that the number of phonons

and integral of the curve in 1.6b is changed and the lattice thermal conductivity decreases. The introduction of boundaries and other phonon scattering mecha-

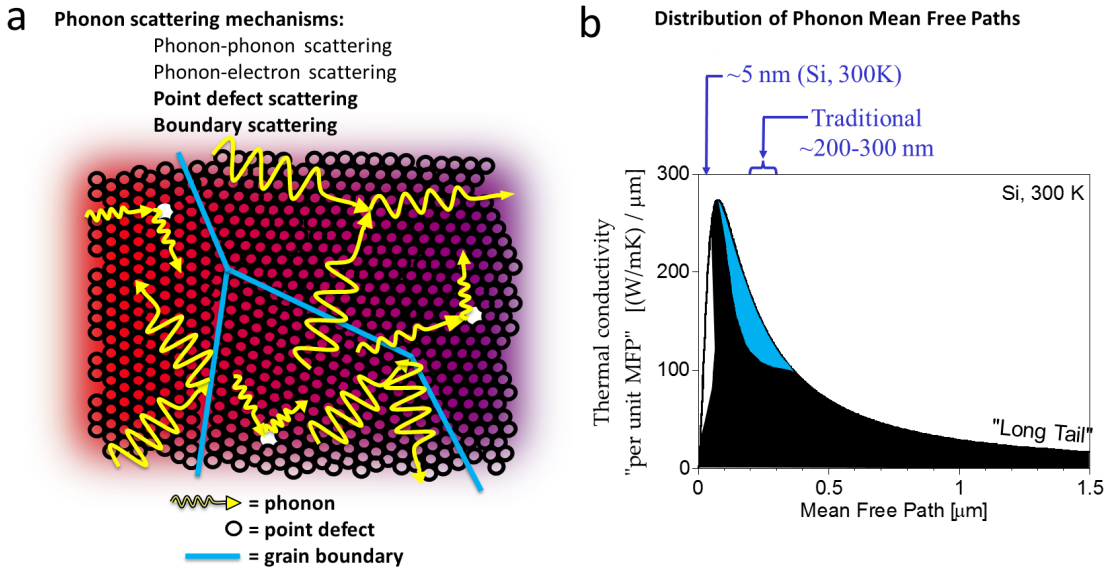

Figure 1.6: (a) The introduction of point defects and boundaries leads to increased phonon scattering and (b) reduction in total lattice thermal conductivity (figure adapted from Dames [5], with permission).

nisms isn't always best for maximizing zT since those scattering mechanisms may exist on a length scale that affects the charge carrier transport too. For a thorough discussion of the phonon mean free path distribution and how it affects thermal conductivity, the reader is referred to Dames [5] and Rowe [6].

The Seebeck coefficient

Using what we just learned about thermal conductivity, the thermoelectric figure of merit may be expressed as equation 1.24:

$$zT = \frac{\alpha^2\ \sigma\ T}{\kappa_{ph} + \kappa_{el}} \tag{1.22}$$

$$= \frac{\alpha^2\ \sigma\ T}{\kappa_{ph} + \sigma\ L\ T} \tag{1.23}$$

$$= \frac{\alpha^2\ /\ L}{1 + \kappa_{ph}/\kappa_{el}}\ . \tag{1.24}$$

Improving the figure of merit is a significant materials engineering problem due to the interdependence of the properties. Most recent advances in improving thermoelectric efficiency have resulted from nanostructuring the material, which leads to a reduction of the lattice thermal conductivity without significantly decreasing the charge mobility.[1] However, the Seebeck coefficient greatly affects the zT.

Microscopically, the Seebeck coefficient is related to the entropy per charge carrier. It may also be expressed by the Mott Formula shown in equation 1.25 and in the expanded form 1.26:

$$\alpha = \frac{\pi^2\ k_B^2}{3\ e} T \left\{ \frac{d[ln(\sigma(E)]}{dE} \right\}_{E=E_F} \tag{1.25}$$

$$= \frac{\pi^2\ k_B^2}{3\ e} T \left\{ \frac{1}{n}\frac{d\ n(E)}{dE} + \frac{1}{\mu}\frac{d\ \mu(E)}{dE} \right\}_{E=E_F}\ , \tag{1.26}$$

where k_B is the Boltzmann constant, e is the elementary charge, $\sigma(E)$ is the energy dependent electrical conductivity, and E_F is the Fermi energy. The Mott formula accurately describes metals and degenerate semiconductors and captures the interdependence of the Seebeck coefficient and electrical conductivity. Generally, an increase in electrical conductivity due to doping will decrease the Seebeck coefficient.

1.3.3 The benchmark thermoelectric materials

In "Complex thermoelectric materials", Snyder and Toberer show the temperature dependence of the zT of commercially available, bulk thermoelectric materials (see Fig. 1.7).

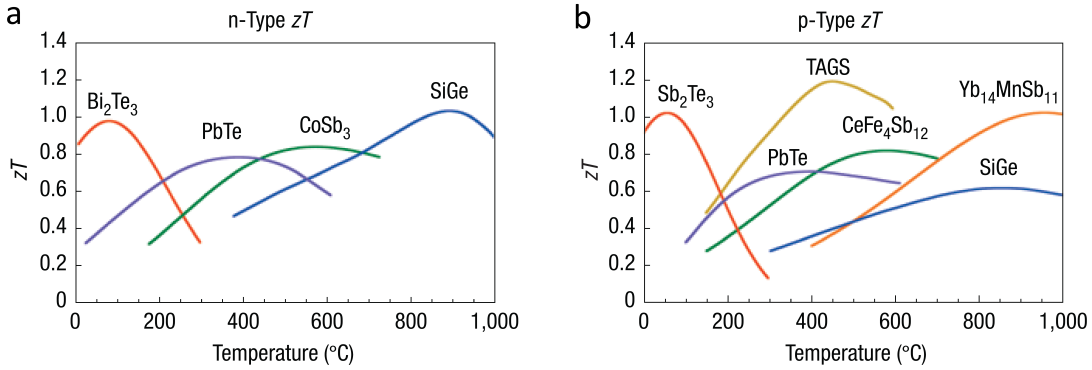

Figure 1.7: The state-of-the-art commercial (a) n-type and (b) p-type thermoelectric materials and some developed by NASA for their radioisotope thermoelectric generators. (Reprinted by permission from Macmillan Publishers Ltd: *Nature Materials*, Ref. [1], Copyright 2008. doi:10.1038/nmat2090)

Silicon germanium alloys ($Si_{1-x}Ge_x$) are the standard materials used for thermoelectric generators at high temperatures. Two appealing advantages of these $Si_{1-x}Ge_x$ alloys are that silicon is the second-most earth abundant element (see Fig. 1.8.[7]); and both silicon and germanium are less toxic than other heavy metals commonly used in thermoelectrics. However, the zT's of the $Si_{80}Ge_{20}$ RTG's used by NASA in the past were limited to 0.5 (p-type) and 1.0 (n-type). New materials or new effects must be discovered and studied in order to improve the efficiency of thermoelectric heat engines.

1.4 Paradigm shifts in thermoelectrics

The functionality of a material/device can be attributed to the properties of the material under the effect of some perturbation, as is highlighted in Figure 1.9. An example of a perturbative effect that gives rise to enhanced functionality is the existence of topological insulators, where the bulk of the material is electrically insulating; however, at the proper dimension and composition, the material/device exhibits electrical conduction at the material's surface.[8–10]

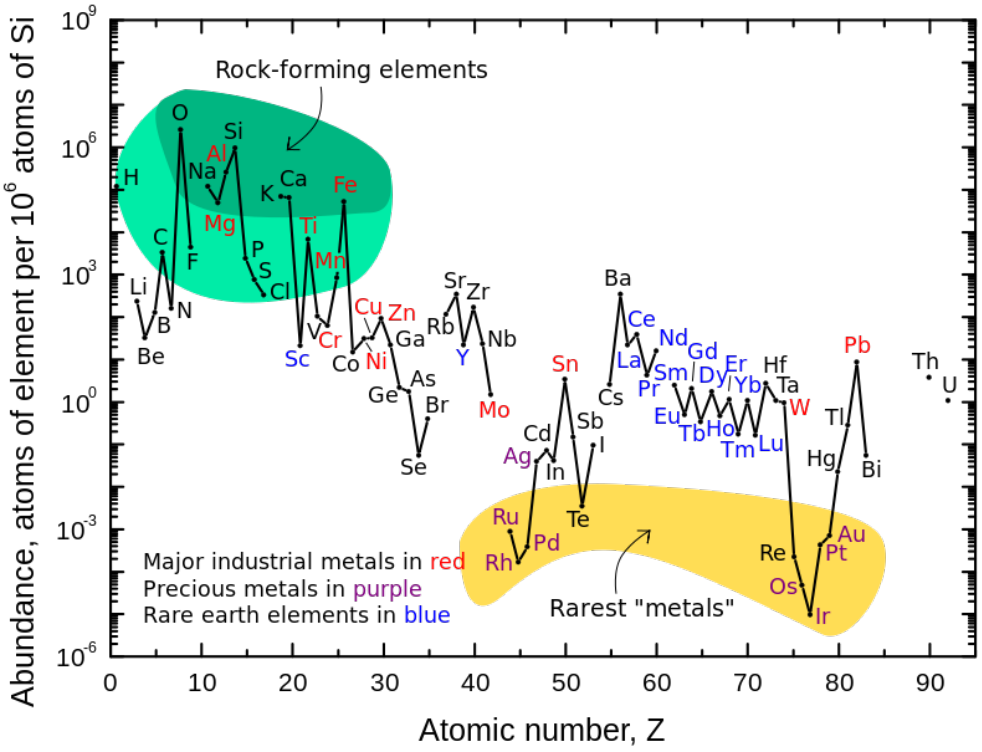

Figure 1.8: The crustal abundance of the elements. (Figure taken from Wikipedia, with permission under a Creative Commons Copyright 2003 Haxel et al. [7].)

1.4.1 Nanostructuring to reduce lattice thermal conductivity

A variety of synthetic strategies have been developed for silicon-based alloys in order to improve the figure of merit and reduce cost.[11–15] In general, the thermoelectric efficiency of the materials can be improved by increasing nanostructuring to enhance phonon scattering to decrease the thermal conductivity,[16, 17] and the cost is reduced by minimizing the germanium content.[18, 19] High energy

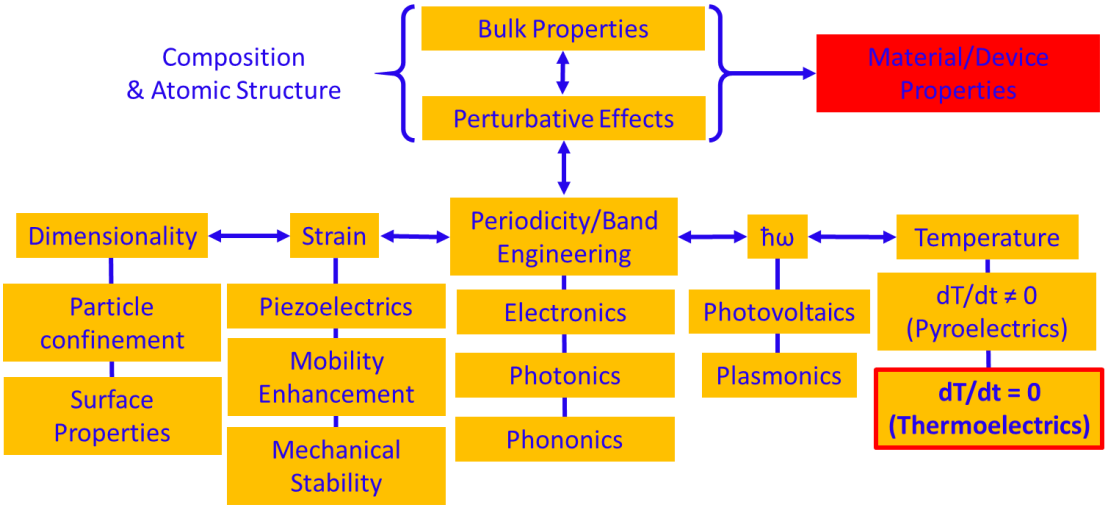

Figure 1.9: Bulk properties and some perturbative effects that give rise to enhanced functionality.

ball milling of a mixture of elemental silicon, germanium, and the dopant element in order to decrease the average particle size and the thermal conductivity has been demonstrated to give the highest figure of merit for bulk nanostructured SiGe thermoelectric materials of 1.3 and 0.95 at 900 °C, for n-type and p-type respectively.[20, 21]

However, the ball milled nanocomposites were prepared from relatively costly metallurgical-grade silicon and germanium made through high temperature (~2000 °C) carbothermal reduction of high purity silica and a similar reduction process of germania. Therefore, an alternative strategy to obtain nanostructured

SiGe particles directly from nanostructured oxides at low temperature is highly desirable.

The successful demonstration of lattice thermal conductivity reduction in nanostructured silicon has been shown in nanowires (see Fig. 1.10) [22, 23], and extended to silicon nanomeshes[24] and Si nanowire arrays[25, 26].

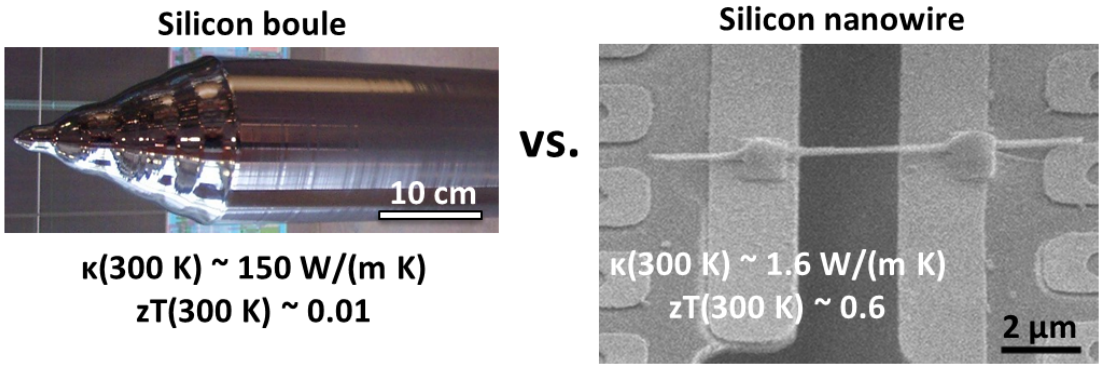

Figure 1.10: A silicon nanowire's thermal conductivity may be reduced two orders of magnitude lower than that of a bulk single crystal, making nano-Si a more efficient thermoelectric than bulk-Si. (Fig. 1.10a adapted from Wikimedia Commons, Creative Commons Copyright 2004 Stahlkocher [27] and Fig. 1.10b reprinted by permission from Macmillan Publishers Ltd: *Nature*, Ref. [22], Copyright 2008. doi:10.1038/nature06381)

Porous thermoelectrics

Porous semiconductors have been proposed as the ideal phonon-glass, electron-crystal. Calculations by Lee et al. suggest that nanoporous Si should exhibit a zT that is two orders of magnitude greater than thatthat of bulk Si and that

nanoporous Ge should exhibit a zT that is thirty times greater than the zT of bulk Ge.[28, 29]. Somewhat encouraging is that there are porous semiconductors or semiconductors that exhibit cage-like structures (e.g. the clathrates), which have been shown to have $zT > 1.3$. However, the effect of porosity may be detrimental in a nanograined material, where the phonons are limited by the grain boundary scattering and additional defects would cause a degradation of the charge mobility. Lee et al. argue that nanoscale porosity is not beneficial in bulk $Si_{1-x}Ge_x$ nanocomposites because the benefit in reducing lattice thermal conductivity is insufficient to overcome the deficit in electrical conductivity.[30]

Isotopic phononic crystals

Yang et al. calculated that a nanoscale 3D isotopic phononic crystal of silicon should yield a $zT > 1$; however, the ability to control the isotope assembly appears to be a huge obstacle.[31] A bottom-up process like the method developed in this thesis may offer an opportunity to prepare such a 3D isotopic phononic crystal.

Embedded "Nanoparticle-in-Alloy"

Mingo et al. calculated the zT for a variety of particle-matrix nanocomposites and reported that a SiGe matrix with ~1% volume fraction of silicide nanoinclu-

sions may have a room temperature zT greater than 0.5 and a zT of 1.7 or higher at 900 K.[32]

1.4.2 Power factor ($\alpha^2\ \sigma$) enhancement

Since the Seebeck coefficient is squared in the zT equation, changes in its value can have a dramatic impact. If we consider the Mott equation for the Seebeck coefficient of a metal as shown in equation 1.27 and expanded in equation 1.28, then we see that the Seebeck coefficient is sensitive to how the Fermi function changes at the Fermi level.

$$\alpha \propto \left\{ \frac{d[ln(\sigma(E)]}{dE} \right\}_{E=E_F} \tag{1.27}$$

$$\propto \left\{ \frac{1}{n}\frac{d\ n(E)}{dE} + \frac{1}{\mu}\frac{d\ \mu(E)}{dE} \right\}_{E=E_F} \tag{1.28}$$

This dependence has been used to improve the thermoelectric power factor by several different (but related) mechanisms.

Distortion of the electronic density of states

Heremans et al. doped PbTe with thallium, which introduces an impurity state that distorts the electronic density of states and the energy derivative in the equations above, resulting in $zT = 1.5$ at 773 K.[33]

Modulation doping in silicon germanium to enhance power factor

If a doped material is interfaced with an undoped material, then charge may transfer to the undoped region and since the undoped region has a higher charge mobility, there may be an enhancement in the power factor. Modulation doping has been employed as a means to enhance the power factor ($\alpha^2\ \sigma$) without significantly increasing the thermal conductivity, yielding zT of 1.3 for p-type at 900 °C.[34, 35] This is similar to the field effect, which has been used to improve the thermoelectric power factor in Si-based nanowires.[36–38]

Energy filtering in heterostructured thermoelectrics

Zide et al. demonstrated enhanced Seebeck coefficients in $In_{0.53}Ga_{0.47}As/In_{0.53}Ga_{0.28}Al_{0.19}As$ superlattices, which they attribute to energy filtering, where the low energy carriers are blocked and the higher energy carriers are transported, producing a lower electrical conductivity but an increase in the derivative of the conductivity with respect to energy.[39] The concept of energy filtering has also been used to explain the thermoelectric properties of highly-doped nanograined semiconductors.[40]

Mobility enhancement and the hole gas in Si/Ge heterostructures

Strain has a dramatic impact on the band structure in $Si_{1-x}Ge_x$. Van de Walle and Martin calculated the band alignment for the Si/Ge system and since then the effect of strain to enhance mobility has been used by Intel.[41] The Ge/Si heterostructure can also result in the confinement of a hole gas to the germanium phase, which without any dopants, gives rise to enhanced conductance.[36, 42–44] This property may be useful for thermoelectrics because ionized impurity scattering is the dominant scattering mechanism which degrades charge mobility in degenerately doped $Si_{1-x}Ge_x$.

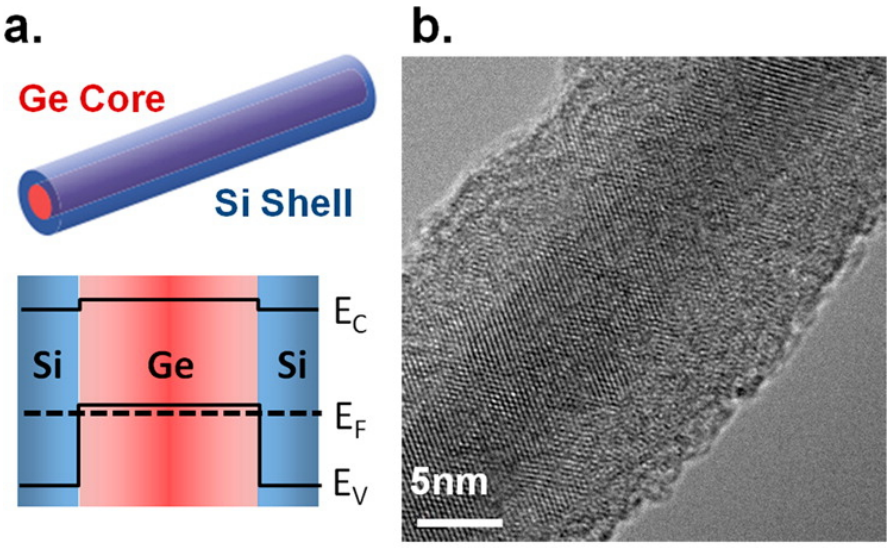

Figure 1.11: The 1D hole gas in Ge/Si nanowire heterostructures: (a) model of the wire's cross section and band offsets in the heterostructure, which confine a hole gas to the germanium core, and (b) HR-TEM image of the Ge/Si nanowire. (Reprinted with permission from Moon et al. [36]. Copyright 2013 American Chemical Society)

1.5 The structure of this thesis

The goal of this thesis is to demonstrate an alternative method to prepare silicon germanium nanocomposites and alloys and to develop doping strategies such that structures like that shown in Figure 1.12, which can't be realized under the extreme conditions currently used to make bulk-$Si_{1-x}Ge_x$, may be realized. This

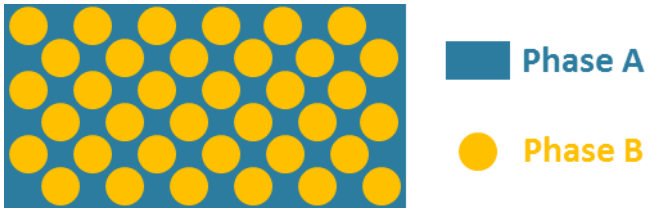

Figure 1.12: Model of a heterostructured nanocomposite (adapted, with permission, from Zhang [45]).

thesis is structured to introduce the concepts and properties that govern thermoelectric transport and then it goes in chronological order of the experiments that I performed from investigating porous silicon films, which had poor electrical properties to the magnesiothermic reduction of doped-$(SiO_2)_{1-x}(GeO_2)_x$ nanocomposites, which exhibit better electrical properties. The processing steps from sol-gel synthesis, to reduction conditions, to powder consolidation conditions all affect the microstructure and homogeneity of the $(Si)_{1-x}(Ge)_x$. Finally, I propose a hybrid organic-inorganic heterostructured thermoelectric that may demonstrate enhanced power factor, using some of the methods developed in this thesis.

Chapter 2

The silicon–germanium system

2.1 Industrial production of metallurgical-grade silicon and germanium

Metallurgical grade (i.e. >98% purity) silicon is prepared by the carbothermal reduction of high purity silica in an electric arc furnace at temperatures around ~2000 °C, as shown in the reactions starting at equation 2.1. The liquid silicon that is collected may be processed further to yield higher purity silicon and single crystals of large diameter may be grown to feed the semiconductor industry.

$$\mathrm{SiO_2\ (s) + 2\ C\ (s)} \xrightarrow{\sim 2000\ ^\circ\mathrm{C}} \mathrm{Si\ (l) + 2\ CO\ (g)} \tag{2.1}$$

$$\mathrm{SiO_2\ (s) + C\ (s)} \xrightarrow{\sim 2000\ ^\circ\mathrm{C}} \mathrm{SiO\ (l) + CO\ (g)} \tag{2.2}$$

$$\mathrm{SiO\ (l) + 2\ C\ (s)} \xrightarrow{\sim 2000\ ^\circ\mathrm{C}} \mathrm{SiC\ (s) + CO\ (g)} \tag{2.3}$$

$$\mathrm{2\ SiC\ (s) + SiO_2\ (l)} \xrightarrow{\sim 2000\ ^\circ\mathrm{C}} \mathrm{3\ Si\ (l) + 2\ CO\ (g)} \tag{2.4}$$

Germanium may be produced by a hydrogen reduction or a carbothermal reduction of a high purity germania. Silicon germanium crystals may be grown; however their size and homogeneity is limited due to the properties of this system's phase diagram (see Fig. 2.2).

2.2 The crystal structure

Silicon crystallizes in the diamond cubic crystal structure, which is two interpenetrating face-centered cubic sublattices. Figure 2.1 shows the unit cell for the diamond cubic crystal structure. The lattice constant of crystalline silicon (c-Si) is 5.431 Å. Silicon can also be deposited as an amorphous or poylcrystalline phase. The lattice constant of c-Ge is 5.658 Å. Germanium may substitute for silicon, which leads to an increase in the lattice constant.

2.3 The phase diagram

Silicon and germanium are completely miscible and may form a solid solution (i.e. an alloy), as seen in Figure 2.2. The large liquidus-solidus region and difference in melting points of the pure phases make it difficult to obtain large, homogeneous $Si_{1-x}Ge_x$ single crystals.

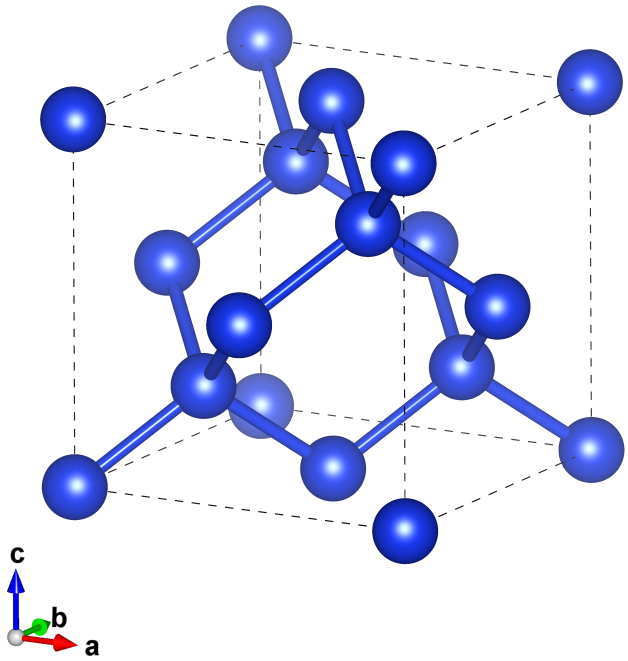

Figure 2.1: At ambient pressure, silicon & germanium crystallize in the diamond cubic crystal structure, which is two interpenetrating face-centered cubic sublattices.[46]

2.4 Basic properties of $Si_{1-x}Ge_x$

2.4.1 Thermal conductivity

The crystal structure of silicon (see Figure 2.1) is a strong covalent network, with a high thermal diffusivity, sound velocity, and lattice thermal conductivity. Figure 2.3 depicts the temperature dependent lattice constant, heat capacity, thermal diffusivity, and thermal conductivity for undoped, crystalline silicon that have been reported.[48–51] Thermal diffusivity decreases with increasing temperature due to increased phonon–phonon scattering.

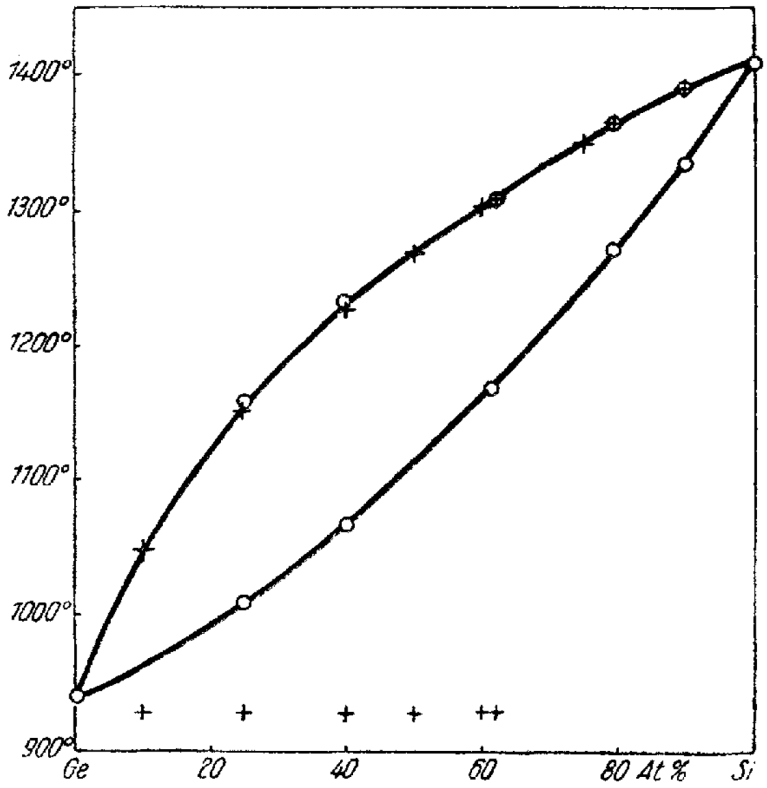

Figure 2.2: The silicon-germanium phase diagram. (Reprinted with permission from Stöhr and Klemm [47]. Copyright 2004 John Wiley and Sons. doi:10.1002/zaac.19392410401)

The density of a bulk thermoelectric (e.g. a pellet) of convenient shape may be measured by its weight and geometric volume. The density of an arbitrarily shaped bulk thermoelectric may be measured by the Archimedean method. The specific heat capacity may be measured by differential scanning calorimetry or estimated by the Law of Dulong-Petit (i.e. $C_p \approx 3R/M$, where R is the gas constant and M is the molar mass). The thermal diffusivity of a bulk thermoelectric may be measured by the laser flash method, where a laser is flashed at one side of the

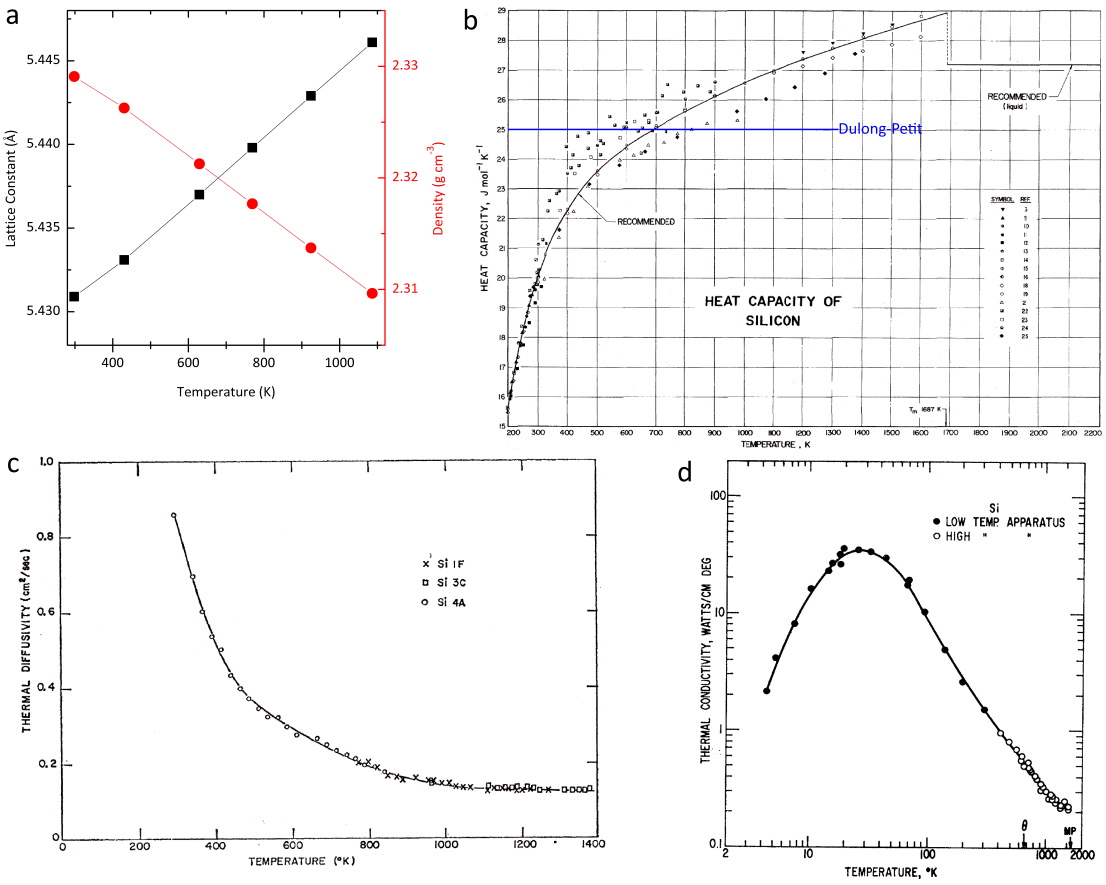

Figure 2.3: Temperature dependence of pure, crystalline silicon's (a) lattice constant (as reported by Yim and Paff [48]) & density, (b) heat capacity [Reprinted with permission from Desai [52]. Copyright 1986, AIP Publishing LLC.], (c) thermal diffusivity [Reprinted figure with permission from Shanks et al. [50], *Physical Review*, vol. 130, 1743, 1963, doi:10.1103/PhysRev.130.1743. Copyright 1963 by the American Physical Society.], and (d) thermal conductivity [Reprinted figure with permission from Glassbrenner and Slack [51], *Physical Review*, vol. 134, A1058–A1069, 1964, doi:10.1103/PhysRev.134.A1058. Copyright 1964 by the American Physical Society.]

pellet and the temporal response of the temperature profile on the other side of the pellet is measured.

Point defect scattering for reduced lattice thermal conductivity in $Si_{1-x}Ge_x$

The lattice thermal conductivity may be significantly reduced with the incorporation of germanium, as shown in Figure 2.4.[53–57] The thermal conductivity reduction is a manifestiation of increased phonon scattering at point defects.

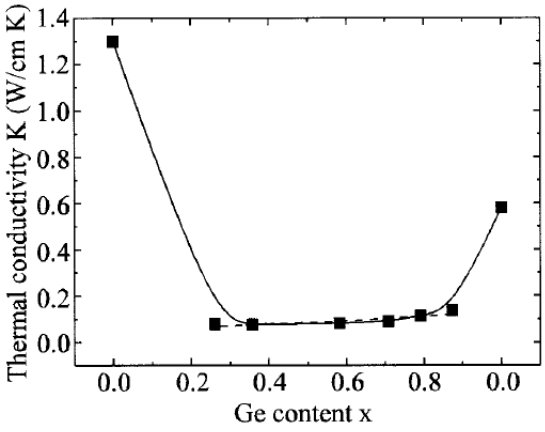

Figure 2.4: Effect of germanium content on lattice thermal conductivity of $Si_{1-x}Ge_x$.[53] (Reprinted with permission from Levinshtein et al. [54]. Copyright 2001, John Wiley and Sons.)

2.4.2 Carrier mobility

Intrinsic germanium (i-Ge) has a higher hole and electron mobility than i-Si. i-$Si_{1-x}Ge_x$ has a lower carrier mobility due to charge–point defect scattering. In all of the doped thermoelectric samples discussed in this thesis, the carrier mobility is limited by ionized impurity scattering.

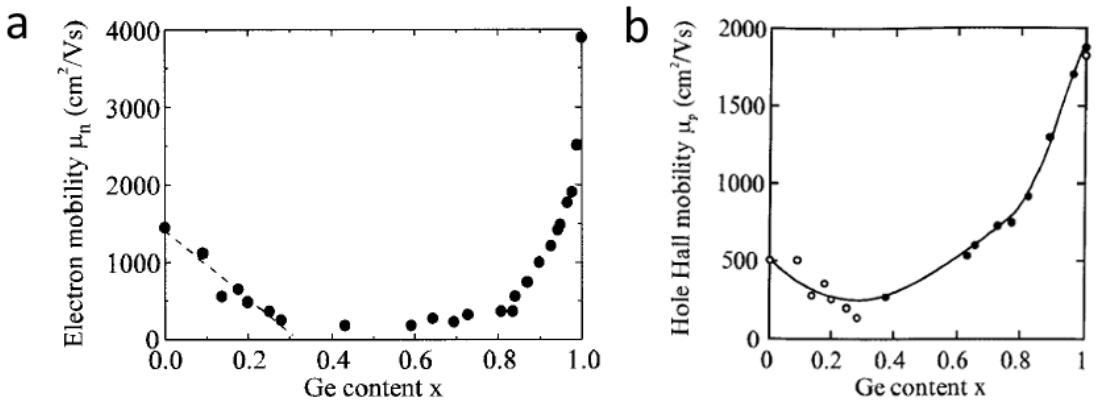

Figure 2.5: Hall mobilities in intrinsic $Si_{1-x}Ge_x$. (Reprinted with permission from Levinshtein et al. [54]. Copyright 2001, John Wiley and Sons.)

2.4.3 Extrinsic doping of $Si_{1-x}Ge_x$

Boron and phosphorus are substitutional dopants in $Si_{1-x}Ge_x$. The ionization energies of some common impurities in monocrystalline silicon are shown in Figure 2.6. Boron introduces shallow acceptor levels and phosphorus introduces shallow donor levels, which are essentially all ionized at room temperature to yield holes or electrons, respectively. The addition of boron or phosphorus into the $Si_{1-x}Ge_x$ lattice allows the carrier density to be tuned to the extent allowed by the solubility of the dopant. The dopant solubility is temperature dependent and preparation dependent; however, a high temperature solubility may be stable for some time at lower temperatures. The solubility of boron and phosphorus in c-Si are $\sim 2 \times 10^{20}$ cm^{-3} and $\sim 3 \times 10^{20}$ cm^{-3} at 900 °C, respectively.[58–60]

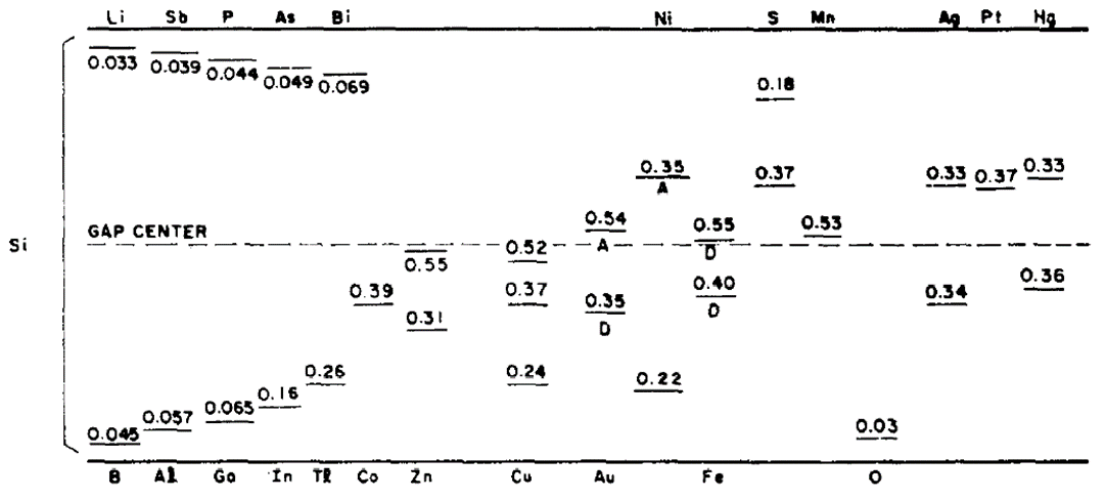

Figure 2.6: Ionization energies of some impurities in monocrystalline silicon. (Reprinted from *Solid-State Electronics*, Vol. 11 Issue 6, Sze and Irvin, "Resistivity, mobility and impurity levels in GaAs, Ge, and Si at 300K" [61], pages 599–602, Copyright 1968, with permission from Elsevier. doi:10.1016/0038-1101(68)90012-9)

The van der Pauw method to measure electrical resistivity

The electrical resistivity of a bar as shown in Fig. 2.7a may be determined according to equation 1.18 or by the van der Pauw method drawn in Fig. 2.7b. A current I_{21} is applied from contact 2 to contact 1 and the potential difference between contact 4 and 3 (V_{43}) are measured to give the resistance $R_{21,43}$. The resistance $R_{31,42}$ is measured similarly. The sheet resistance (R_s) that appears in the van der Pauw equation may be solved numerically, according to van der Pauw's procedure.[62]

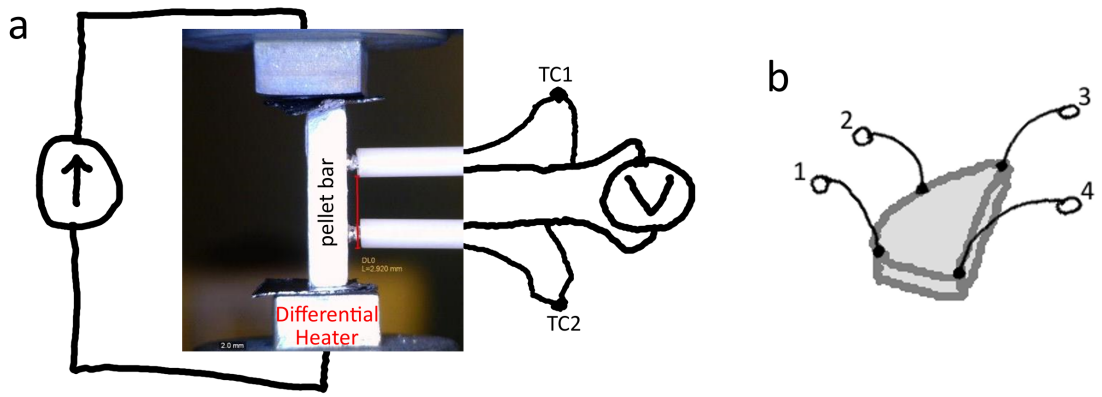

Figure 2.7: Schematics of how electrical conductivity is measured on the (a) ULVAC ZEM-3 and in the (b) van der Pauw configuration.[62]

The Hall effect

A magnetic field ($\|\mathbf{B}\|$) orthogonal to a conducting plane exerts a Lorentz force on charge carriers, giving rise to the Hall voltage that may be measured according to Figure 2.8. The Hall voltage is related to the carrier density by equation 2.5:

$$V_{Hall} = -\frac{I \, \|\mathbf{B}\|}{n \, t \, e} \quad , \tag{2.5}$$

where, for an n-type semiconductor, the n carriers (per volume) are all electrons, I is the excitation current, $\|\mathbf{B}\|$ is the magnetic field orthogonal to the conducting sheet, e is the elementary charge, and t is the thickness. When all of this information is known and an electrical conductivity has been determined, then the Hall mobility (μ_{Hall}) may be determined according to $\sigma = n_{Hall} \, e \, \mu_{Hall}$. Note that this is a simple use of the Hall results that won't take into account the Hall

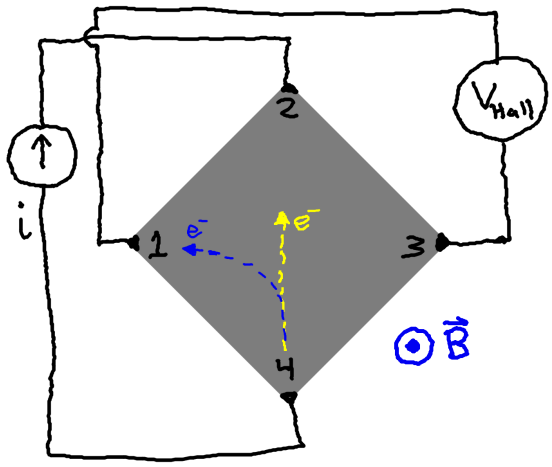

Figure 2.8: Schematic of how the Hall effect measurement is performed in the van der Pauw configuration.

scattering factor (r_{Hall}), which is important when interpreting Hall results for an inhomogeneous semiconductor, which will be discussed in Chapter 8.

Chapter 3

Porous silicon from electrochemically etched single crystal silicon

3.1 Porous silicon (PSi) films

Our first strategy to demonstrate the model heterostructure shown in 1.12 so that we could test the theoretical calculations of Lee et al. [28] and Lee and Grossman [29] for porous silicon (PSi) and germanium, was to electrochemically etch single crystal silicon. Uhlir was the first to report the electrochemical etching of silicon and germanium [63] and his work was forgotten until Canham demonstrated light emission from the electrochemically etched PSi.[64]

3.1.1 Previous studies on thermoelectric properties of PSi

The temperature-dependent thermal conductivity of porous silicon films was investigated by Gesele et al., who found that the porous silicon films had thermal conductivities that "were three to five orders of magnitude smaller than the values for bulk silicon."[65]

The electrical conductivity of porous silicon films are known to be degraded due to a high density of surface traps that compensate the dopants and/or the fluctuation in the band edges due to the inhomogeneous distribution of crystallites.[66] We will attempt to characterize the electrical conductivity of PSi prepared from highly boron-doped, p^{++} silicon wafer and aim to backfill the pores to yield a heterostructure with enhanced power factor, as shown in Figure 3.1c.

3.2 Synthesis of PSi

Highly boron-doped Si wafers were obtained from Siltronix. The setup shown in Figure 3.1a was used to perform the chemistry shown in Figure 3.1b. A current density J_1 was applied for some amount of time to generate the porous film and to obtain a freestanding film, we could use a different hydrofluoric acid concentration and current density.

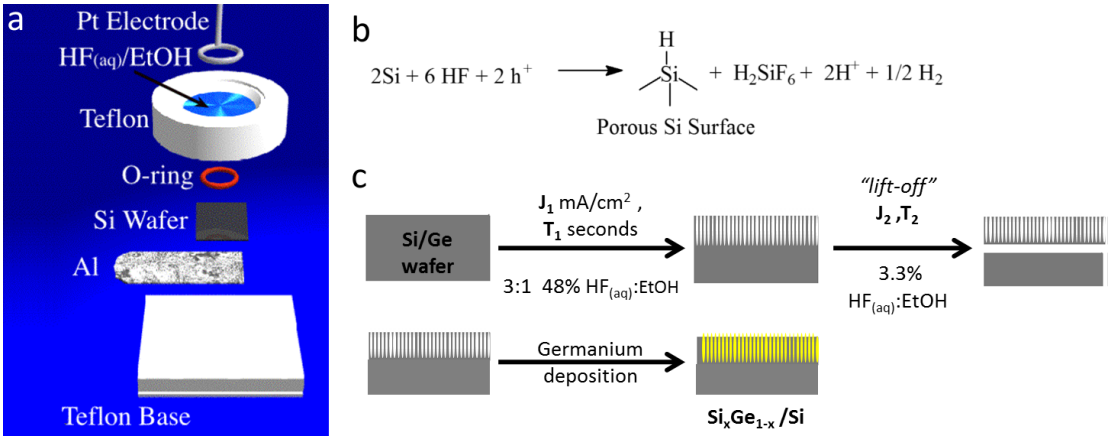

Figure 3.1: Scheme for the electrochemical synthesis of porous silicon. (a) electrochemical etching cell used to prepare porous Si from single crystal Si wafers (image credit: Sailor [67], used by permission), (b) the electrochemistry that takes place to etch the silicon wafer, and (c) the scheme to prepare freestanding porous silicon films or to backfill and prepare a silicon-germanium nanocomposite.

3.3 Electrical properties of the PSi films

We first characterized the resistance of the porous films on silicon in the sandwich configuration shown in Figure 3.2a. The current-voltage characteristic for a PSi film on Si is shown in Figure 3.2b. The slope of the trace is the reciprocal of the resistance, indicating that the PSi film has a higher electrical resistivity than the silicon wafer. We wanted to determine the electrical resistivity of the porous film, without the influence of the silicon substrate or the PSi/Si interface so we performed the electropolishing "lift-off" procedure.

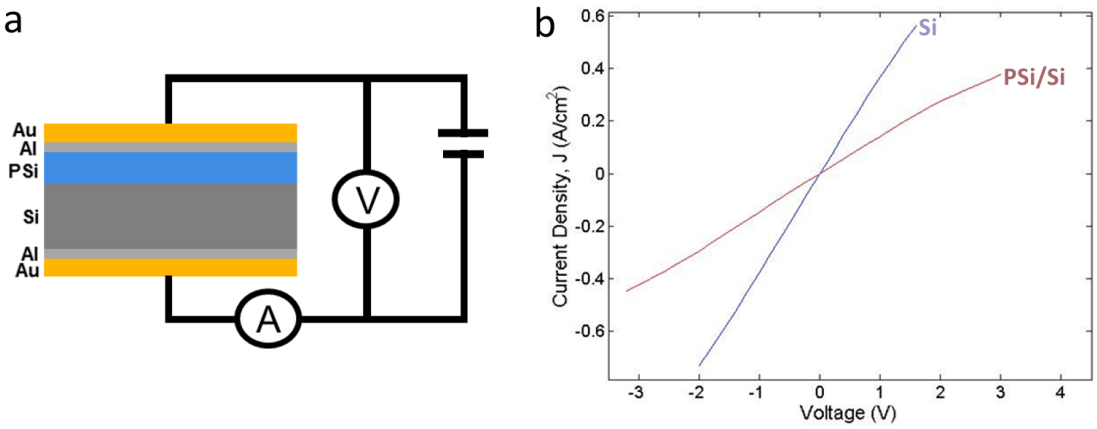

Figure 3.2: (a) Scheme for determining cross-sectional resistance of porous silicon film and (b) J-V curves of the starting silicon and the porous silicon film on silicon.

3.4 Free-standing porous silicon films

Upon drying, the PSi on Si films crack and the free-standing PSi films crack, as shown in Figure 3.3a & b. The cracking is a mechanism to relieve strain in the nanocrystalline film. It is concomitant with amorphousization of the structure, as shown in the Raman spectra of Figure 3.4, where the optical phonon of silicon at 520 cm^{-1} becomes asymmetric towards lower wavenumbers.[68]

CO_2 critical point drying was used to produce lifted-off PSi films with less cracks; however, the crack-free films would roll up, which made it difficult to probe their electrical resistivity. The thickness and porosity of the PSi films prepared under different conditions were determined by the gravimetric method discussed in *Properties of Porous Silicon*.[66] The properties of the PSi films that

we prepared are summarized in Table 3.1, which shows that PSi films on silicon had variable resistivities and once they were lifted-off of the silicon substrate they became insulators.

Etch Conditions	Layer Thickness (μm)	Porosity	PSi/Si Resistivity (Ω cm)	Freestanding PSi Resistivity (Ω cm)
0 mA cm^{-2}, 0 min.	0	0%	0.0008	N/A
10 mA cm^{-2}, 20 min.	~8	~61%	~1.6	~1×10^{6}
100 mA cm^{-2}, 20 min.	~50	~74%	~40,000	~1×10^{6}

Table 3.1: Properties of porous silicon films discussed in this chapter.

The poor electrical conductivity of PSi films is attributed to compensation due to trap states & undulating bands & extensive crack defects, as discussed in *Properties of Porous Silicon*– "the evaluated trap density is ~10^{19} cm^{-3}, the same order of magnitude as the dopant density."[66] PSi has not been successfully applied as an electronic material but it has been successfully applied as an optical material for biosensors, drug delivery, and gas sensors.[69–73]

We quickly abandoned this top-down approach to silicon thermoelectrics, in favor of a bottom-up process that would yield material with better electronic properties.

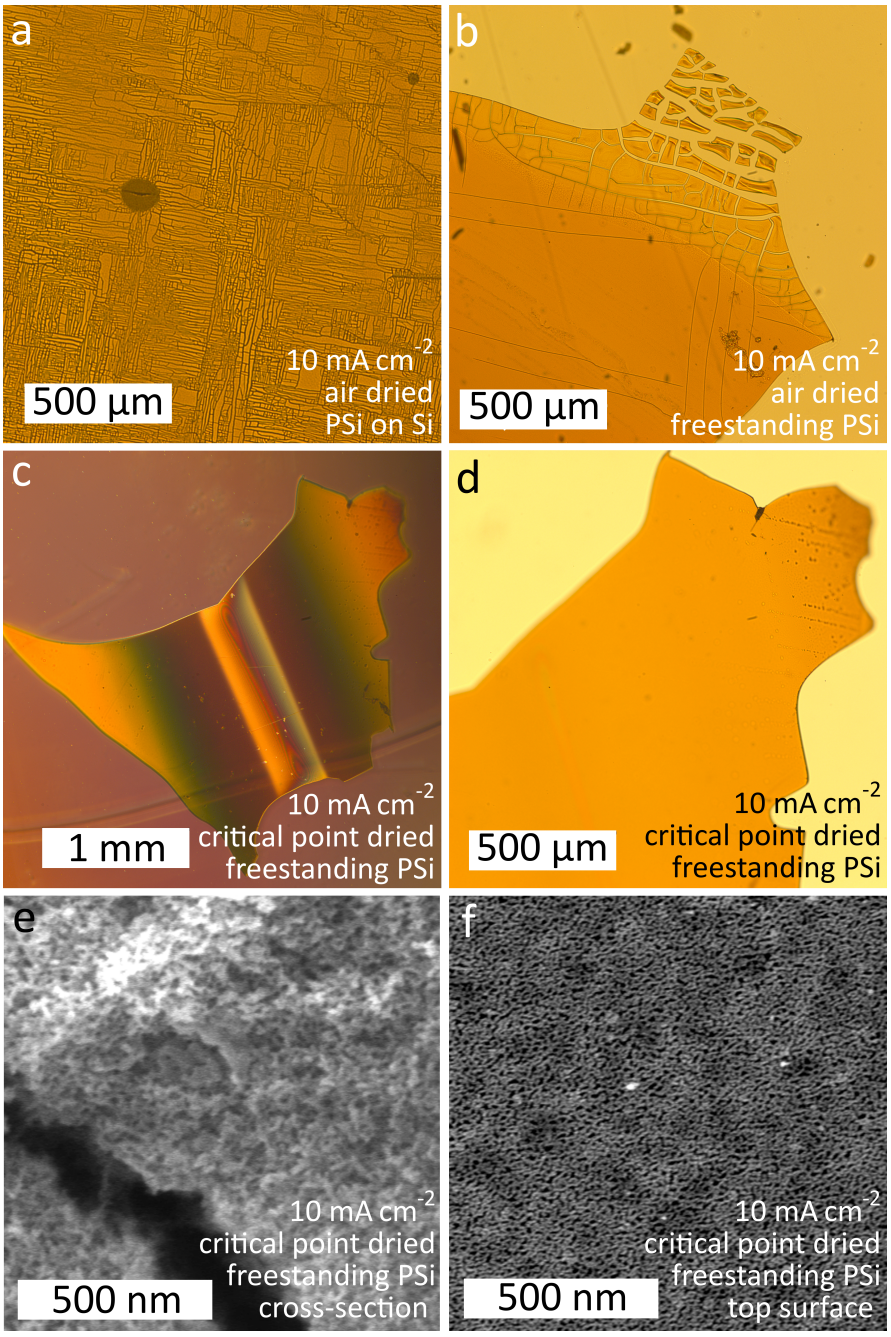

Figure 3.3: Micrographs of (a) air dried PSi on Si & (b) air dried freestanding PSi show widespread cracking, whereas (c–f) critically point dried freestanding PSi exhibit less cracking– instead they roll up.

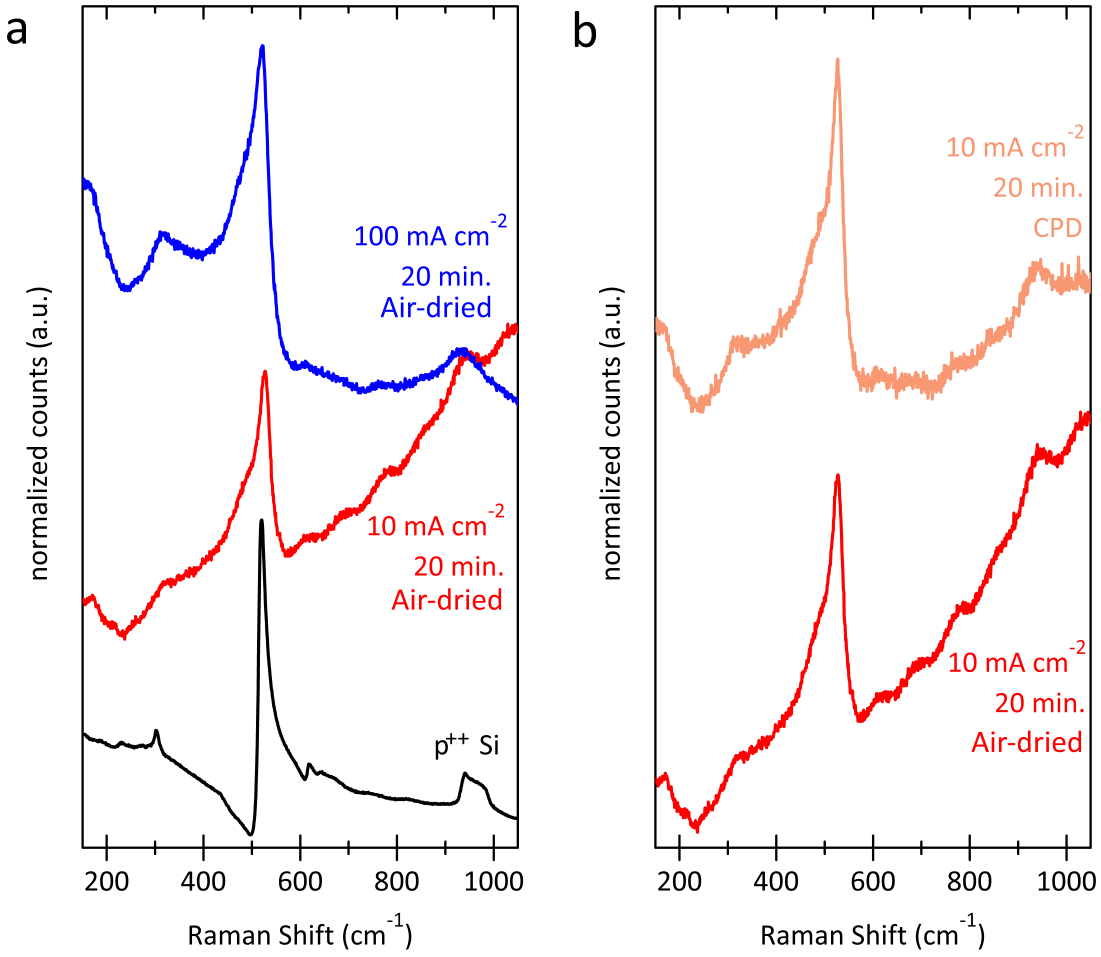

Figure 3.4: Raman spectra of the (a) starting p^{++} Si wafer and after electrochemical etching at two different current densities and (b) PSi that is dried in air compared to a critically point-dried PSi film.

Chapter 4

Magnesiothermic reduction of doped silica-germania nanocomposites

4.1 The carbothermal reduction of silicon dioxide

The highest thermoelectric performance reported for $Si_{1-x}Ge_x$ is for ball milled nanocomposites that were prepared from relatively costly metallurgical-grade silicon and germanium made through high temperature (~2000 °C) carbothermal reduction of high purity silica and a similar reduction process for germania. Therefore, an alternative strategy to obtain nanostructured SiGe particles directly from nanostructured oxides at low temperature is highly desirable.

Motivated by this goal, several attempts to synthesize hierarchically structured Si and SiC materials from silica at low temperature have been reported.[74, 75] Bao *et al.* first reported a successful magnesiothermic reduction of silica to silicon

at 650 °C that maintains the microstructure of the precursor oxide (in their case, a diatom frustule as shown in Figure 4.1).[76]

4.2 Maintaining microstructures with the magnesiothermic reduction of silicon dioxide

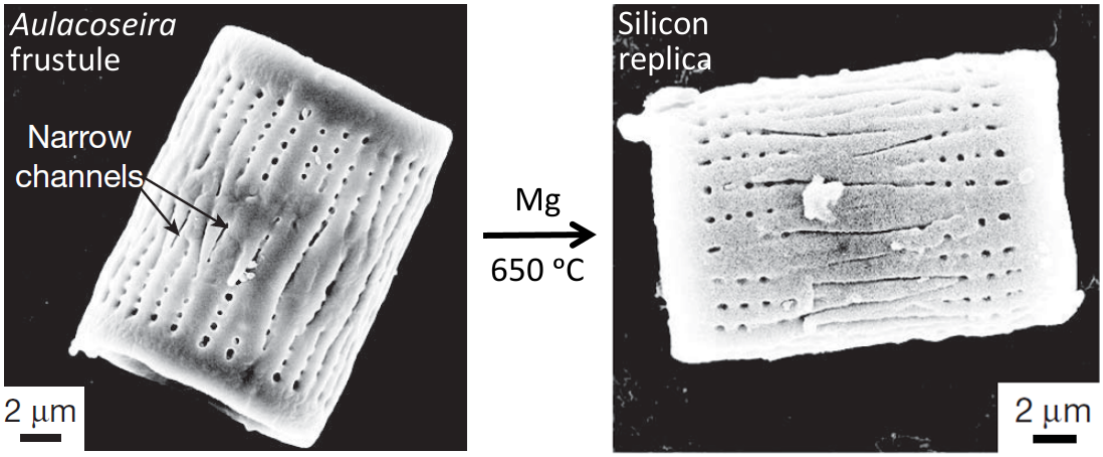

Figure 4.1: The magnesiothermic reduction of a diatom frustule maintains the microstructure of the frustule. (Adapted by permission from Macmillan Publishers Ltd: *Nature*, Ref. [76], Copyright 2007. doi:10.1038/nature05570)

The reduction chemistry and etch chemistries

The Bao et al. result was achieved by vapor transport of magnesium to the oxide. The reduction chemistry that occurs in the magnesiothermic reduction is

shown in equation 4.1 and overreduction leads to the silicide-germanides shown in 4.2. Szczech and Jin showed that the diatom frustule may be overreduced to the silicide and the diatom's structure is maintained.[77]

$$(SiO_2)_{1-x}(GeO_2)_x\ (s) + 2\ Mg\ (g) \xrightarrow{650\ ^\circ C} Si_{1-x}Ge_x\ (s) + 2\ MgO\ (s) \quad (4.1)$$

$$2\ Mg\ (g) + Si_{1-x}Ge_x\ (s) \longrightarrow Mg_2Si_{1-x}Ge_x\ (s) \quad (4.2)$$

The product of the magnesiothermic reduction contains impurity phases, which may be selectively etched according to equations 4.3–4.5.

$$MgO\ (s) + 2\ HCl\ (aq) \longrightarrow MgCl_2\ (aq) + H_2O\ (l) \quad (4.3)$$

$$Mg_2Si\ (s) + 4\ HCl\ (aq) \longrightarrow 2\ MgCl_2\ (aq) + SiH_4\ (g) \quad (4.4)$$

$$SiO_2\ (s) + 6\ HF\ (aq) \longrightarrow H_2SiF_6\ (aq) + 2\ H_2O\ (l) \quad (4.5)$$

Sustainability

The magnesiothermic reduction of silica obtained from rice husks and sand and application of those materials for lithium ion batteries has been reported.[78–80] The benefit of those silica sources is that they are plentiful: (1) a huge fraction of the population consume rice and (2) sand constitutes a huge fraction of the Earth's crust.

Another silica source, as shown above, is diatomaceous earth. Diatoms naturally incorporate boron into their cell walls with many types having 10–1000

ppm boron.[81, 82]. There have been studies on the effect of germanium incorporation on diatom growth and structure, as well.[83–86] Perhaps diatoms may be bioengineered to have the germanium and dopant content that would make them sustainable feedstock for nano-$Si_{1-x}Ge_x$ applications.

Although this low temperature route can successfully maintain the microstructure of the precursor oxide since it occurs below silicon's melting point, we are not aware of any studies on the electronic properties of the silicon obtained by this route or application of the magnesiothermic reduction to prepare silicon-based thermoelectrics.

4.3 What I propose to do

Shi demonstrated that the vapor-transport magnesiothermic reduction of a mesoporous silica, yielded a micro/mesoporous silicon, as shown in Figure 4.2. We aim to develop a one-pot synthesis of a doped silica-germania and potentially backfilling of the pores to achieve the nanocomposite structures shown in Figure 4.3 that may allow us to access the perturbative effects that give rise to enhanced functionality.

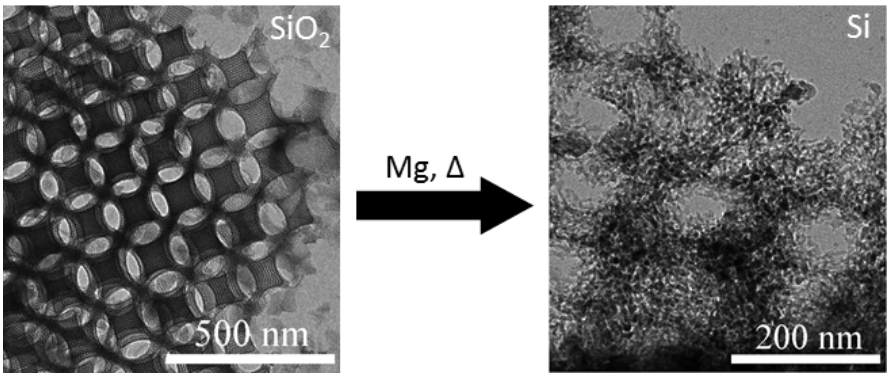

Figure 4.2: TEM images of a mesoporous silica and the micro/mesoporous silicon product obtained after vapor-transport magnesiothermic reduction (unpublished results by and with the permission of Shi [87]).

4.3.1 Free energies for reduction and importance for doping

The most important material property for tuning the thermoelectric efficiency is the carrier density, which is modulated by the dopant density; thus, we must develop a means to controllably dope the precursor oxide. The Ellingham diagram describes what species we may be able to reduce using magnesium.[88] Our doping strategy is to inject the desired amount of dopant into the solution during the sol-gel synthesis. The amount to inject is determined according to Figure 4.4. We use boron to yield p-type conductivity and phosphorus to yield n-type conductivity. The solubility of those dopants in the final $Si_{1-x}Ge_x$ are on the order of $\sim 2\times10^{20}$ cm^{-3} at 900 °C.[58–60]

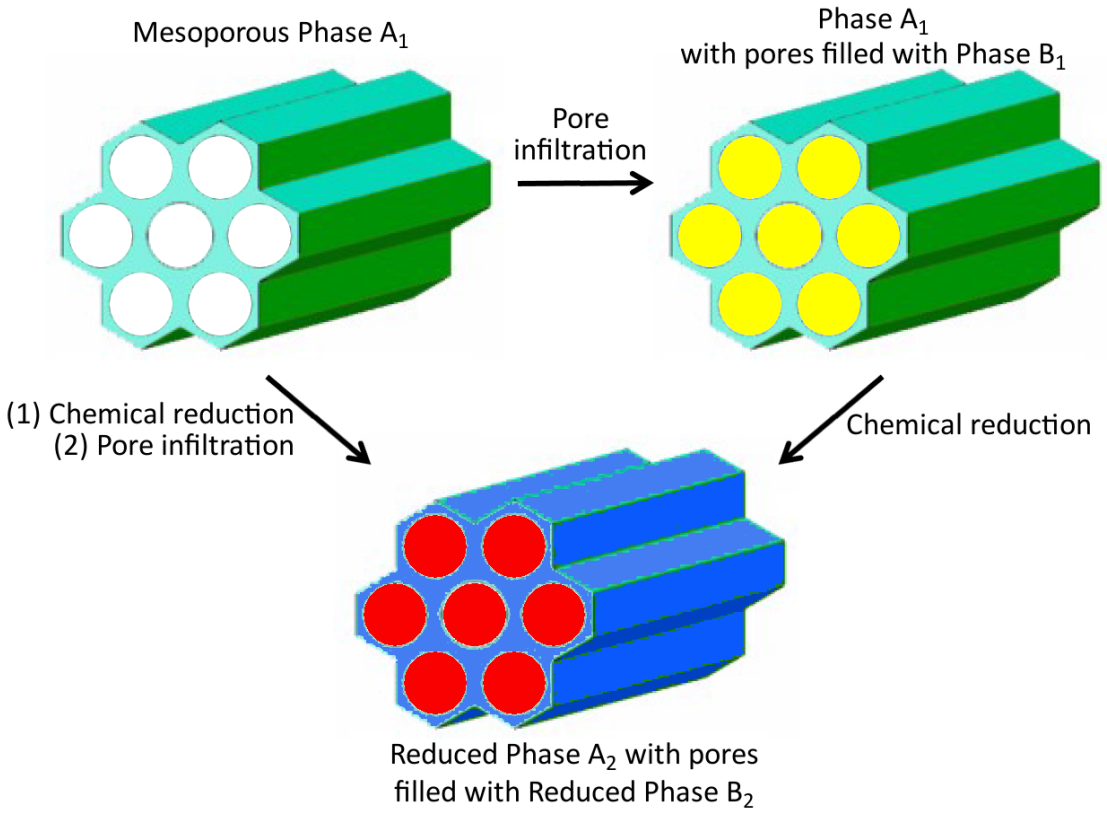

Figure 4.3: Scheme for the synthesis of ordered mesoporous material and pore-filled nanocomposites (Figure adapted, with permisson, from Zhang [45]).

4.4 "SBA-15" $(SiO_2)_{1-x}(GeO_2)_x$ nanocomposites

We chose Santa Barbara Amorphous type material, SBA-15 as a model nanocomposite to realize the structures shown in Figure 4.3.[89] There was a previous study on a SBA-15 borosilicate; however, the boron content in that study is greater than the amount of boron that we'll need to target in order get degenerately doped $Si_{1-x}Ge_x$.[90]

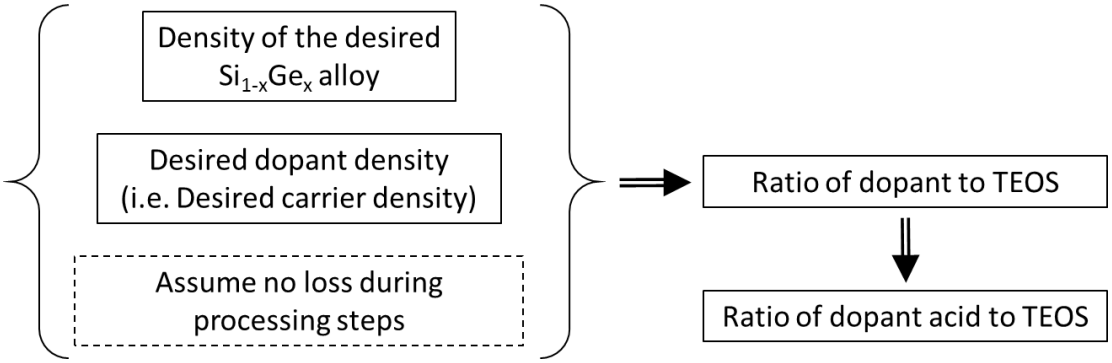

Figure 4.4: Method of determining how much dopant acid to use during the sol-gel synthesis to yield the desired dopant density.

4.4.1 Synthesis

SBA-15 was synthesized by the soft template, amphiphilic block copolymer Poly(ethylene glycol)-block-poly(propylene glycol)-block-poly(ethylene glycol) aka (PEG-PPG-PEG), commercially available as Pluronic-P123. 1 gram of P123, 30 mL of 2M HCl, and 7.5 mL of water were stirred at 38 °C until the solution was clear. Then 2.08 grams of tetraethylorthosilicate (TEOS) was injected and the solution was stirred for 24 hours. The viscosity increased in the first 15–25 minutes and then it decreased.

The sealed Nalgene bottle was placed in the oven at 100–130 °C for 24 hours. It was removed and the white powder was collected by vacuum filtration, dried at 25–60 °C over night, then the powder was calcined at 1.5 °C min^{-1} to 500 °C and soaked there for 5 hours.

The silica SBA-15 obtained by this synthesis is shown in the brightfield transmission electron micrographs shown in Figure 4.5.

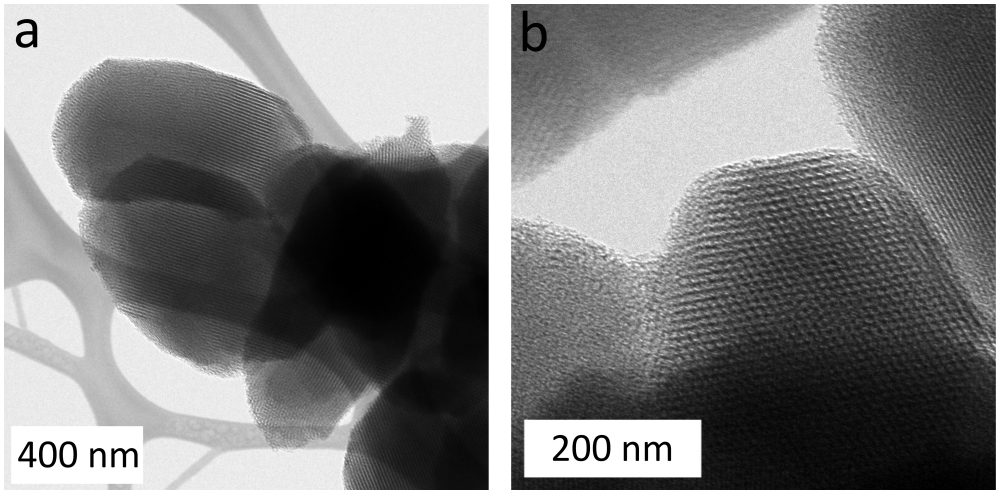

Figure 4.5: Brightfield TEM image of a SiO_2 SBA-15 after calcination.

The effect of the germanium dioxide precursor

The SiO_2–GeO_2 system has been studied extensively for fiber optic cables due to the tunability of the index of refraction by incorporation of germania.[91–94] Processing at high temperature appears to yield homogeneous silica germania.[95] It is known that TEOG and chlorogermanes have larger hydrolysis and condensation rates than their silicon analogs; however, there are reports of homogeneous, self-assembled mesoporous silica-germania films.[96] To the best of my knowledge the nanoscale heterogeneity of sol-gel synthesized silica-germania prepared from the alkoxides has not been definitively shown but the heterogeneity has been dis-

cussed for SiO_2-GeO_2 glass preforms and fibers prepared by vapor phase axial deposition method,[97] and proton implantation into GeO_2-SiO_2 was shown to yield embedded germanium nanocrystals[98] and hydrogen reduction of the GeO_2-SiO_2 was shown to yield embedded germanium nanocrystals.[99]

The phase diagram of the SiO_2–GeO_2 system shown in Figure 4.6 indicates that a solid solution will form at high temperature but at lower temperatures, equilibrium favors the precipitation of crystalline germania. I was never able to determine the type crystallinity of the germania obtained in this thesis work. There are different structures of germania that have appreciable solubility in water and so aqueous processing should be avoided for nanostructured germania.[100]

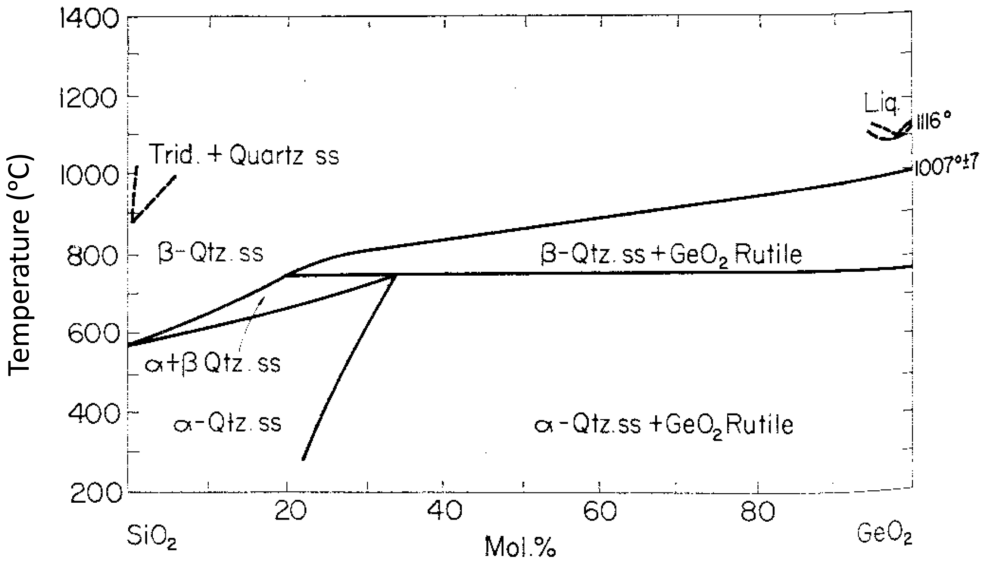

Figure 4.6: Equilibrium phase diagram for the SiO_2–GeO_2 system, as reported by Shafer and Roy [101] and Levin et al. [102]. (Reprinted with the permission of The American Ceramic Society, `www.ceramics.org`.)

"SBA-15" $(SiO_2)_{95}(GeO_2)_5$ was synthesized by the appropriate molar substitution of germanium (IV) ethoxide (TEOG) for the TEOS. Condensation was rapid and visible within 30 seconds. A white film was observed on the pipet used to inject the TEOG.

4.4.2 Microstructure

Scanning electron microscopy was used to show that the germania precursor affects the "SBA-15" particle morphology as shown in Figure 4.7. The Si:Ge=95:5 (nominal composition) "SBA-15" has a rod-like structure that is more tortuous and there are tiny, brighter particles on the surface, and the particle diameter is reduced.

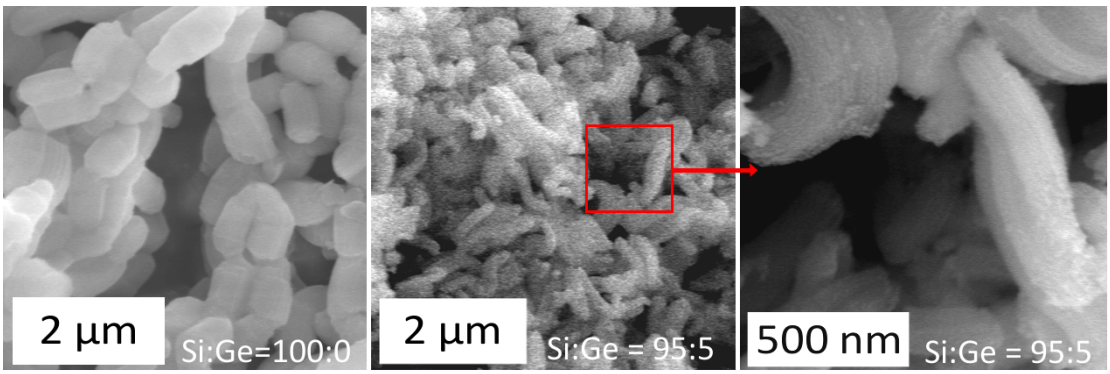

Figure 4.7: SEM images of the calcined SBA-15's show the germania precursor causes morphological changes and the $(SiO_2)_{95}(GeO_2)_5$ "SBA-15" has small dots decorating the surface of the rods.

4.4.3 Porosity

Nitrogen adsorption/desorption was performed to determine the Brunauer-Emmett-Teller (BET) surface area of the "SBA-15s" (see Fig. 4.8a) and the Barrett-Joyner-Halenda (BJH) pore size distribution is shown in Figure 4.8b. The germania precursor does not significantly affect the specific surface area or the average pore size.

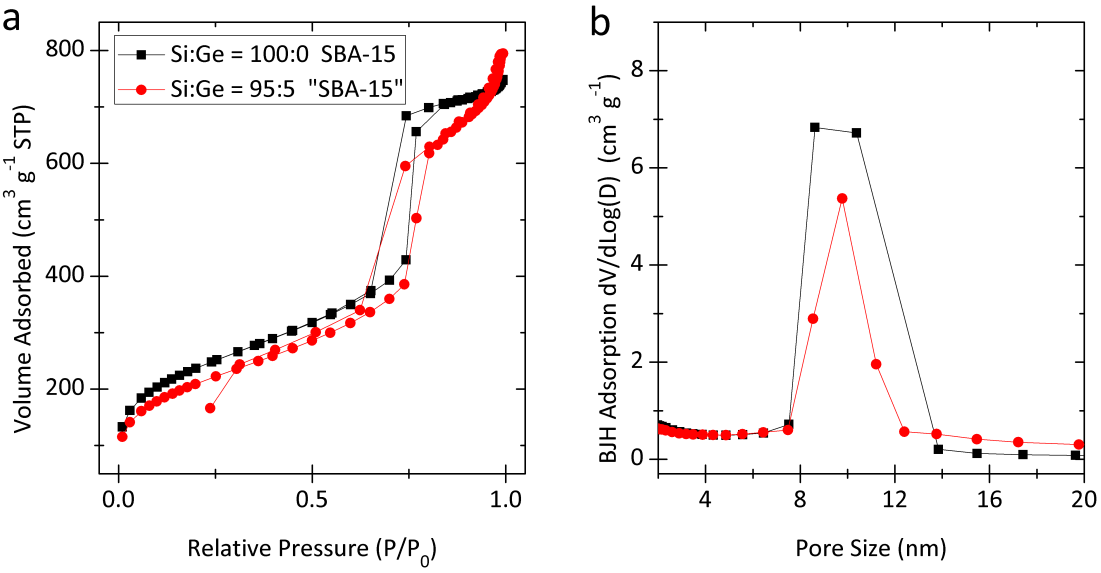

Figure 4.8: Porosimetry of the SiO_2 SBA-15 and $(SiO_2)_{95}(GeO_2)_5$ "SBA-15"after calcination: (a) N_2 adsorption/desorption isotherms and (b) pore size distribution.

Small-angle XRD indicates that the germania precursor does not signficantly affect the d_{100} spacing or pore ordering as shown in Figure 4.9.

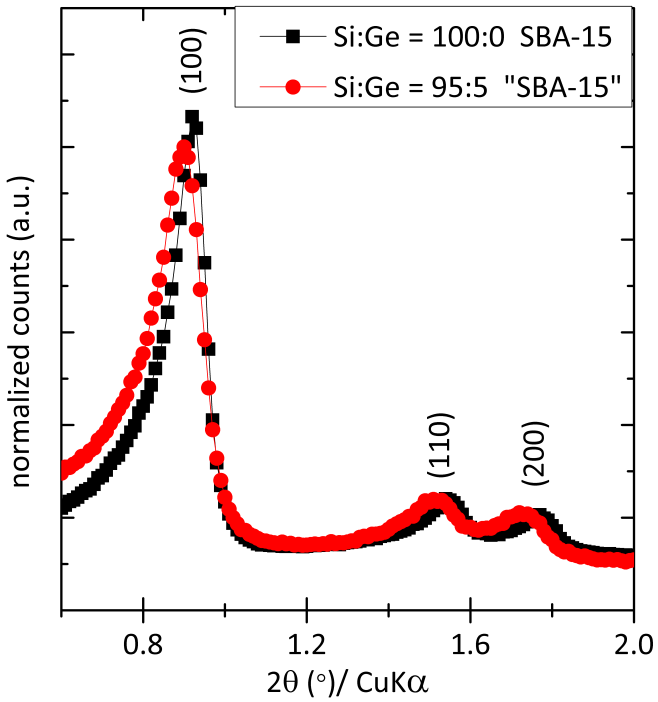

Figure 4.9: Small-angle XRD patterns of the SiO_2 SBA-15 and $(SiO_2)_{95}(GeO_2)_5$ "SBA-15" after calcination indicate that addition of germania precursor at 5 mol% doesn't appear to affect the d_{100} spacing of the pore structure.

Compilation of the structural properties of the "SBA-15s" is shown in Table 4.1. The germania precursor seems to only affect the particle diameter which may be due to the rapid formation of GeO_2 particles that disrupt the soft template.

SBA-15	BET Area (m^2 g^{-1})	Pore Size (nm)	d_{100} (nm)	Wall Thickness (nm)	Particle length (nm)	Particle Diameter (nm)
Si:Ge = 100:0	840	9.5	9.4	1.4	900	510
Si:Ge = 95:5	745	9.8	9.6	1.3	860	210

Table 4.1: Summary of the structural properties of the calcined "SBA-15" nanocomposites.

Silica and germania nanocomposites for battery applications

There have been recent studies on silica and germania for anode materials that exhibit high and stable capacities.[103–106] The phase segregation in our "SBA-15" $(SiO_2)_{1-x}(GeO_2)_x$ may exhibit enhanced battery properties. We have attempted to prepare battery cells with our oxide nanocomposite; however, the films we apply to the electrode peel off. This work is ongoing with Dr. Young-Si Jun & Dayton Horvath.

4.4.4 Retention of phase segregation after magnesiothermic reduction of $(SiO_2)_{95}(GeO_2)_5$ "SBA-15"

The $(SiO_2)_{95}(GeO_2)_5$ "SBA-15" was reduced with 2 mol. equivalent of magnesium powder that were gently mixed and placed in a steal tube in an argon glovebox and then sealed. The tube was placed in a box furnace and heated to 650 °C. The obtained brown & purple-ish powder were cleaned with hydrochloric acid and then hydrofluoric acid. The Raman spectrum of the $(Si)_{95}(Ge)_5$ "SBA-15" is shown in Figure 4.10 and compared to a $Si_{95}Ge_5$ alloy prepared by ball milling (BM) and hot pressing (HP) silicon and germanium powders. The absence of a Raman band at ~400 cm^{-1} indicates that the $(Si)_{95}(Ge)_5$ "SBA-15" has no Si–Ge alloying.

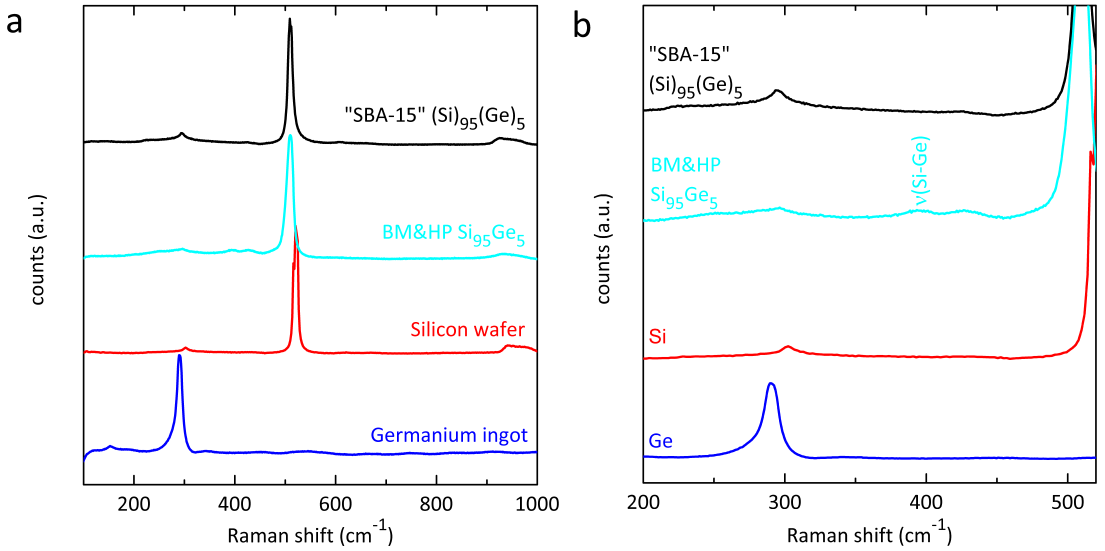

Figure 4.10: (a) Raman spectra of phase-segregated $(Si)_{95}(Ge)_5$ "SBA-15" compared to an alloyed $Si_{95}Ge_5$, Si, and Ge indicates that there is no significant alloying between Si & Ge in the $(Si)_{95}(Ge)_5$ "SBA-15". (b) The same Raman spectra but zoomed in to show the absence of Si–Ge vibrations in the $(Si)_{95}(Ge)_5$ "SBA-15".

Raman spectroscopy is a useful tool for studying the diamond cubic crystal system. The Raman shifts and relative intensities for characteristic phonon bands in crystalline $Si_{1-x}Ge_x$ are shown in 4.11 and in 4.2. If the $Si_{1-x}Ge_x$ is nanos-

Band	**Raman Shift** (cm^{-1})
Si(2TA)	300
Ge($\|\mathbf{q}\| \approx 0$)	300
Si–Ge	400
Si($\|\mathbf{q}\| \approx 0$)	520
Si(2TO)	950

Table 4.2: Characteristic Raman bands in crystalline $Si_{1-x}Ge_x$.[107–109]

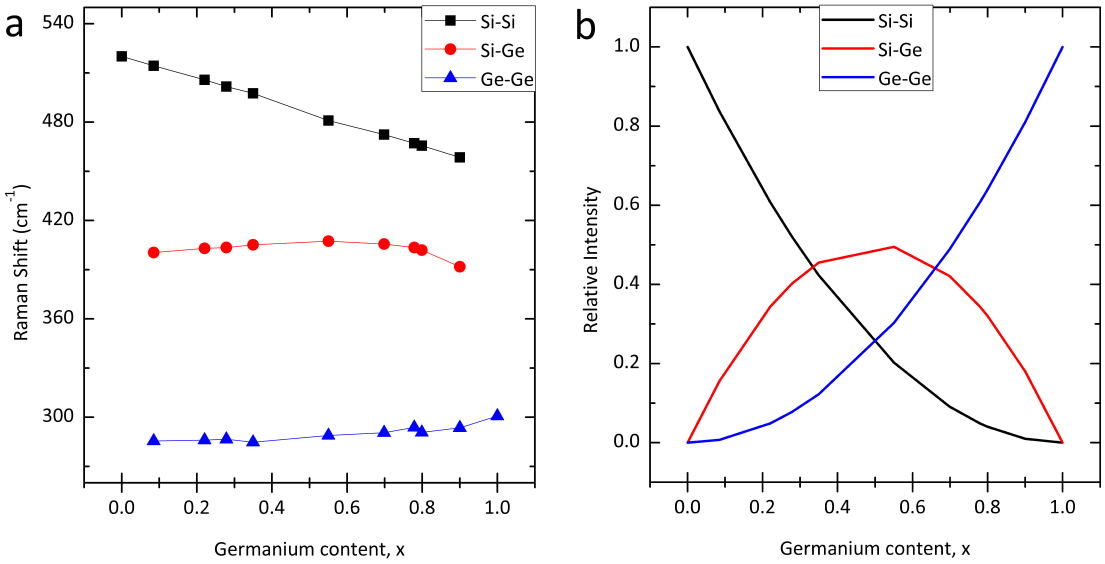

Figure 4.11: (a) Raman shifts, as reported by Alonso and Winer [107] and (b) relative intensities in the $Si_{1-x}Ge_x$ system. (Fig. 4.11a adapted with permission from Levinshtein et al. [54]. Copyright 2001, John Wiley and Sons.)

tructured, then the optical phonon shifts to lower wavenumber due to phonon confinement effect.[110] If the $Si_{1-x}Ge_x$ is doped, then it can produce an asymmetry in the phonon band due to Fano resonance. These spectral features are useful for characterizing $Si_{1-x}Ge_x$; however, the presence of multiple broadening or shifting phenomena makes analysis mostly qualitative.

Poor yields after reduction and etch chemistries

The aforementioned magnesiothermic reduction of $(SiO_2)_{95}(GeO_2)_5$ "SBA-15" produced a very low yield of product due to: (1) low density of the mesoporous

oxide and limited reactor volume and (2) high surface area and instability of the porous structure. We wanted to make a lot of material because that is what we will need to get a pellet for thermoelectric characterization and considered nanospheres as a better alternative since a ~30 nm silica sphere should have a specific surface area of ~40 m^2/g, which is much less than that of our SBA-15.

4.5 "Stöber" $(SiO_2)_{1-x}(GeO_2)_x$ nanocomposites

4.5.1 Synthesis of the $(SiO_2)_{1-x}(GeO_2)_x$

A silica germania nanocomposite was synthesized via an adaptation of the modified Stöber method used by Strandwitz *et al.*[111, 112] Silica-germania nanospheres were formed by the ammonia-catalyzed hydrolysis and condensation of a mixture of tetraethyl orthosilicate (TEOS) and germanium(IV) ethoxide (TEOG) dissolved in ethanol. The ratio of silicon to germanium was tuned by adjusting the molar ratio of the TEOS and TEOG precursors.

Tetraethyl orthosilicate (X grams TEOS, 99.999%, Alfa-Aesar) and germanium(IV) ethoxide (Y grams TEOG, 99.995%, Alfa Aesar) were added to a glass vial and bath sonicated for 10 seconds. This mixture was injected into ethanol (280 mL, 200 proof) that was stirred inside an Erlenmeyer flask by a magnetic stir bar. Aqueous ammonium hydroxide (8.4 mL, 30 wt.%, ACS grade, EMD) was

added drop wise over three minutes. Then ethanolic dopant acid (Z µL of 1 M solution was quickly injected, the flask was sealed with parafilm, and the mixture was stirred for 24 hours. The parafilm was removed and the flask was placed in an oven for 24 hours at 65 °C. The condensate was obtained by vacuum filtration, rinsed with deionized water and ethanol, redispersed in ethanol, and allowed to dry in a crystallization dish at room temperature over several days. The oxide powder was calcined at 500 °C for 6 hours. In order to obtain $(SiO_2)_{90}(GeO_2)_{10}$: X = 6.768 and Y = 0.9126. In order to obtain $(SiO_2)_{80}(GeO_2)_{20}$: X = 6.016 and Y = 1.826.

Boron-doped $(SiO_2)_{1-x}(GeO_2)_x$

Borosilicates have been studied thoroughly and are a great accomplishment of materials science. The weight ratio of boron to silicon in PYREX is ~10%.[113] The properties and structure of B_2O_3–GeO_2 glasses have been determined and there is no sign of phase separation or microclustering.[114]

Boron was incorporated into the oxide by injecting an aliquot of ethanolic boric acid into the precursor solution immediately after the ammonia was added. The volume of the boric acid aliquot was selected based on the boron content desired in the silicon germanium alloy (see Figure 4.4). Boron was chosen because 1) it is a common p-type dopant in silicon semiconductors,[61] 2) there has

been extensive research and development of borosilicates, including borosilicate nanoparticles,[115] and 3) the incorporation of boron into mesoporous silica SBA-15 has been demonstrated.[90] The added boric acid resulting in the desired boron doping concentrations did not affect the particle shape or size for our samples.

We used boric acid as our dopant acid to yield p-type materials. For the dopant series, $[B]_1$: Z = 0; $[B]_2$: Z = 71; $[B]_3$: Z = 710; and $[B]_4$: Z = 7100.

Borates may be incorporated in the silicate structure directly, or boric esters (see equation 4.6) may play some role in that incorporation, or residual boron species may form B_2O_3 upon calcination of the oxide (see equation 4.9) and that may be reduced to elemental boron during the magnesiothermic reduction.

$$B(OH)_3 + 3\ C_2H_5OH \longrightarrow B(OC_2H_5)_3 + 3\ H_2O \tag{4.6}$$

$$B(OH)_3 \xrightarrow{170\ ^\circ C} HBO_2 + H_2O \tag{4.7}$$

$$4\ HBO_2 \xrightarrow{300\ ^\circ C} H_2B_4O_7 + H_2O \tag{4.8}$$

$$H_2B_4O_7 \xrightarrow{\Delta} 2\ B_2O_3 + H_2O \tag{4.9}$$

Phosphorus-doped $(SiO_2)_{1-x}(GeO_2)_x$

Phosphosilicates have been prepared with phosphoric acid during the sol-gel synthesis. [116–119] The phosphosilicates have been used to improve thermal stability of cotton fabrics and for flame retardancy.[120–122] To the best of my

knowledge, all previous studies introduced a phosphorus content much greater than the work discussed in this thesis and desireable for n-type $Si_{1-x}Ge_x$.

Anastasescu et al. observed the loss of phosphorous in silica-phosphate sol-gel films.[123] Livage et al. observed that phosphoric acid reacts too fast during the polycondensation reaction leading to precipitation rather than gelation[124] and Fernandez-Lorenzo et al. noted that it is difficult to achieve homogeneity in the sol-gel synthesis of SiO_2-P_2O_5 glasses.[125] Szu et al. used MAS-NMR to show that phosphite and phosphate lead to different crystallization in the phosphosilicate gels.[126] Another NMR study considered a variety of phosphorus sources and that the amount of phosphorus lost during the processing depends on the precursor and the preparation method.[127]

We used phosphorous acid and phosphoric acid as our dopant acids to yield n-type materials. For the dopant series, $[P]_1$: Z = 0; $[P]_2$: Z = 71 H_3PO_4; $[P]_3$: Z = 71 H_3PO_3; and $[P]_4$: Z = 7100 H_3PO_3.

It is uncertain exactly how the phosphorus gets incorporated to eventually yield elemental phosphorus; however, phosphorous acid may deprotonate following equations 4.10–4.11 to leave phosphites in the silicate network or residual phosphorous acid may be left and then during the calcination, it would convert

to phosphoric acid as shown in equation 4.12.

$$HPO(OH)_2 + OH^- \longrightarrow HPO(OH)(O)^- + H_2O \quad (4.10)$$

$$HPO(OH)(O)^- + OH^- \longrightarrow HPO(O)_2^- + H_2O \quad (4.11)$$

$$4\ HPO(OH)_2 \xrightarrow{200\ ^\circ C} 3\ H_3PO_4 + PH_3 + ... \quad (4.12)$$

Addition of the phosphoric acid, likely forms phosphates that will form in phosphate-rich regions in the silicate network. Residual phosphoric acid may thermally decompose during the calcination of the oxide, yielding phosphorus suboxides that could be reduced to elemental phosphorus.

$$H_3PO_4 + 3\ OH^- \longrightarrow {PO_4}^{3-} + 3\ H_2O \quad (4.13)$$

$$H_3PO_4 \xrightarrow{\Delta} (PO_2OH)_n + H_2O \quad (4.14)$$

The effect of the germanium dioxide precursor

Due to the high hydrolysis and condensation rate of the TEOG precursor relative to that of TEOS, $(SiO_2)_{1-x}(GeO_2)_x$was also prepared with germanium (IV) isopropoxide and germanium (IV) n-butoxide as the precursors. The hydrolysis and condensation rates appeared to be the same as for TEOG based on visual observation.

4.5.2 Microstructure of the $(SiO_2)_{1-x}(GeO_2)_x$

Fusion of the oxide nanospheres was achieved through a mild thermal treatment of the oxide condensate and precursor solution before the oxide was isolated by vacuum filtration, rinsed with water and ethanol, redispersed in ethanol, and dried at room temperature. The oxide was then calcined. Figure 4.13a presents a scanning electron microscope (SEM) image of the calcined $(SiO_2)_{90}(GeO_2)_{10}$ nanocomposite that was obtained, which shows that the particles are monodisperse with an average diameter between ~16 and 30 nm. Imaging with a scanning transmission electron microscope (STEM) reveals a more complex nanostructure, with ~3 nm diameter germania clusters randomly dispersed throughout the oxide matrix (Figure 4.13b). The electron micrographs indicate that the particles had fused.

Calcination changes the morphology slightly

Figure 4.12 shows an SEM image of the $(SiO_2)_{90}(GeO_2)_{10}$ composite, indicating that the particles are ~30 nm spheres. A high-angle annular dark-field (HAADF) scanning transmission electron microscope (STEM) image of the $(SiO_2)_{90}(GeO_2)_{10}$ indicates a finer structure with ~3 nm diameter GeO_2 dots embedded in the silica, as inferred from the Z-contrast. Calcination has a slight effect on the particle size and morphology as shown in Figure 4.13. The particles

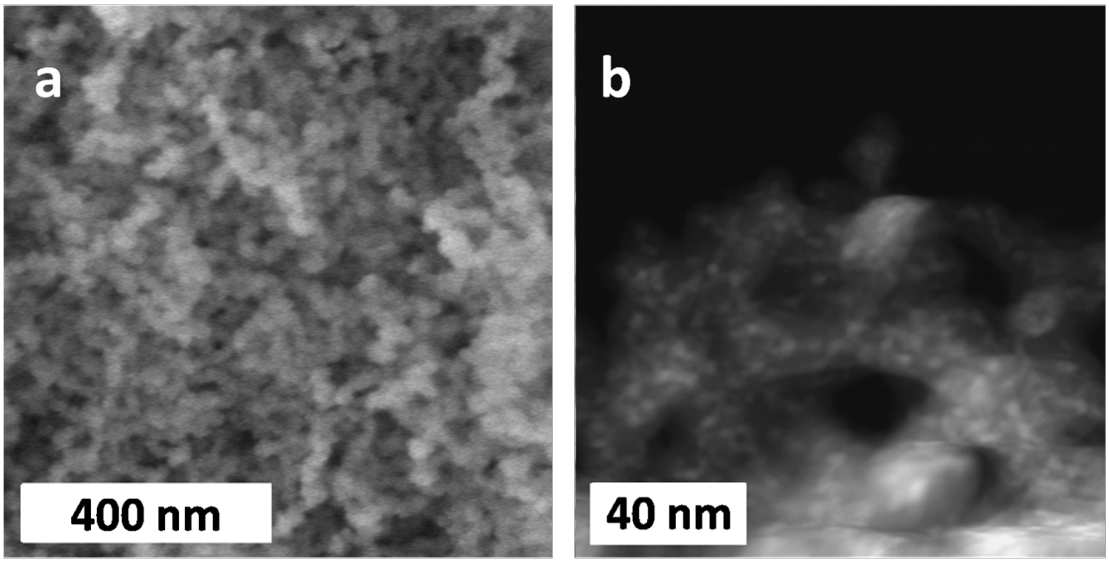

Figure 4.12: (a) SEM image and (b) HAADF–STEM image of the $(SiO_2)_{90}(GeO_2)_{10}$ composite before calcination, which indicates the presence of germania particles (~3 nm diameter) embedded in the silica nanoparticle matrix.

appear rougher, the particle diameter is ~16 nm and the embedded GeO_2 are ~3 nm in diameter.

The amount of germania precursor used doesn't appear to significantly affect the particle size or morphology from $(SiO_2)_{90}(GeO_2)_{10}$ to $(SiO_2)_{80}(GeO_2)_{20}$.

Brightfield TEM images of $(SiO_2)_{90}(GeO_2)_{10}$ (see Fig. 4.14) may be compared to $(SiO_2)_{80}(GeO_2)_{20}$ (see Fig. 4.15), indicating that more germania precursor

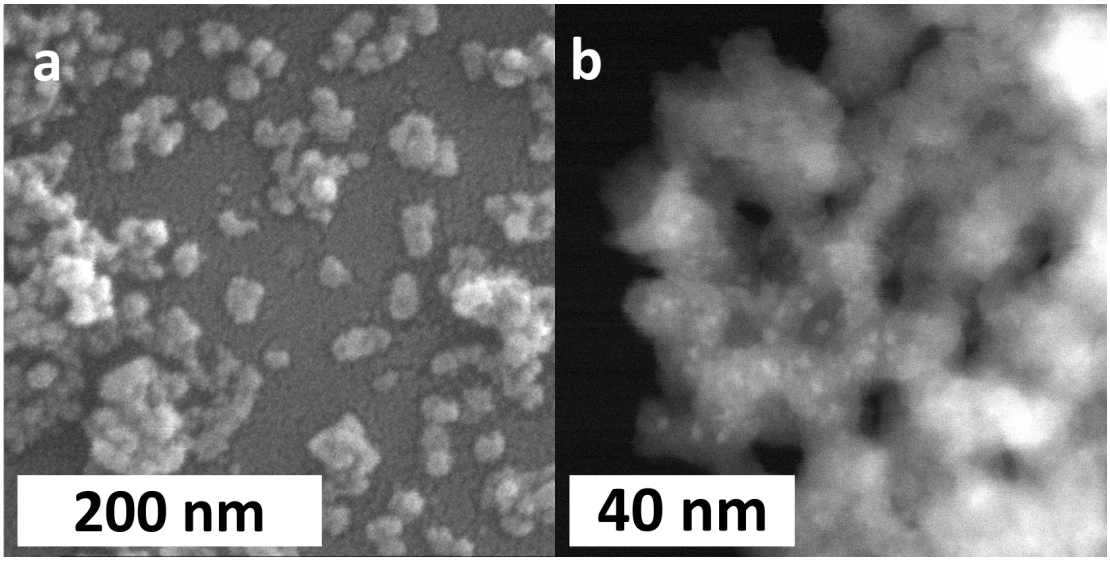

Figure 4.13: (a) SEM image and (b) HAADF–STEM image of the calcined $(SiO_2)_{90}(GeO_2)_{10}$ composite, which indicates the presence of germania particles (~3 nm diameter) embedded in the silica nanoparticle matrix. (Reprinted with permission from Snedaker et al. [128]. Copyright 2013 American Chemical Society.)

slightly decreases the diameter of the particles. Note that the embedded germania dots are not discernible in brightfield TEM mode.

Heterogeneity in the phosphorus-doped $(SiO_2)_{80}(GeO_2)_{20}$

The HAADF-STEM image of $(SiO_2)_{80}(GeO_2)_{20}$–$[P]_4$ and EDX linescan shown in 4.16 indicate the presence of a phosphorus rich region. Note that the image quality and EDX signal to noise ratio are poor. A better signal to noise ratio

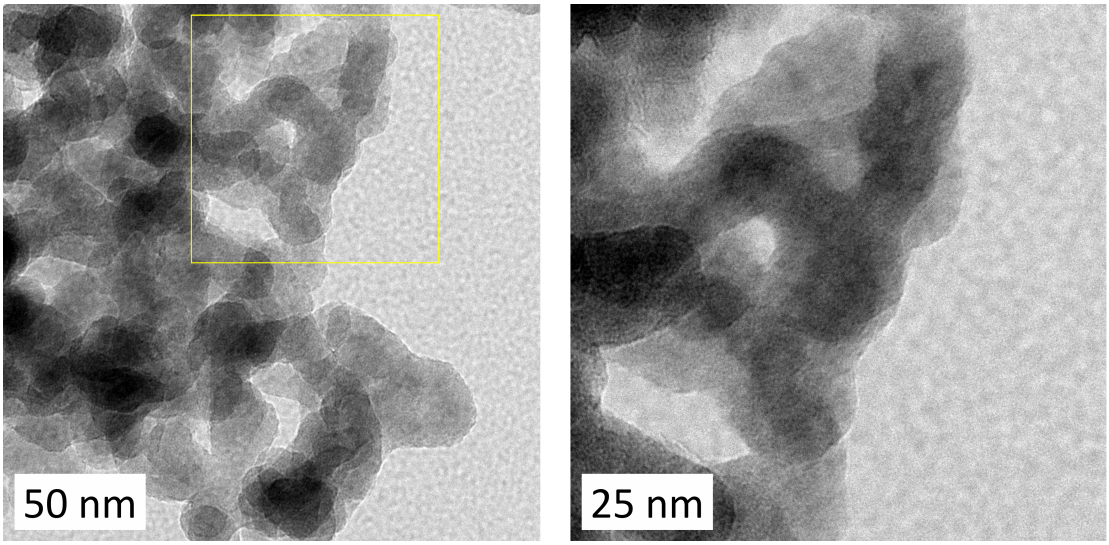

Figure 4.14: Brightfield TEM image of the boron-doped $(SiO_2)_{90}(GeO_2)_{10}$ after calcination. Note that there is no contrast that indicates embedded particles.

should be obtained using a lower spot number, higher beam current, and longer acquisition time.

Powder XRD of the calcined $(SiO_2)_{1-x}(GeO_2)_x$ nanocomposite did not detect the presence of crystalline GeO_2. Electron diffraction of the calcined $(SiO_2)_{1-x}(GeO_2)_x$ nanocomposite did not detect the presence of crystalline GeO_2.

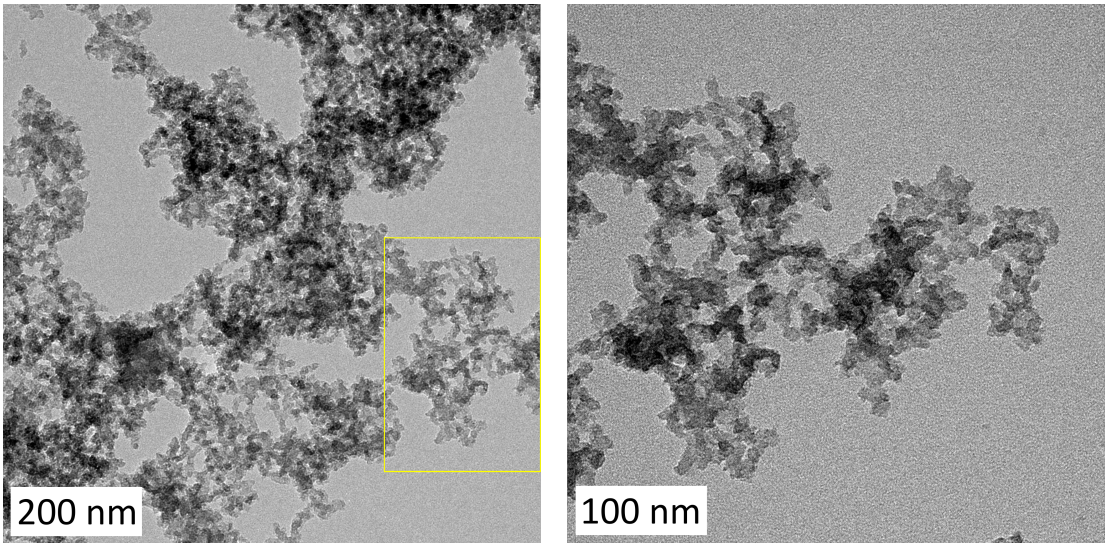

Figure 4.15: Brightfield TEM image of the phosphorus-doped $(SiO_2)_{80}(GeO_2)_{20}$ after calcination. Note that there is no contrast that indicates embedded particles.

4.5.3 Magnesiothermic reduction of the "Stöber" $(SiO_2)_{1-x}(GeO_2)_x$

A pellet of oxide powder and magnesium powder was prepared by grinding the oxide (0.6 grams) with magnesium (0.6 grams, -325 mesh powder, 99.8%, Alfa-Aesar) in acetone with a mortar and pestle until dry. The light grey mixed powder was cold-pressed into a pellet at about 7 tons for ca. 3 min. The pellet was placed inside an open ended quartz tube that was placed at the center of a quartz tube furnace. A 90 sccm argon : 10 sccm hydrogen flow was established

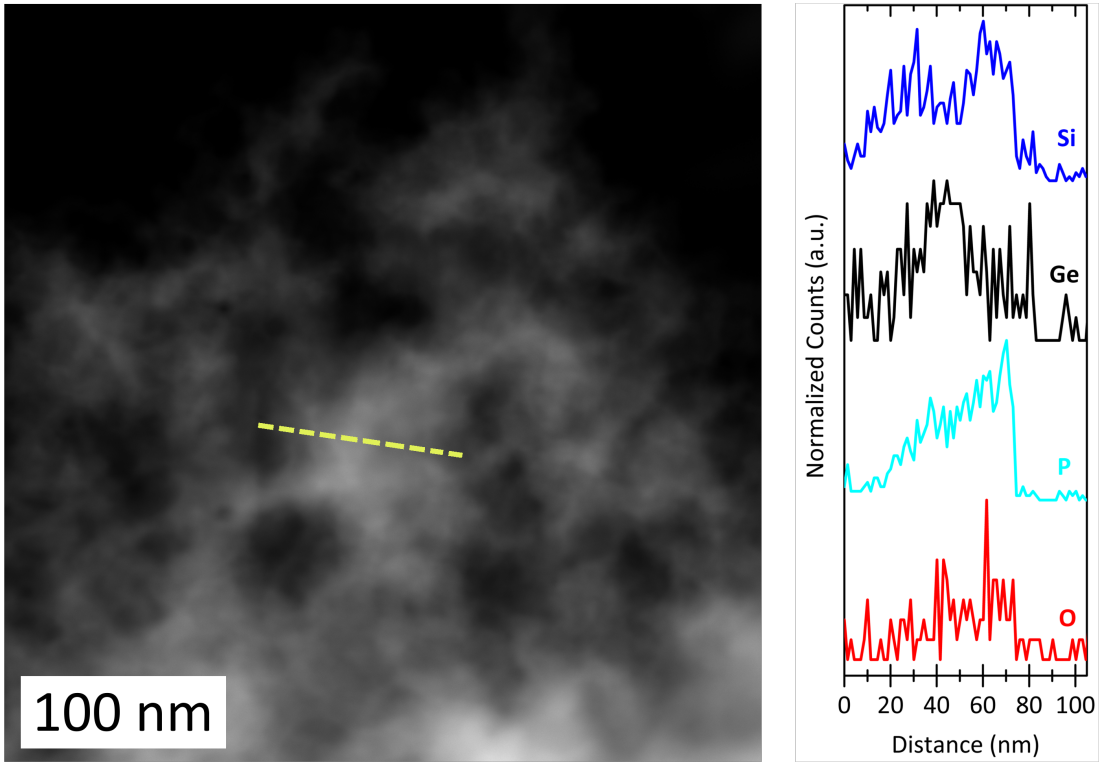

Figure 4.16: STEM image and EDX linescan of the P-doped $(SiO_2)_{80}(GeO_2)_{20}$ after calcination.

and the furnace was heated to 650 °C at 4.8 °C min^{-1}, soaked at 650 °C for 6 hours, and allowed to cool to room temperature.

Please note that later chapters will use modified conditions for the magnesiothermic reduction, as discussed in Chapter 7.

4.5.4 Powder purification through etch chemistries

All of the powder contents of the tube were collected into a centrifuge tube and soaked in aqueous hydrochloric acid solution (30 mL, 3 M) for 12 hours. The liquid was removed following centrifugation, the powder was washed again with the hydrochloric acid solution and then agitated by a bath sonicator for 20 minutes, decanted, washed once more with the hydrochloric acid solution and agitated by a bath sonicator for 20 minutes, and decanted. Then a hydrofluoric acid solution (~30 mL, 3:1 volumetric ratio of 48% aqueous hydrofluoric acid: 200 proof ethanol) was poured into the centrifuge tube with the powder. This mixture was sonicated for 20 minutes, centrifuged, decanted, and these steps repeated again. After the second HF solution had been decanted, ethanol (~30 mL, 200 proof) was added to the centrifuge tube with powder, sonicated for 20 minutes, centrifuged, decanted, and these steps were repeated again. The centrifuge tube with the wetted-powder was placed in a vacuum oven at 50 °C for at least 24 hours in order to yield a dry, purified, brown powder.

An SEM image of the powder mixture obtained after the magnesiothermic reduction of the $(SiO_2)_{90}(GeO_2)_{10}$ nanocomposite is shown in 4.17a and the hydrochloric acid cleaned podwer appears as is shown in 4.17b. The cleaned $(Si)_{90}(Ge)_{10}$ structure is porous with small, bright-looking dots decorating the surface– these dots are believe to be elemental germanium.

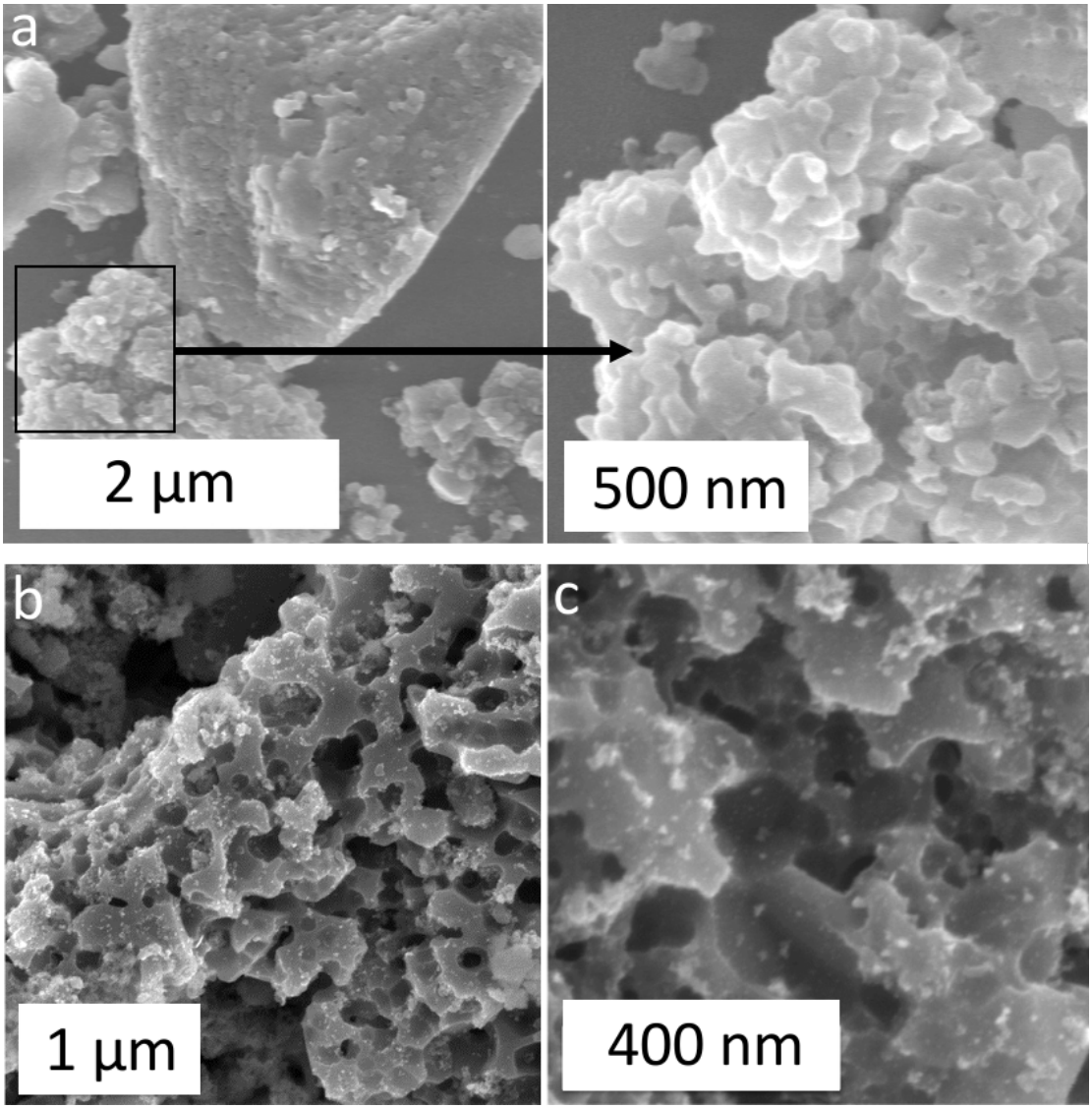

Figure 4.17: (a) SEM image of a representative region of the powder mixture obtained after the magnesiothermic reduction of the $(SiO_2)_{90}(GeO_2)_{10}$ nanocomposite and (b) after the $(Si)_{90}(Ge)_{10}$ was cleaned with hydrochloric acid. (Reprinted with permission from Snedaker et al. [128]. Copyright 2013 American Chemical Society.)

The etch chemistries remove the impurity phases, as shown in Figure 4.18. We observe a reflection from the Si(111) planes and Ge(111) and the $Si_{1-x}Ge_x$(111). The Ge(111) reflection is broader indicating a smaller domain size and compressive strain.

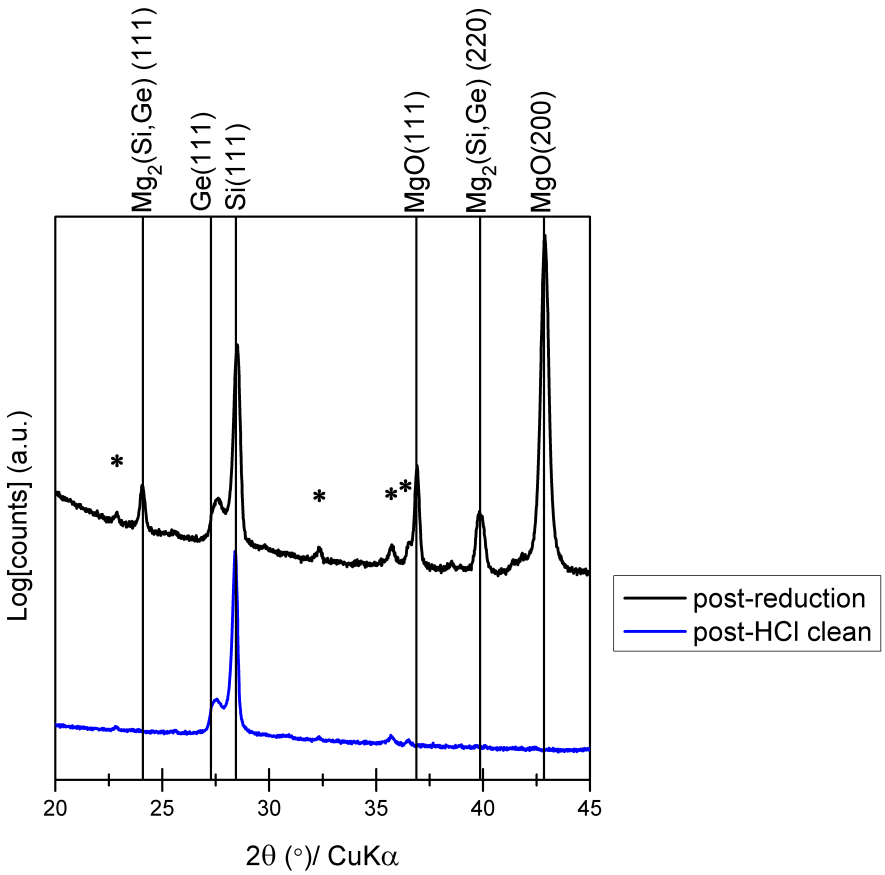

Figure 4.18: XRD patterns of the powder after the magnesiothermic reduction of the $(SiO_2)_{80}(GeO_2)_{20}$ and after the product has been cleaned with HCl. (Reprinted with permission from Snedaker et al. [128]. Copyright 2013 American Chemical Society.)

This $(Si)_{1-x}(Ge)_x$ structure may be useful for batteries according to Liu et al.[129]

4.5.5 Reduction of the "Stöber" $(SiO_2)_{1-x}(GeO_2)_x$ using intermetallic Mg_2X alloys

Ji et al. started investigating the use of intermetallic Mg_2X alloys for modified magnesiothermic reduction of silica in 2010.[130] The goal is to use the different heats of reaction for the intermetallics in order to prevent the overreduction of the silicon to the silicide.

We prepared intermetallic Mg_2Sn alloy by intimate mixing of the elemental powders and then direct reaction in a crucible placed in an argon-flow tube furnace. Powder XRD shows that (see Fig.4.19a) the intermetallic has a β–Sn phase. This intermetallic was used in a modified magnesiothermic reduction to reduce the "Stöber" $(SiO_2)_{90}(GeO_2)_{10}$. The product of that reaction was cleaned with a hydrochloric acid solution and the powder XRD of the dried product is shown in Figure 4.19a. We see that the $(Si)_{90}(Ge)_{10}$ exists with an impurity phase of β–Sn and that the reflection from Si(111) is asymmetric towards the position of the Ge(111) reflection.

Raman spectra were obtained at three different regions of the powder that appeared different under an optical microscope and are shown in Figure 4.19b.

The optical phonon of germanium is immediately recognizable. The absence of a band at 400 cm^{-1} indicates that there is no significant bonding between Si–Ge, that is, there is little to no $Si_{1-x}Ge_x$ alloy. We also observe that the region with the most tin has a silicon optical phonon band with a larger breadth and that it has shifted to lower wavenumber, indicating that the silicon near the tin-rich regions is more nanostructured than the the silicon in the tin-deficient regions.

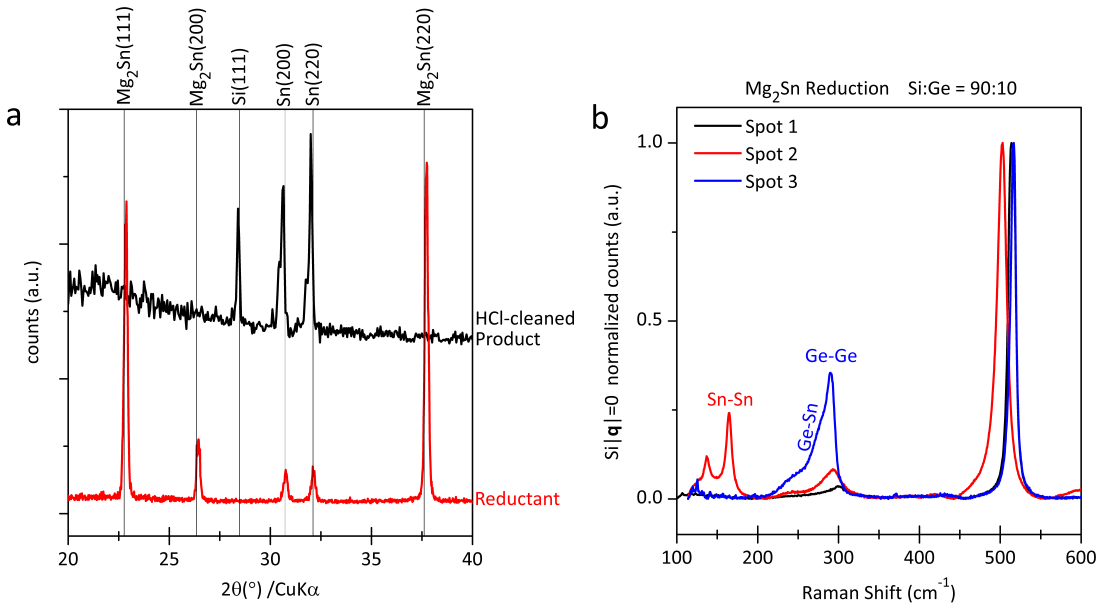

Figure 4.19: (a) Powder XRD pattern of the intermetallic Mg_2Sn reductant and hydrochloric acid cleaned $(Si)_{90}(Ge)_{10}/\beta$–Sn with asymmetric Si(111) reflection and (b) Raman spectra at three different regions in the HCl-cleaned $(Si)_{90}(Ge)_{10}/\beta$–Sn indicates phase segregation of germanium and no evidence of alloying.

It is not clear whether the presence of a β–Sn impurity phase will be beneficial for thermoelectric properties of its composite with $Si_{1-x}Ge_x$; however, I decided to abandon this method because β–Sn has a low melting point, which may complicate powder consolidation, and it cannot be etched away appreciably with hydrochloric acid. Figure 4.20 show the energy dispersive X-ray spectroscopy (EDX) maps of silicon and tin in the $(Si)_{90}(Ge)_{10}/\beta$–Sn after a hydrochloric acid clean. Since β–Sn resists corrosion by hydrochloric acid, we find metallic tin everywhere. One potential etch chemistry to increase the corrosion rate of metallic tin would be to use a hydrochloric acid solution and bubble in oxygen, as discussed by Craig et al. [131]. Craig et al. report a corrosion rate of ~100 mg cm^{-2} day^{-1} under such conditions.

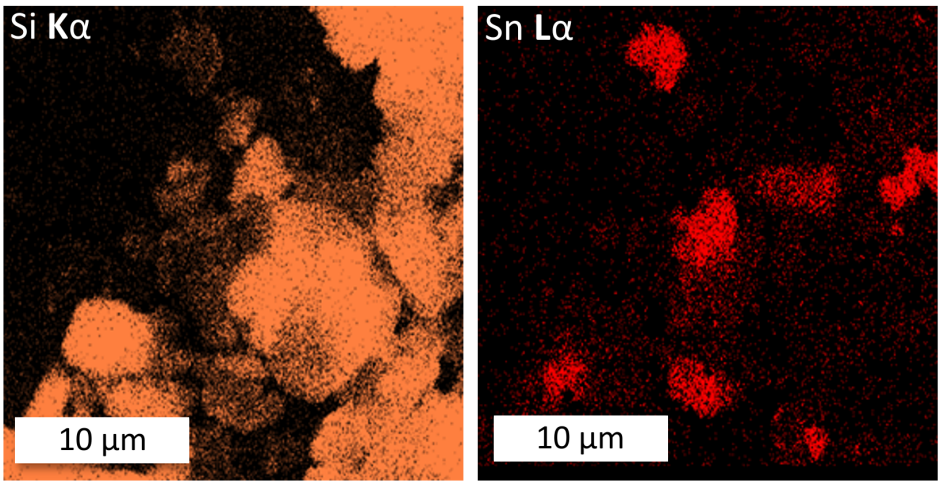

Figure 4.20: EDX map of the $(Si)_{90}(Ge)_{10}/\beta$–Sn composite prepared through a magnesiothermic reduction with the intermetallic Mg_2Sn.

Ji et al. [130] reported on the use of intermetallic Mg_2Sb and Mg_2Si as reductants for a modified magnesiothermic reduction; however, they did not discuss the use of Mg_2Sn– presumably because this study was done at UCSB.

Chapter 5

Thermoelectric properties of the hot pressed silicon germanium nanocomposites

Although this low temperature route can successfully maintain the microstructure of the precursor oxide since it occurs below silicon's melting point, we are not aware of any studies on the electronic properties of the silicon obtained by this route or application of the magnesiothermic reduction to prepare silicon-based thermoelectrics. Herein, we solve the issues of extrinsic doping and germanium incorporation and describe the first confirmation that the magnesiothermic reduction can be used to produce silicon-based thermoelectric materials, and demonstrate that this reaction may offer a low temperature, cost-effective route to prepare p-type silicon-based thermoelectric materials, with an equivalent power factor (~20 $\mu W\,cm\,K^{-2}$ at 800 °C) as the reference alloy (i.e. the one used for NASA's space missions) prepared by the conventional silicon production route.[21]

In this chapter, we focus on the doping strategy to tune the carrier density in the $Si_{1-x}Ge_x$ alloy by controllably incorporating the dopant into the precursor oxide concurrent with the direct reduction of the precursor silicon and germanium oxides. By creating an optimal carrier density for p-type $Si_{80}Ge_{20}$, the best thermoelectric power factor performance obtained using a silica precursor is comparable to the record values reported for the ball-milled material that we will refer to as BM-$Si_{80}Ge_{20}$.[21] These results suggest a new, potentially cost-effective route for the preparation of $Si_{1-x}Ge_x$ alloys that have a high thermoelectric performance. The ability to directly produce nanostructured silicon germanium from nanostructured silica and germania to eliminate time-consuming, high energy ball milling will be considered in the subsequent chapters.

We demonstrate n-type $Si_{1-x}Ge_x$; however, the thermoelectric power factor is limited due to a background concentration of holes from unintentional boron, which compensates the electrons produced by phosphorous donors.

5.1 Conventional hot pressing of $(Si)_{1-x}(Ge)_x$

5.1.1 Pelletization and pellet processing

About 0.34 grams of the $Si_{1-x}Ge_x$ powder was added to a POCO EDM-3 graphite die with an inner diameter of 1.3 cm. The die surfaces that contacted the

powder were previously coated with a boron nitride diffusion barrier. The powder was hot-pressed into a pellet at 1200 °C and 70 MPa for 2 hours. A schematic of the hot pressing tool/process is shown in Figure 5.1. The hot pressing profile and powder compression for a representative silicon germanium nanocomposite powder are shown in Figure 5.2. The pellet was removed from the die and the

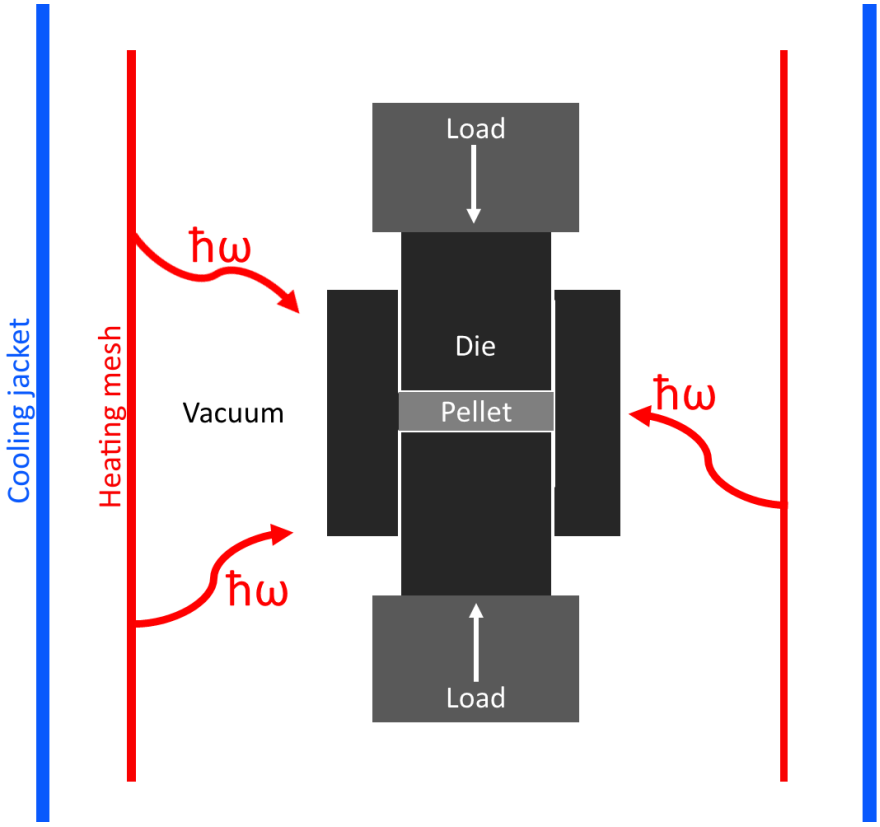

Figure 5.1: Schematic of the hot pressing process.

surface boron nitride was removed from the pellet by sanding with silicon carbide sand paper. The surface of the pellet was further polished with diamond lapping films down to at least 1 µm diamond grain size (MultiPrep, Allied High Tech,

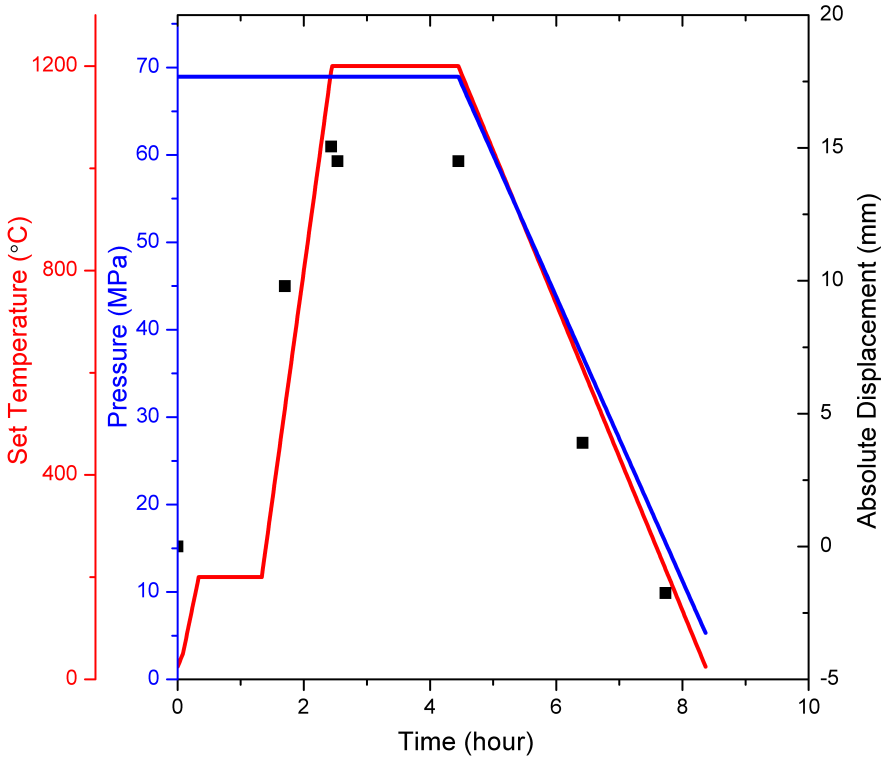

Figure 5.2: The hot pressing profile used on the silicon germanium nanocomposite powders and a representative compression profile.

Inc.). A ~1 µm × 2 µm × 10 µm bar was cut from the pellet with a low-speed saw fitted with a diamond wafering blade (Allied High Tech Products, Inc.).

5.1.2 Hot pressing alloys the Ge dots into the Si matrix to form $Si_{1-x}Ge_x$

Hot pressing the $(Si)_{80}(Ge)_{20}$, alloys the germanium into the silicon as seen in Figure 5.3. The Ge(111) reflection disappears and the Si(111) reflection shifts to $Si_{1-x}Ge_x(111)$.

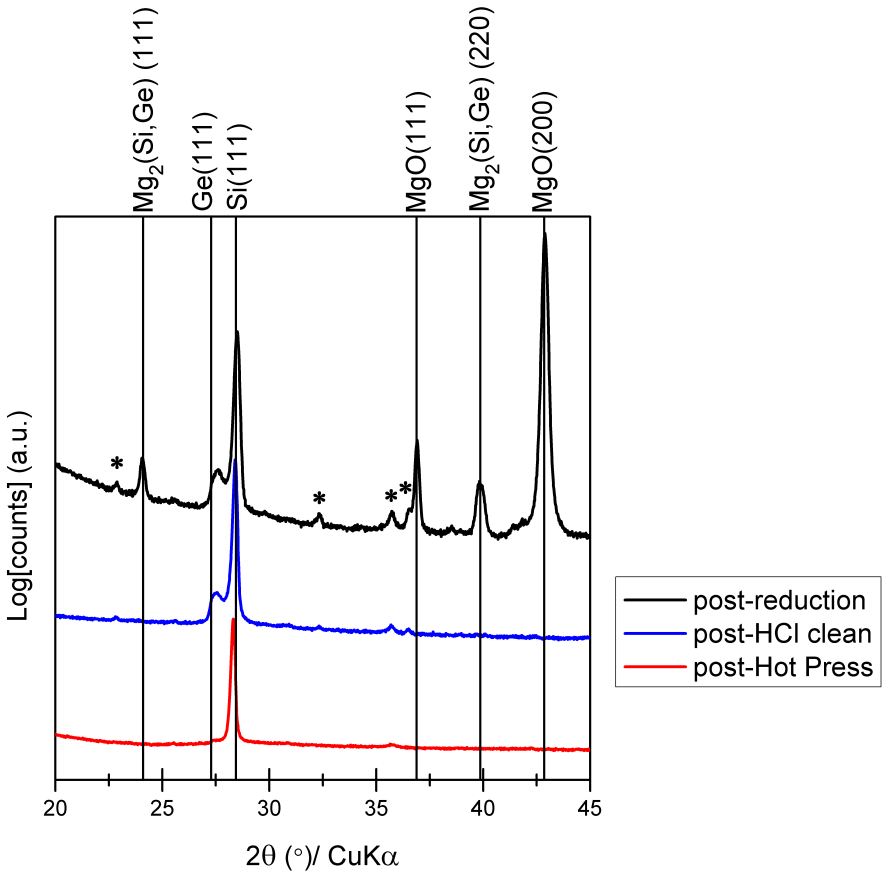

Figure 5.3: X-ray diffraction patterns of the $(Si)_{80}(Ge)_{20}$ composite after the magnesiothermic reduction, the $(Si)_{80}(Ge)_{20}$ composite after the magnesia & silicide-germanide impurity phases are removed with hydrochloric acid, and the $Si_{80}Ge_{20}$ alloy after being hot pressed. The impurity phase marked with the asterisks is assumed to be a magnesium germanium oxide phase that forms due to the high local temperature during the magnesiothermic reduction. This magnesium germanium oxide phase is assumed to transform to magnesium fluoride during the hydrofluoric acid clean which precedes the hot pressing step. (Reprinted with permission from Snedaker et al. [128]. Copyright 2013 American Chemical Society.)

XRD characterization

Lab powder diffraction data were collected on a Philips X'PERT, using the CuKα radiation wavelength of $\lambda = 1.5418$ Å and some powders were measured on a

zero-background silicon substrate. High resolution synchrotron powder diffraction data were collected at beamline 11-BM at the Advanced Photon Source (APS), Argonne National Laboratory using a wavelength of $\lambda = 0.413\,15\,\text{Å}$. Le Bail fits were performed with TOPAS Academic v4.1.17.[46]

High-resolution synchrotron powder X-ray diffraction data (Figure 5.4a) for the clean, dry $(Si)_{90}(Ge)_{10}$ powder indicate separate phases of germanium and silicon, with Le Bail fits giving an average germanium grain size of 8.5 nm and an average silicon grain size of approximately 200 nm. This phase segregation is in agreement with an observation made by Szczech et al. [132].

The average silicon grain size of 200 nm is about fifteen times larger than the grain size obtained by groups that performed the reduction on silicon dioxide nanostructures;[76, 133] however, this may be attributed to the oxide being in intimate contact with the magnesium powder (instead of the reduction relying upon Mg-vapor transport), the longer reduction time that we have used, and/or efficient crystal nucleation around the germanium nanoparticles, which form before the silicon dioxide starts to reduce. Since germanium dioxide can be reduced to germanium with hydrogen gas at temperatures below magnesium's melting point,[134] the germanium nanoparticles may act as seeds for the silicon crystallization. SEM images of the clean, dry $(Si)_{90}(Ge)_{10}$ powder show that germanium dots decorate the surface of the porous matrix (Figure 5.4c).

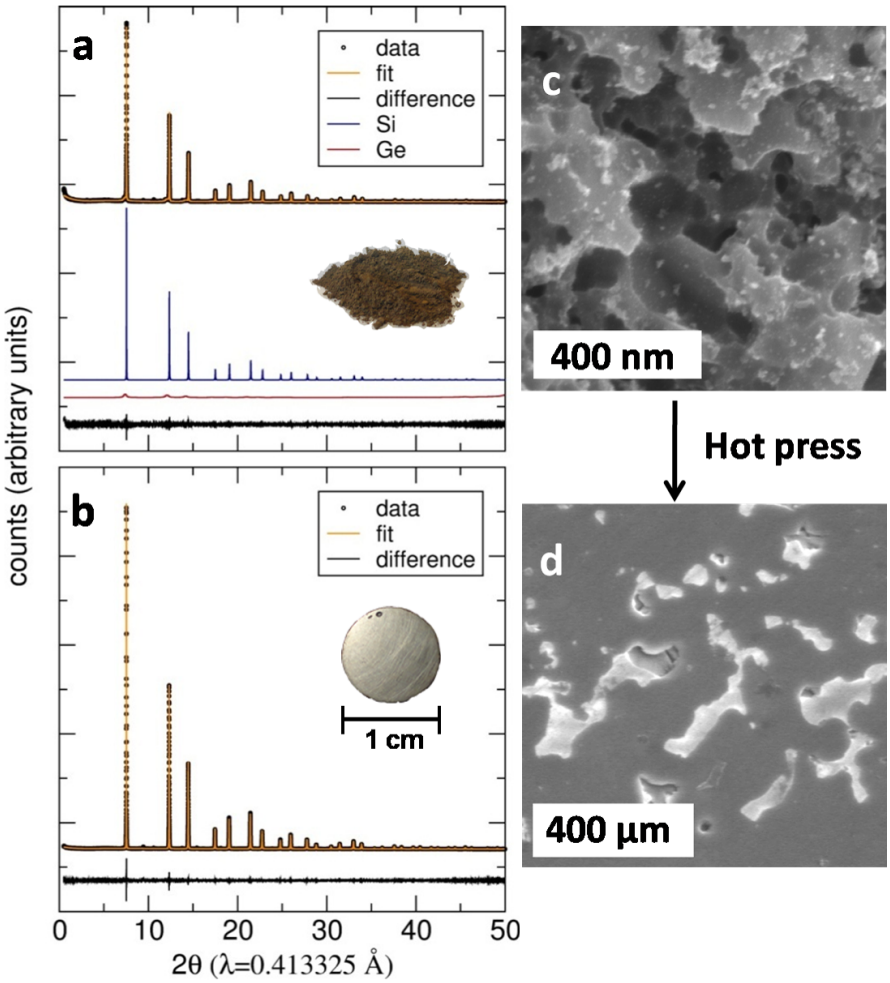

Figure 5.4: (a) Synchrotron X-ray powder diffraction data (black circles), two-phase Le Bail fit (orange line) corresponding to the segregated silicon (blue line) and germanium (red line) phases, and difference profile (black line) of the reduced, purified $(Si)_{90}(Ge)_{10}$ powder. (b) Synchrotron X-ray powder diffraction data (black circles), single-phase Le Bail fit (orange line) corresponding to the $Si_{90}Ge_{10}$ alloy and difference profile (black line) of the annealed $Si_{90}Ge_{10}$ compound. An SEM image of the reduced, purified $(Si)_{90}(Ge)_{10}$ powder appears in (c) and an SEM image of the pressed, polished $Si_{90}Ge_{10}$ pellet appears in (d). (Reprinted with permission from Snedaker et al. [128]. Copyright 2013 American Chemical Society.)

The XRD data also indicate the presence of a trace silicon carbide (SiC) impurity phase, which was significantly lessened when the oxides were calcined before the magnesiothermic reduction. The SiGe powder is consolidated into a pellet (Figure 5.4b inset) by hot pressing at 1200 °C and 70 MPa for two hours, which causes the germanium nanodots to alloy into the silicon matrix, as shown by the disappearance of the Ge reflections in the XRD pattern for the $Si_{90}Ge_{10}$ pellet (Figure 5.4b). The average $Si_{90}Ge_{10}$ grain size calculated from the single-phase Le Bail fit is 500 nm. The germanium is considered to completely alloy into the silicon because the Ge(111) reflection disappears and the lattice constant of 5.44448(1)Å calculated on the basis of the SiGe(111) diffraction peak is in agreement with the lattice constant measured for the $Si_{90}Ge_{10}$ alloy.[135]

Microscopy characterization

Field-emission scanning electron microscopy was performed on a FEI XL40 Sirion FEG microscope with an Oxford Inca X-ray system attached for energy dispersive x-ray spectroscopy. Secondary electron images were collected with an acceleration voltage of 5 kV and EDX measurements were collected with an acceleration voltage of 20 kV to distinguish between magnesium and germanium. Pellets for TEM characterization were polished with diamond lapping films to ~100 nm roughness and an electron-transparent lamella was then obtained by low-angle

milling with a FEI Focused Ion Beam Helios 600 Dual Beam with Omniprobe. Transmission electron microscopy images were obtained with an FEI T20 electron microscope at an accelerating voltage of 200 kV. TEM EDX measurements were performed with the use of a double-tilt sample holder. HAADF-STEM and EDX were performed on an FEI Titan.

After polishing the pellet (shown in the inset of Figure 5.4b) with diamond lapping films, SEM images of the sample's surface (Figure 5.4d) were obtained. The surface is characterized by regions rich in silicon germanium (darker) and lighter regions that are rich in magnesium and fluorine, as determined by energy dispersive X-ray spectroscopy with a lateral resolution of ~50 nm (EDX).

A lamella was obtained from a $Si_{90}Ge_{10}$ pellet by focused ion beam etching in order to investigate the grain sizes and grain interfaces by transmission electron microscopy. The inset of Figure 5.5a shows a TEM image of the lamella prepared from a $Si_{90}Ge_{10}$ pellet. The sample is composed of grains that range in size from tens of nanometers up to a micron. The large grains are silicon germanium. EDX measurements suggest that the silicon germanium composition is spatially homogeneous in the large grains. Figure 5.5b shows the SiGe(111) lattice planes in the large grain marked "1" (Figure 5.5).

An EDX linescan of one of the nanocrystals embedded in a $Si_{90}Ge_{10}$ grain was performed in order to confirm that it is SiC (see Fig. 5.6).

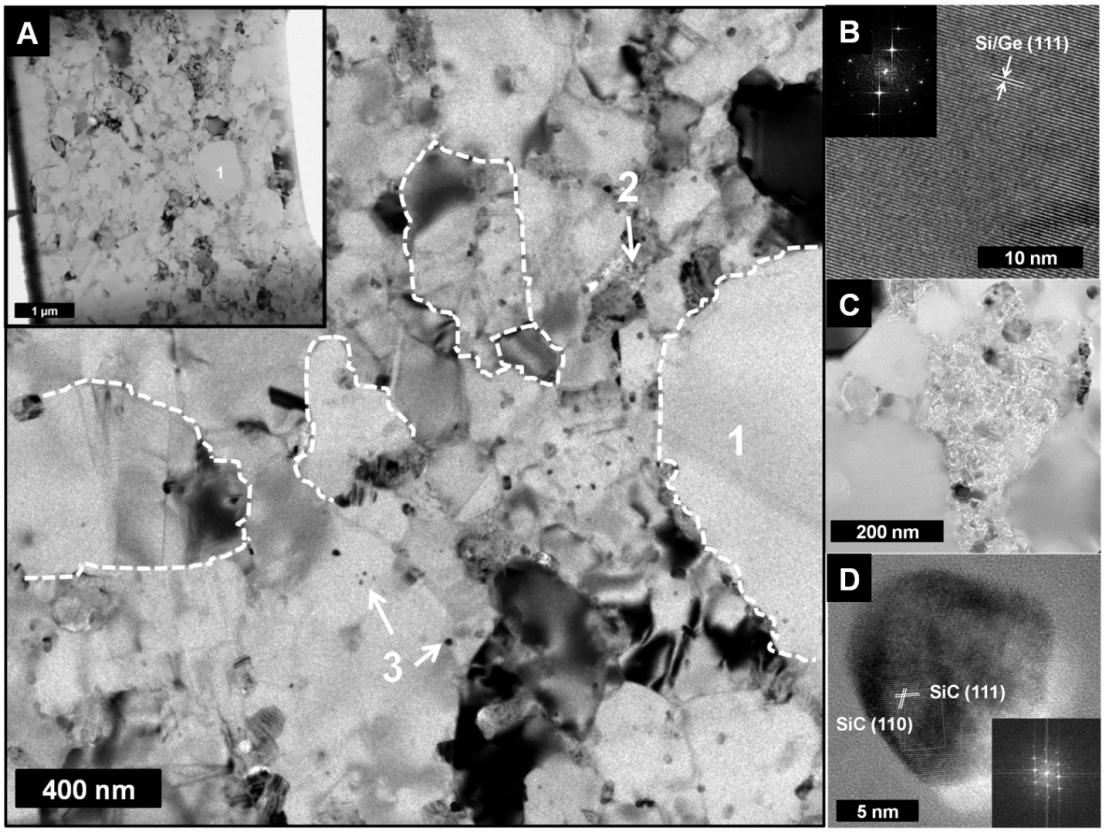

Figure 5.5: (a) TEM image of lamella prepared from a $Si_{90}Ge_{10}$ pellet by focused ion beam etching with an inset image at lower magnification and (b) HR-TEM image of the large SiGe grain marked "1", (c) a magnified image of region "2" which contains magnesium and fluorine, and (d) an HR-TEM image of the SiC nanoparticle that is embedded in the SiGe grain shown in region "3". Both of the HR-TEM images include a Fast Fourier Transform of the image as an inset. (Reprinted with permission from Snedaker et al. [128]. Copyright 2013 American Chemical Society.)

Some of the boundaries of the SiGe grains (such as region "2" which is shown magnified in Figure 5.5c) interface with an impurity phase that is rich in magnesium and fluorine, as determined by EDX. The TEM analysis also indicates that

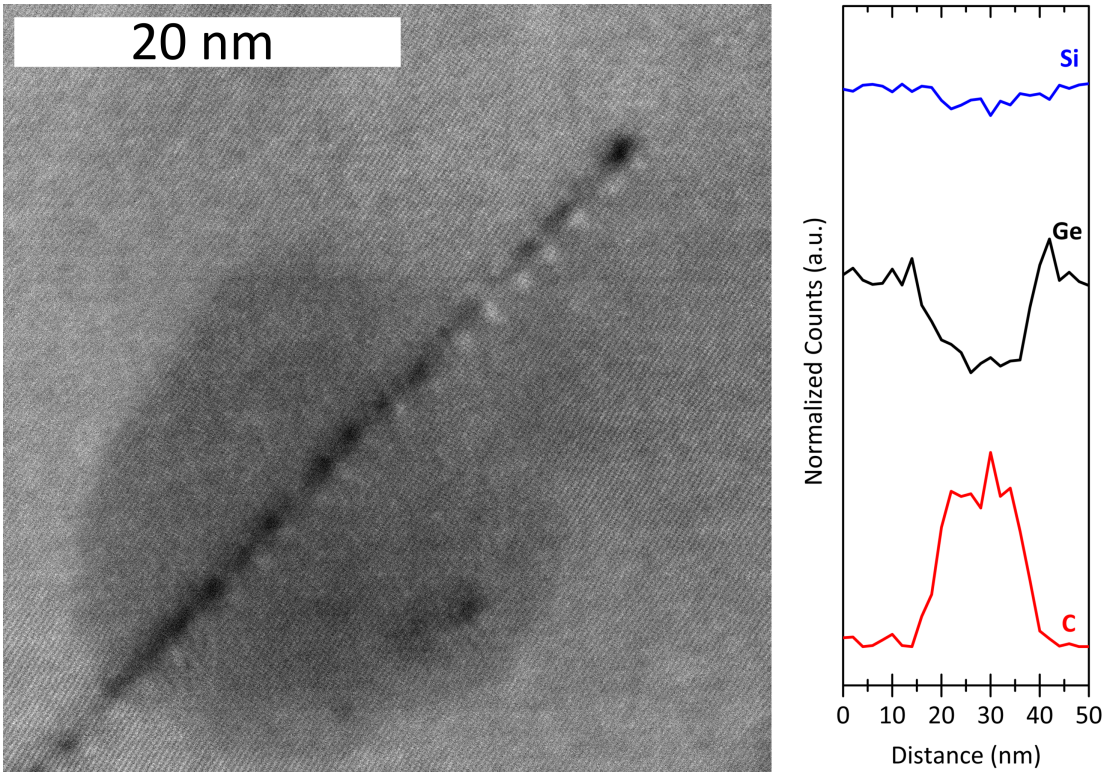

Figure 5.6: STEM image and EDX linescan of embedded SiC nanocrystal in the $Si_{90}Ge_{10}$ pellet.

the SiC impurity phase that was observed by XRD is due to SiC nanoinclusions that are embedded in the SiGe grains. Figure 5.5d shows a high resolution TEM image (HR-TEM) of an embedded SiC nanoparticle from region "3".

Secondary ion mass spectrometry

A Physical Electronics 6650 Dynamic Secondary Ion Mass Spectrometry (SIMS) system was used to measure the boron to background silicon ratio. A

relative sensitivity factor (RSF) of 4.5 $\times$ 10^{20} Si cm^{-3}, which was obtained for boron-doped, single crystal silicon, was used to estimate the boron density in the samples. The RSF are known for standards; however, the samples we are measuring have some oxygen and halide content, which affects the ionization probability of the species that we are measuring so the interpretation of the SIMS results introduces some error and we are measuring from a $Si_{1-x}Ge_x$ matrix so that introduces a systematic error.[136] Regardless, the matrices are similar and the boron densities reported here are semi-quantitative.

The effectiveness of our doping strategy is shown in Table 5.1 and in the SIMS Depth Profile (Figure 5.7), where we have demonstrated reproducibility and the ability to control the boron content over two orders of magnitude. We detect a significant amount of boron in the unintentionally-doped $Si_{90}Ge_{10}$–$[B]_1$, which we attribute to boron contamination from the glassware used during the oxide synthesis and likely boron contamination from the ammonium hydroxide's glass bottle.

Electronic and thermal transport characterization

The Seebeck coefficient and electrical conductivity in the temperature region between 35 °C and 800 °C were meas-ured simultaneously on bar-shaped samples using a ULVAC ZEM-3 M8. Thermal diffusivity was measured on pellets or half-

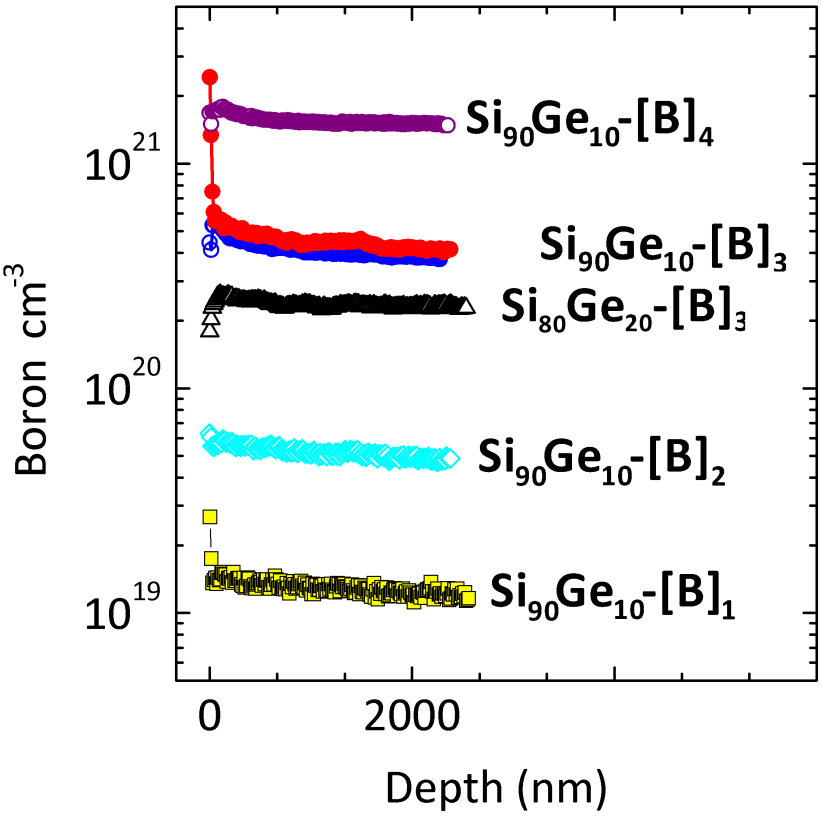

Figure 5.7: Dynamic secondary ion mass spectrometry depth profiles of boron in the $Si_{1-x}Ge_x$ pellets that were prepared with varying boron content. Two $Si_{90}Ge_{10}$–$[B]_3$ samples were measured in order to check doping reproducibility. (Reprinted with permission from Snedaker et al. [128]. Copyright 2013 American Chemical Society.)

pellets using a Netzsch laser flash apparatus (LFA 457) in the temperature region between 35 °C and 800 °C, samples were coated with a thin layer of graphite to minimize errors in the emissivity. Most of the Hall coefficients were measured by the van der Pauw method on a home-built system with 2 Tesla field; however, some were obtained on a Quantum Design PPMS with 7 Tesla field and indium contacts and gold wires to the specimens.

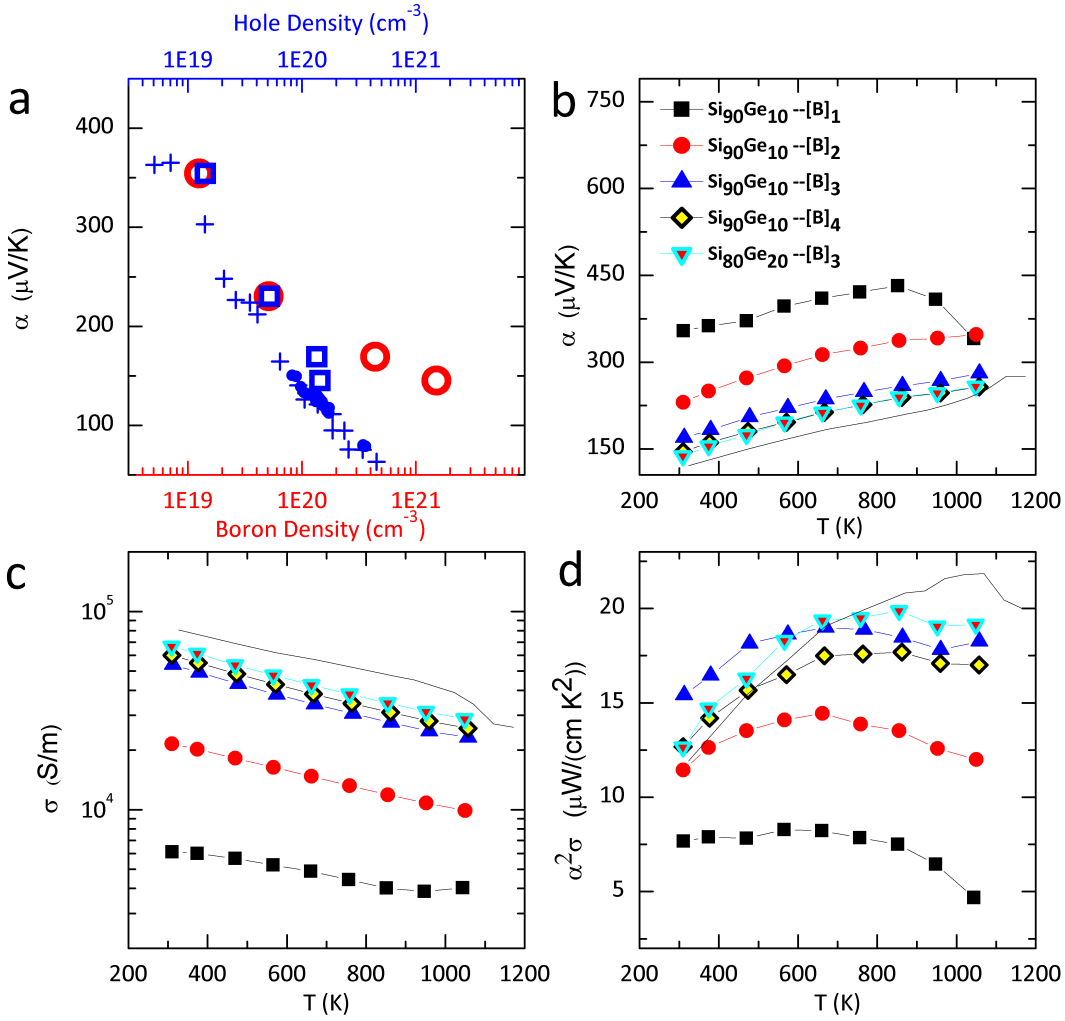

Figure 5.8: (a) Dependence of room-temperature Seebeck coefficient on the boron density (red ring) and the hole density (blue box) for the $Si_{90}Ge_{10}$ $[B]_i$ doping series, including the data reported for p-type $Si_{70}Ge_{30}$ (blue crosses),[137] and p-type $Si_{80}Ge_{20}$ (blue circles).[138] Temperature dependence of the (b) Seebeck coefficient, (c) electrical conductivity, and (d) power factor for bulk-nanostructured $Si_{1-x}Ge_x$ alloys of varying boron content. The boron content increases from $[B]_1$ to $[B]_4$. The solid trace represents the data from BM-$Si_{80}Ge_{20}$. [21] (Reprinted with permission from Snedaker et al. [128]. Copyright 2013 American Chemical Society.)

The mass-densities of the pellet samples were determined by the Archimedean method. The measured densities are greater than 94% of the corresponding alloy's density. The Si:Ge ratio and the atomic percentage of magnesium were characterized by EDX measurements on several regions across the samples' surfaces. The densities and atomic compositions data for the samples discussed in this paper are provided in Table 5.1. The densities of the samples are all high enough such that their effective thermoelectric properties are representative of their host thermoelectric properties (see Appendix A).

5.1.3 Thermoelectric characterization of p-type $Si_{1-x}Ge_x$

As the thermoelectric properties of a material are strongly dependent upon the carrier density, we used our doping strategy to prepare a doping series for the $Si_{90}Ge_{10}$ composition ($Si_{90}Ge_{10}$–$[B]_i$). The hole density and mobility in the samples were meas-ured by the van der Pauw method.[62] The boron incorporation strategy we have developed is observed to be an effective means of tuning the carrier density, as seen in Table 5.1, where the hole density increases with the boron density measured by SIMS. We achieved an optimal hole density in the $Si_{90}Ge_{10}$ composition, which is also close to the previously determined optimal level (~1.5× 10^{20} cm^{-3}) for $Si_{80}Ge_{20}$.[138]

With a knowledge of the boron content that produces an optimal carrier density in a $Si_{90}Ge_{10}$ alloy and because the optimal carrier density does not vary significantly with the alloy composition,[139] we prepared a $Si_{80}Ge_{20}$ sample with a near-optimal carrier density so that we could compare the thermoelectric properties of the material prepared by our magnesiothermic reduction route to a $Si_{80}Ge_{20}$ nanocomposite prepared by the ball-milling route.[21]

The electrical conductivity and Seebeck coefficient were measured from room temperature to 800 °C on a ~1 mm × 2 mm × 10 mm bar that was diced from each pellet with a low-speed saw fitted with a diamond wafering blade. The room temperature Seebeck coefficients for the $Si_{90}Ge_{10}$–$[B]_i$ doping series are plotted as a function of carrier density and boron density in Figure 5.8a, showing that the Seebeck coefficient decreases with increasing carrier density. Our results for this doping series agree well with previously reported carrier density dependent Seebeck coefficient measurements on p-type $Si_{80}Ge_{20}$ and p-type $Si_{70}Ge_{30}$.[137, 138] The discrepancy between hole density and boron density for the two highest doped samples is likely due to boron precipitation, which limits the number of electrically active boron atoms and thus, the hole density. The hole density in the highest doped sample (i.e. $Si_{90}Ge_{10}$–$[B]_4$) is an order of magnitude lower than the boron density due to the solubility limit of boron in this alloy.

Up to 800 K, the Seebeck coefficients for the $Si_{90}Ge_{10}$–$[B]_i$ series and the optimally doped $Si_{80}Ge_{20}$ alloy (Figure 5.8b) increase with increasing temperature, with the exception of the $Si_{90}Ge_{10}$–$[B]_1$ sample, where a maximum of Seebeck coefficient was observed around 800 °C due to the contribution from minority carriers in lightly doped samples.

The electrical conductivities of the $Si_{90}Ge_{10}$–$[B]_i$ doping series and the optimally doped $Si_{80}Ge_{20}$ alloy are presented in Figure 5.8c. With increasing boron content in the $Si_{90}Ge_{10}$–$[B]_i$ doping series, we observed increasing electrical conductivity. The electrical conductivity for the optimally doped $Si_{90}Ge_{10}$ is comparable to the optimally doped $Si_{80}Ge_{20}$. The electrical conductivity of all of the samples decreases as a function of temperature, which is expected for degenerately doped semiconductors. The optimally-doped $Si_{90}Ge_{10}$-$[B]_3$ exhibits an approximately 80% increase in power factor at 1000 K compared to the unintentionally-doped $Si_{90}Ge_{10}$–$[B]_1$ (Figure 5.8d). Our high-temperature power factor for the optimally-doped $Si_{80}Ge_{20}$–$[B]_3$ alloy is $\sim 20\,\mu W\,cm\,K^{-2}$ in the temperature range from 700 K to 1000 K, approximately 10% lower than that reported for BM–$Si_{80}Ge_{20}$.[21]

The thermal diffusivities of the $Si_{1-x}Ge_x$ alloys were measured by the laser flash method from room temperature to 800 °C. The thermal conductivity was determined from the product of the temperature-dependent thermal diffusivity,

Hot Pressed Sample	EDX Si:Ge	EDX Mg (at.%)	Density (g cm^{-3})^b	SIMS B Density (B cm^{-3})	Hole Density (cm^{-3})	Hole Mobility ($cm^2V^{-1}s^{-1}$)
$\mathbf{Si_{90}Ge_{10}}$**-[B]**$_1$	89:11	5.0	2.58 (96.2%)	1.25×10^{19}	1.42×10^{19}	31
$\mathbf{Si_{90}Ge_{10}}$**-[B]**$_2$	92:8	3.8	2.54 (94.7%)	5.09×10^{19}	5.18×10^{19}	29
$\mathbf{Si_{90}Ge_{10}}$**-[B]**$_3$	92:8	3.3	2.58 (96.2%)	4.39×10^{20}	1.35×10^{20}	29
$\mathbf{Si_{90}Ge_{10}}$**-[B]**$_4$	91:9	3.7	2.63 (98.0%)	1.52×10^{21}	1.44×10^{20}	27
$\mathbf{Si_{80}Ge_{20}}$**-[B]**$_3$	82:18	1.1	2.97 (98.8%)	2.32×10^{20}	1.55×10^{20}	28

Table 5.1: Summary of the compositional and carrier properties of the hot pressed samples. ^{a}The relative standard deviations are <5% for SIMS B density, ~1% for the hole density, and ~1% for hole mobility, respectively. ^{b}The mass-density column includes the density relative to the theoretical density for the nominal Si:Ge composition.[135] (Reprinted with permission from Snedaker et al. [128]. Copyright 2013 American Chemical Society.)

the room temperature mass-density, and the temperature dependent heat capacity measured by Amano *et al.* for the $Si_{80}Ge_{20}$ composition (for the $Si_{90}Ge_{10}$ composition, the heat capacity was estimated using the Dulong-Petit value, which slightly underestimates the heat capacity).[140] For the carrier density range explored in the $Si_{90}Ge_{10}$–$[B]_i$ doping series, the $[B]_1$ sample is the only one to exhibit a bipolar contribution to the thermal conductivity at temperatures greater than 900 K (Figure 5.9a). However, the thermal conductivities of the $[B]_2$, $[B]_3$, and $[B]_4$ $Si_{90}Ge_{10}$ alloys do not increase in the order of increasing electrical conductivity as one would expect from the Wiedemann-Franz law. This trend may

be due to differences in microstructure (including porosity and impurity content), or electron-phonon scattering with increasing carrier density, which occurs in this degenerate-doping regime.[141] The $Si_{80}Ge_{20}$–$[B]_3$ alloy is expected to have a lower thermal conductivity than the $Si_{90}Ge_{10}$ samples; however, the thermal conductivity of the $Si_{90}Ge_{10}$ samples is estimated using the heat capacity from the Dulong-Petit value, which underestimates the heat capacity and hence the thermal conductivity.

The thermal conductivity of our optimally doped $Si_{80}Ge_{20}$ alloy at 800 °C is approximately 10% lower than the thermal conductivity reported for a non-nanostructured, optimally doped p-type $Si_{80}Ge_{20}$ radioisotope thermoelectric generator (RTG) used for space missions.[21, 138] However, compared to BM–$Si_{80}Ge_{20}$, the grain sizes in the samples reported here are almost 30 times larger, which leads to our $Si_{80}Ge_{20}$ alloy having a thermal conductivity at 800 °C that is about 50% higher than the ball-milled and hot-pressed nanocomposite. The larger grain sizes are due to the synthetic conditions we have employed and the dramatic grain growth during the consolidation process (2 hours at 1200 °C and 70 MPa). The grain size may be minimized by using vapor transport for the magnesiothermic reduction and by using a more rapid consolidation process such as spark plasma sintering or rapid hot pressing.[142]

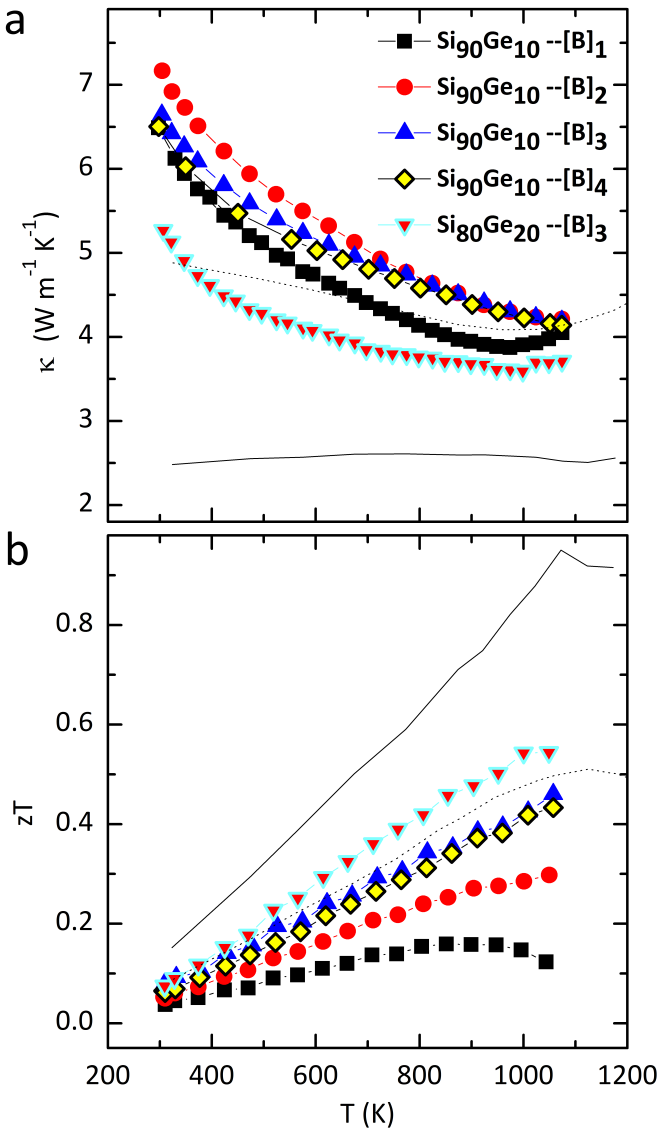

Figure 5.9: Temperature dependence of the (a) thermal conductivity and (b) thermoelectric figure of merit for $Si_{1-x}Ge_x$ alloys of varying boron content prepared by magnesiothermic reduction of a silica-germania nanocomposite. The thermal conductivity is calculated from thermal diffusivity, Archimedean density, and the relevant heat capacity (i.e. the literature-reported, temperature-dependent heat capacity of $Si_{80}Ge_{20}$ or the Dulong-Petit value for $Si_{90}Ge_{10}$). The dotted trace represents the data for RTG–$Si_{80}Ge_{20}$ and the solid trace represents the data for BM–$Si_{80}Ge_{20}$from Joshi et al. [21] (Reprinted with permission from Snedaker et al. [128]. Copyright 2013 American Chemical Society.)

The zT values of the $Si_{1-x}Ge_x$ alloy that we prepared via magnesiothermic reduction of a boron-doped silica-germania nanocomposite are shown as a function of temperature in Figure 5.9b. The optimally doped $Si_{80}Ge_{20}$ alloy has a zT of 0.5 (800 °C). The maximum zT for our $Si_{80}Ge_{20}$ alloy is in agreement with the RTG material (0.5 at 800 °C) but about 40% lower than the zT (800 °C) of 1 for the nanostructured bulk BM–$Si_{80}Ge_{20}$ alloy, as a result of the larger grain size in our alloy.[21, 138] The maximum power factor of our optimally-doped $Si_{80}Ge_{20}$ alloy is in agreement with the RTG material (~20 $\mu W\,cm\,K^{-2}$ at 800 °C).

5.1.4 Conclusions

In summary, p-type $Si_{1-x}Ge_x$ alloys prepared by hot-pressing the product from a magnesiothermic reduction of a boron-doped silica germania nanocomposite have been shown to have comparable thermoelectric properties to p-type $Si_{1-x}Ge_x$ alloys prepared by the conventional carbothermal reduction route. The carrier density and electronic properties were tuned by varying the boron content in the precursor oxide, which resulted in a power factor that is competitive with the record values in compositionally homogeneous p-type $Si_{80}Ge_{20}$ nanocomposites. The large grain size in our alloys results in a relatively high thermal conductivity, which is currently the limiting factor in the thermoelectric efficiency of our alloys. We expect the figure of merit to be further enhanced by mini-

mizing the grain growth during the magnesiothermic reduction and consolidation process– these strategies are addressed in Chapter 7 and Chapter 6, respectively.

5.2 n-type doping control via silica-germania nanocomposite synthesized in the presence of H_3PO_3

Samples of $(SiO_2)_{1-x}(GeO_2)_x$ were prepared and phosphorus-containing acids were injected according to the procedure described in Chapter 4. The phosphorus-doped $(SiO_2)_{1-x}(GeO_2)_x$ was reduced as described in Chapter 4 and hot pressed and processed as described above.

5.2.1 Thermoelectric properties of n-type $Si_{1-x}Ge_x$ prepared by the magnesiothermic reduction of a phosphorus-doped silica-germania nanocomposite

When no phosphorus-containing acid was added (i.e. $Si_{90}Ge_{10}$–$[P]_1$), the Seebeck coefficient indicates the material is p-type, as shown in Figure 5.10a. The use of phosphoric acid (i.e. $Si_{90}Ge_{10}$–$[P]_2$) produces a p-type material that has a decreasing Seebeck coefficient with increasing temperature– this is possibly due

to the elemental phosphorus being phase segregated and with increasing temperature it is solubilized, ionizing to give electrons that sequentially compensate the hole density. The use of phosphorous acid (i.e. $Si_{90}Ge_{10}$–$[P]_3$), produces an n-type material that when sufficiently doped (i.e. $Si_{90}Ge_{10}$–$[P]_4$), exhibits a Seebeck coefficient that is competitive with the Seebeck coefficient of the literature record for n-type BM-$Si_{80}Ge_{20}$.[20] Figure 5.10 shows the temperature dependent electrical conductivities. $Si_{90}Ge_{10}$–$[P]_2$ exhibits "metal-like" temperature dependence, whereas $Si_{90}Ge_{10}$–$[P]_2$ and $Si_{90}Ge_{10}$–$[P]_3$ exhibit thermally activated conductivity. The thermally activated conductivity is probably due to electrons from the phosphorus compensating a background hole density and then with increasing temperature more free carriers are generated. $Si_{90}Ge_{10}$–$[P]_4$ exhibits a "metal-like" temperature dependence; however, the maximum is significantly lower than the similarly doped n-type BM-$Si_{80}Ge_{20}$ considering the value of the Seebeck coefficient. This reduction of the electrical conductivity in $Si_{90}Ge_{10}$–$[P]_4$ is likely due to compensation from a background boron content of $\sim 10^{19}$ Boron cm^{-3} that we measured by SIMS in the pellet that was not intentionally doped with anything. The consequence of the compensation of ~10–40% of the donor states is the degradation of the electrical conductivity and the thermoelectric power factor of the material prepared using our current sol-gel process.

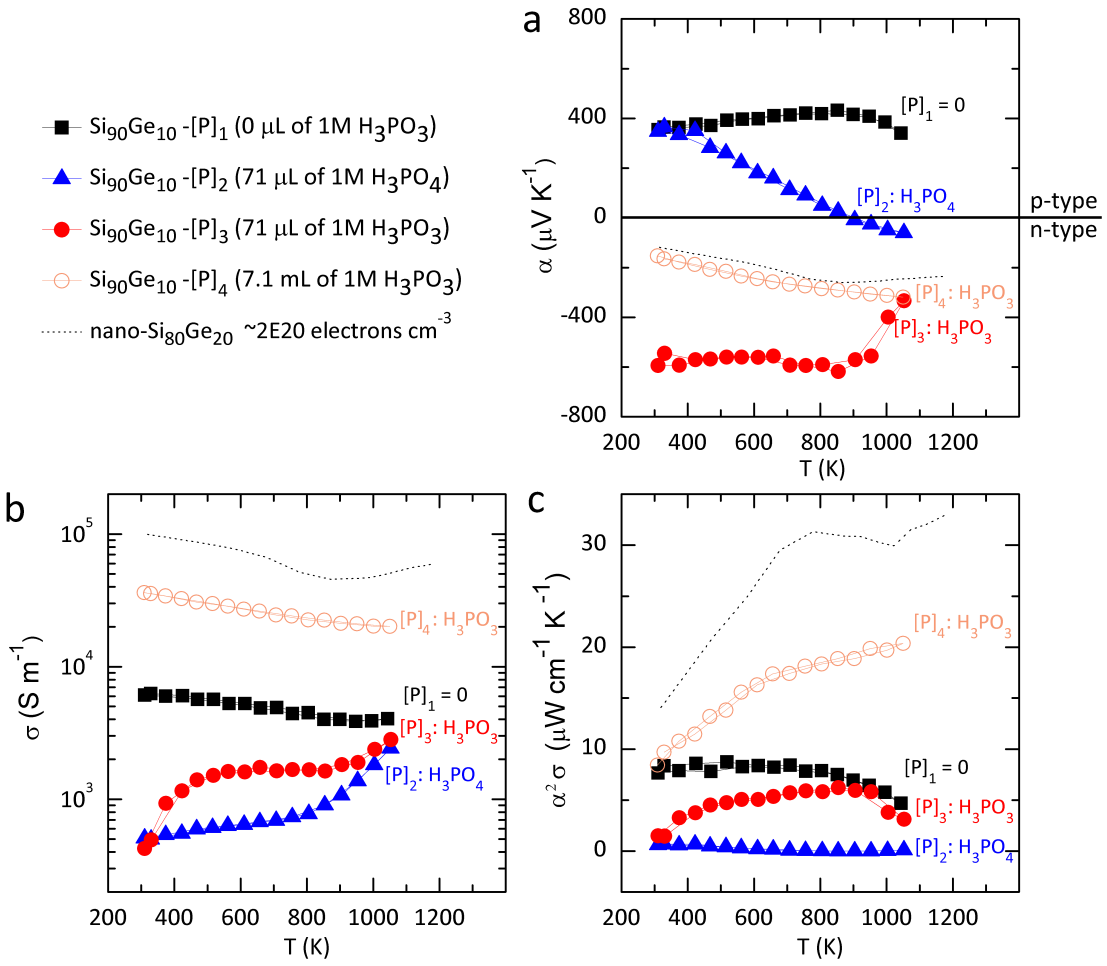

Figure 5.10: Temperature dependence of the (a) Seebeck coefficient, (b) electrical conductivity, and (c) power factor for bulk-nanostructured $Si_{1-x}Ge_x$ alloys of varying phosphorus content. The phosphorus contents were achieved based on the information in the legend. The dotted trace represents the data for BM-$Si_{80}Ge_{20}$ from Wang et al. [20].

5.2.2 The phosphorus content

Attempts to quantify the phosphorus content by dynamic SIMS were unsuccessful due to the mass interference components in the secondary ion signal (i.e. $^{12}C^{18}F^{+}$ and $^{30}SiH^{+}$).[136] However, as of November 2014 at UC Santa Barbara, it should be possible to distinguish the phosphorus ions due to the installation of a magnetic sector detector with higher resolution than the previous quadrupole mass analyzer.

5.2.3 Reducing the background boron content to improve thermoelectric power factor

If the background concentration of boron were reduced, then there would be less compensation of the donor impurities; thus, the power factor would be higher for our n-type $Si_{1-x}Ge_x$. I believe that the source of the background boron content is the ammonium hydroxide solution's bottle, which is borosilicate glass. The ammonia may cause borates to leach into the solution and then during the sol-gel process, the borates may become part of the silicate network. Strategies to avoid this contamination would be to use ammonia solution from a plastic bottle and/or use a catalyst that won't introduce impurities.

Chapter 6

Current Assisted Pressure Activated Densification of $(Si)_{1-x}(Ge)_x$

An alternative powder consolidation technique to hot pressing is current activated pressure assisted densification (CAPAD) aka spark plasma sintering (SPS) aka field assisted sintering (FAST), where a load is applied to the powder and a current is passed through it, giving rise to a large heating rate and short pressing time. CAPAD has been applied to the densification of ceramic powders and materials systems that don't easily sinter by other pressing methods.[143, 144] Although, there is no evidence of a spark or plasma during CAPAD, the process is commonly called SPS.

6.1 The SPS process

Spark plasma sintering has been applied to prepare half-Heusler/full-Heusler thermoelectrics.[145] Reactions can also be performed, as exemplified by the SPS synthesis of Magnéli phase thermoelectrics with reduced lattice thermal conductivity.[146, 147] For SPS, the powder is placed in the graphite die and graphoil is used as a diffusion barrier (see Fig. 6.1a). The die is placed in the SPS chamber, which may be evacuated, and then the pressing program is initiated, resulting in aggregates of crystallites being pressed against each other so that mass transfer occurs between the crystallites due to the applied current and load (see Fig. 6.2) so that the domains ripen and a robust pellet may be obtained.

6.2 Heterogeneous alloying of $(Si)_{1-x}(Ge)_x$ during SPS

6.2.1 XRD

The $(Si)_{80}(Ge)_{20}$ powder was spark plasma sintered according to the pressing profile shown in Figure 6.3– densification was achieved in ~20 minutes. Powder XRD of the SPS-$(Si)_{80}(Ge)_{20}$ (see Fig. 6.4) shows an asymmetric Si(111) reflection

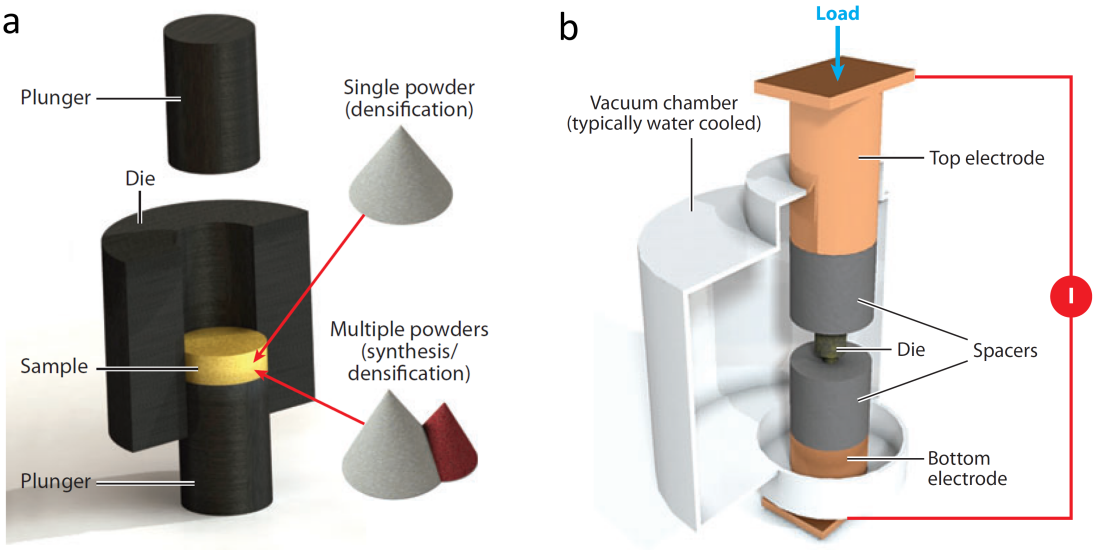

Figure 6.1: The procedure for SPS: (a) graphite die and powder or powders to be pressed and (b) the setup for the die inside the SPS system. (Figures taken from Garay [144].)

towards the Ge(111) reflection and there is an impurity phase which may be elemental germanium or a crystalline magnesium fluoride impurity.

6.2.2 Microscopy

The granular structure of the SPS'd $(Si)_{80}(Ge)_{20}$ is visible by eye and optical micrographs show porosity that is characteristic of the presence of a liquid during solidification, as shown in Figure 6.5.[148] EDX showed that the SPS'd $(Si)_{80}(Ge)_{20}$ had lost some germanium relative to the starting powder, such that it became SPS-$(Si)_{85}(Ge)_{15}$. FIB was used to pull a lamella from a large grain

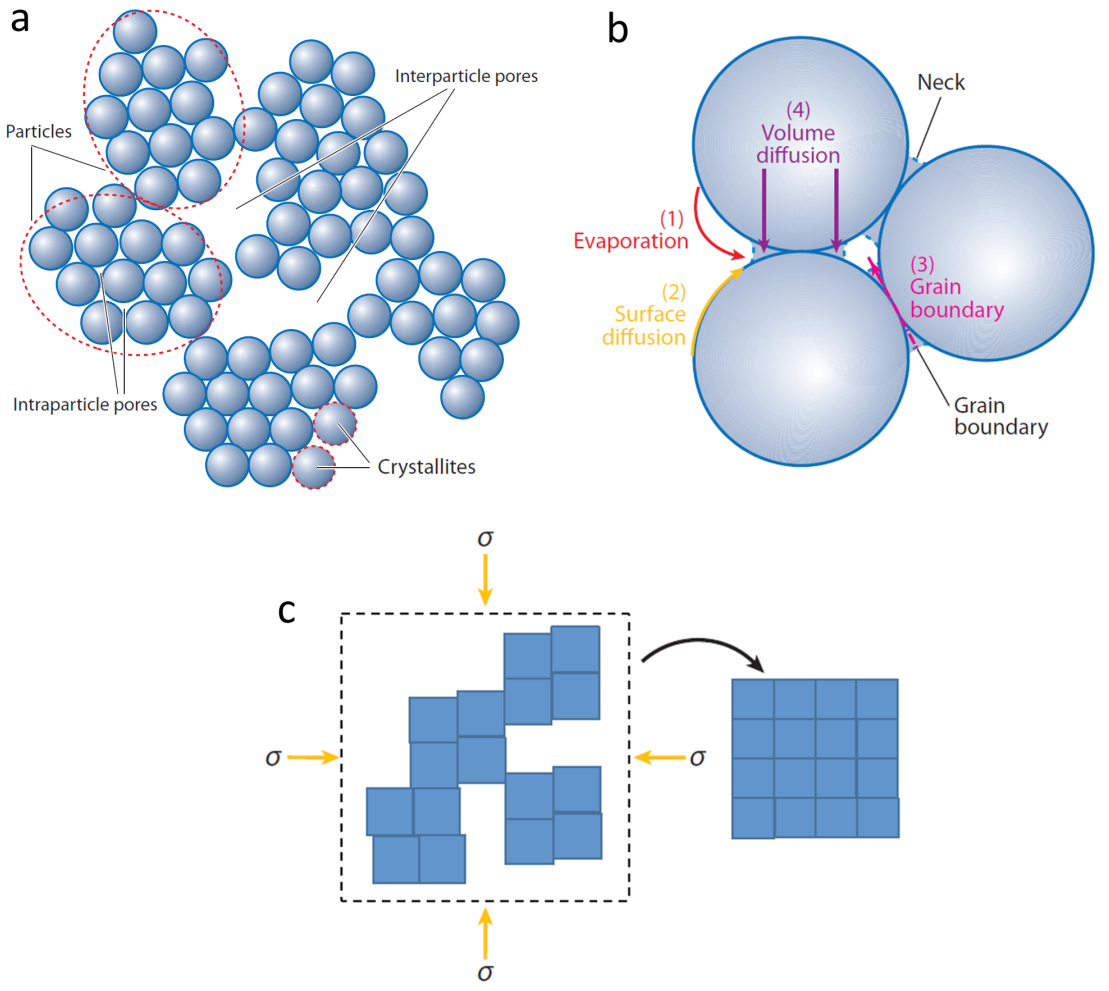

Figure 6.2: The mechanism of consolidation for SPS, as presented by Garay: (a) aggregates of crystallites are pressed against each other under a load, (b) mass transfer occurs between the crystallites due to the applied current and load, and (c) as domains ripen, they form a consolidated, granular pellet. (Figures taken from Garay [144].)

region and analysis by TEM (Fig. 6.6) indicates the lamella is a single crystal with a high dislocation density. FIB was used to pull a lamella from a smaller

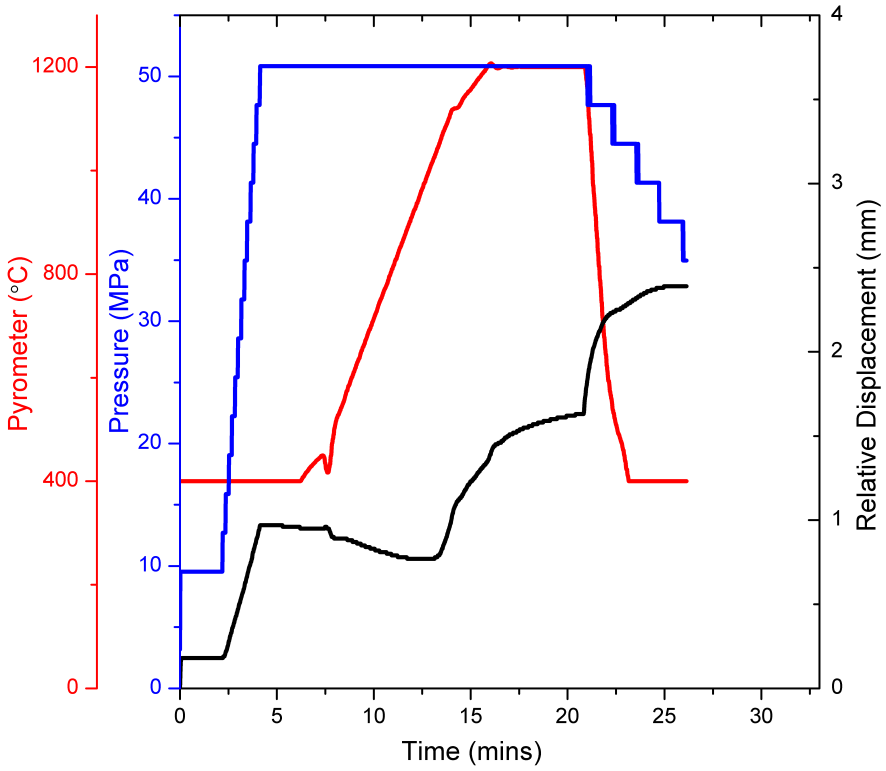

Figure 6.3: The SPS profile that was used to consolidate the $(Si)_{1-x}(Ge)_x$ powder.

grain region and analysis by TEM (Fig. 6.7) indicates the lamella is a polycrystalline and porous. We wanted to determine the location and distribution of the elemental germanium phase that XRD suggested but we did not observe a germanium phase. Figure 6.8a shows a HAADF-STEM image of a grain that appears in 6.7b. An EDX linescan from the center of the grain to the grain boundary indicated that the grain was heterogeneously alloyed, with germanium localized to near the grain boundary. The Z-contrast in Figure 6.8c confirms the existence of germanium primarily at the grain boundary.

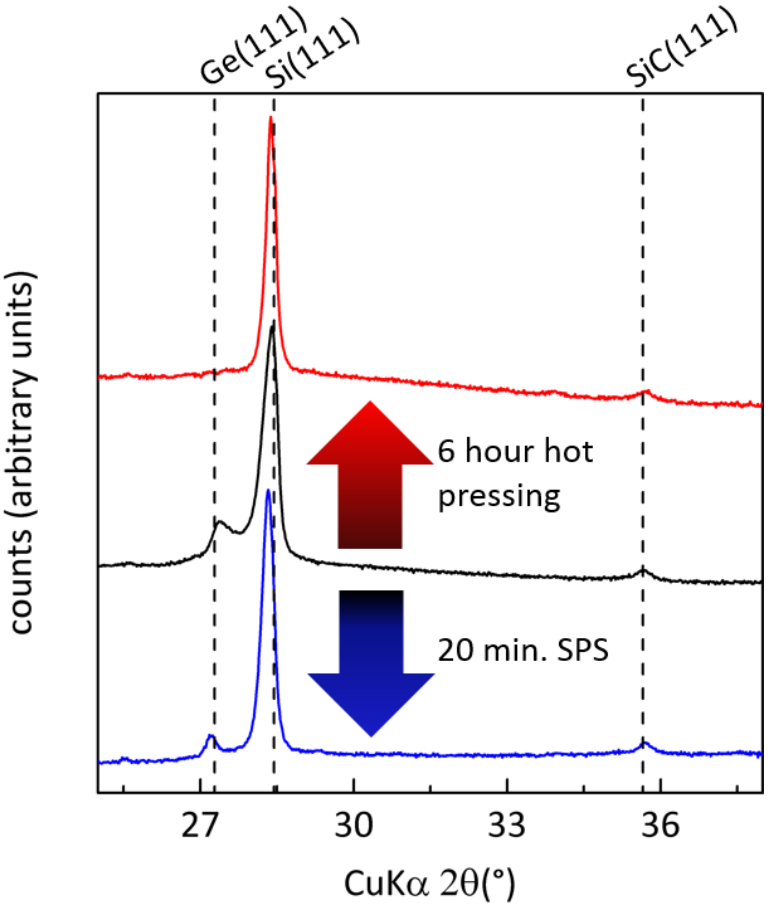

Figure 6.4: Powder XRD patterns of the pellets prepared by hot pressing the $(Si)_{80}(Ge)_{20}$ or spark plasma sintering the $(Si)_{80}(Ge)_{20}$.

6.2.3 Electronic properties

Dynamic SIMS of the SPS–$(Si)_{85}(Ge)_{15}$–$[B]_3$ pellet suggests that the boron density is in good agreement with the similarly doped hot pressed pellets and that the boron density is uniform through the pellet (see Fig. 6.9). The compositional and carrier properties of the similarly doped hot pressed samples compared to the SPS'd sample are shown in Table 6.1. The SPS'd pellet has a higher boron

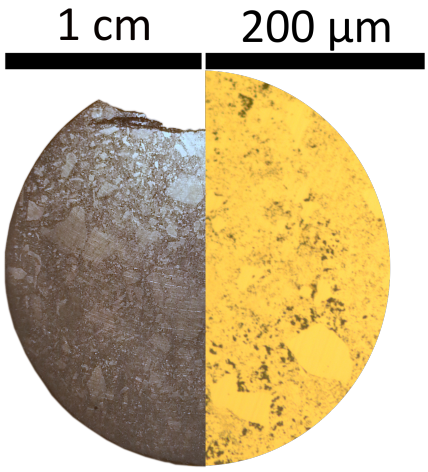

Figure 6.5: Photograph and optical micrograph of the pellet obtained after SPS of the $(Si)_{80}(Ge)_{20}$. Large grains are visible and so are porous regions that are indicative of the presence of liquid during solidification.

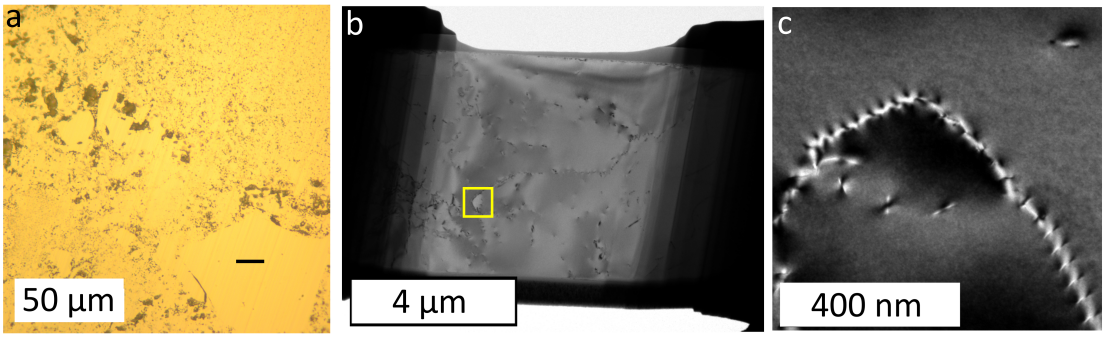

Figure 6.6: (a) Optical microscope image of the surface of the SPS-$(Si)_{85}(Ge)_{15}$ with a large grain visible, (b) bright field TEM image of a *single crystal* lamella that was plucked from a large grain region similar to that shown by the line in (a), and a higher resolution weak-beam condition image to accentuate the dislocations in this single crystal lamella.

density, higher hole density, and lower Hall mobility than the hot pressed pellets.

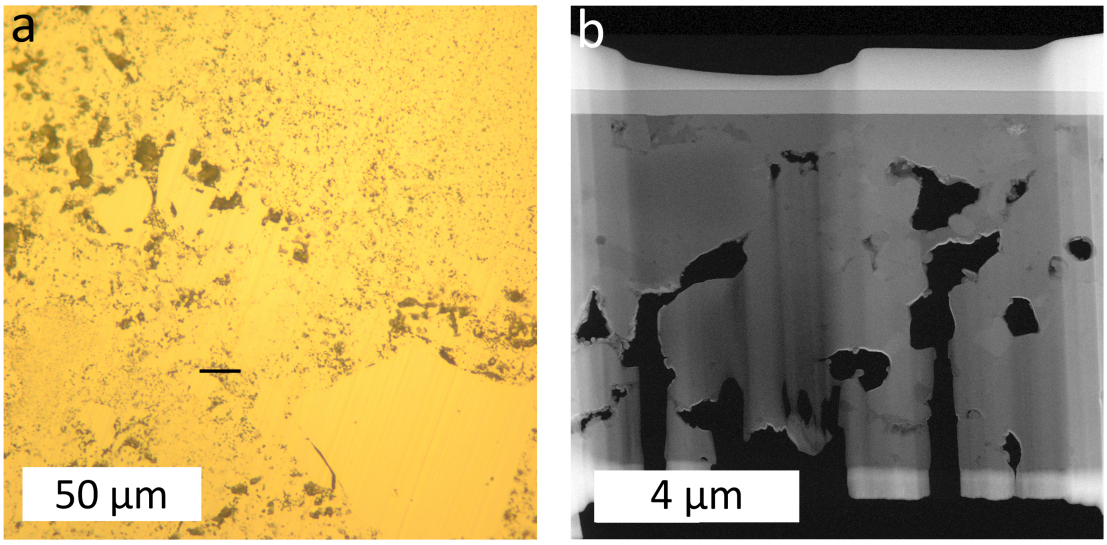

Figure 6.7: (a) Optical microscope image of the surface of the SPS-$(Si)_{85}(Ge)_{15}$ with porous regions visible and a (b) STEM image of a *polycrystalline* lamella that was plucked from a region similar to that shown in (a).

Hot Pressed Sample	EDX Si:Ge	EDX Mg (at.%)	Density (g cm^{-3})^a	SIMS B Density (B cm^{-3})	Hole Density (cm^{-3})	Hole Mobility (cm^{2}V^{-1}s^{-1})
HP-$Si_{90}Ge_{10}$-[B]$_3$	92:8	3.3	2.58 (96.2%)	4.88×10^{20}	1.35×10^{20}	29
HP-$Si_{80}Ge_{20}$-[B]$_3$	82:18	1.1	2.97 (98.8%)	2.91×10^{20}	1.55×10^{20}	28
SPS-$(Si)_{85}(Ge)_{15}$-[B]$_3$	85:15	3–10	2.65 (92.0%)	3.63×10^{20}	2.45×10^{20}	22

Table 6.1: Summary of the compositional and carrier properties of the similarly doped hot pressed samples compared to the SPS'd sample. ^{a}The mass-density column includes the density relative to the theoretical density for the nominal Si:Ge composition.[135] (Adapted with permission from Snedaker et al. [128]. Copyright 2013 American Chemical Society.)

The RSF for boron in silicon was corrected according to the Si:Ge ratio for the samples as determined by EDX and the estimated boron density's correlation

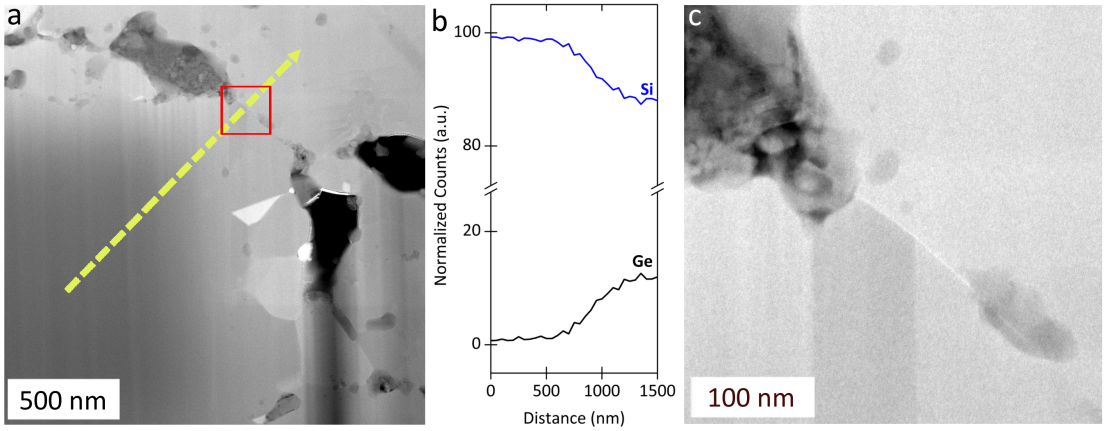

Figure 6.8: (a) HAADF-STEM image and EDX linescan direction across a grain in the 6.7b lamella, (b) EDX linescan for Si and Ge approaching the grain boundary, and (c) HAADF-STEM image of the boxed region shown in (a) shows Z-contrast due to germanium at the grain boundary.

to Seebeck coefficient and hole density are shown in Figure 6.10a. The SPS–$(Si)_{85}(Ge)_{15}$–$[B]_3$ sample's data agrees with previously reported carrier density–Seebeck coefficient values for boron doped $Si_{1-x}Ge_x$. The temperature dependent Seebeck coefficient indicates that the SPS–$(Si)_{85}(Ge)_{15}$–$[B]_3$ has an above-optimal boron density (see Fig. 6.10) and there is hysteresis upon cooling, which may be due to alloying that takes place at the higher temperatures and a change in the conductivity. The electrical conductivity of the SPS–$(Si)_{85}(Ge)_{15}$–$[B]_3$ is competitive with the ball milled nanocomposite reported by Joshi et al. [21]. The above-optimal carrier density in the SPS–$(Si)_{85}(Ge)_{15}$–$[B]_3$ pellet degrades the

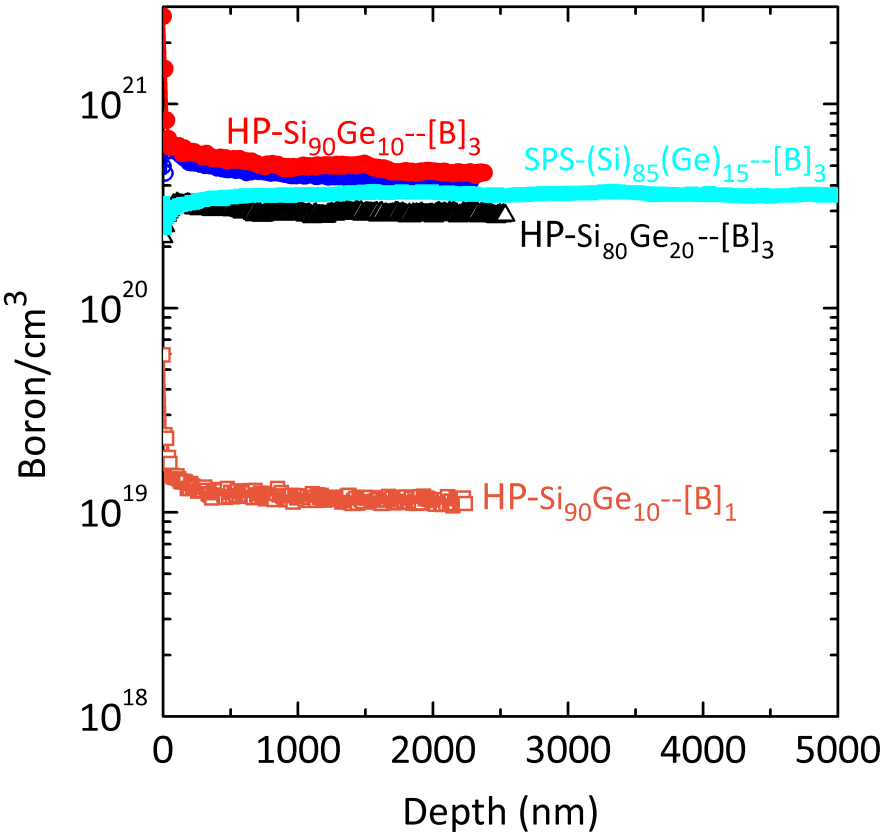

Figure 6.9: Dynamic secondary ion mass spectrometry depth profiles of boron in the $Si_{1-x}Ge_x$ pellets that were prepared with varying boron content and hot pressed compared to the SPS–$(Si)_{85}(Ge)_{15}$–$[B]_3$ pellet. Two HP–$Si_{90}Ge_{10}$–$[B]_3$ samples were measured in order to check doping reproducibility. (Adapted with permission from Snedaker et al. [128]. Copyright 2013 American Chemical Society.)

Seebeck coefficient, limiting the thermoelectric power factor to below the literature record.

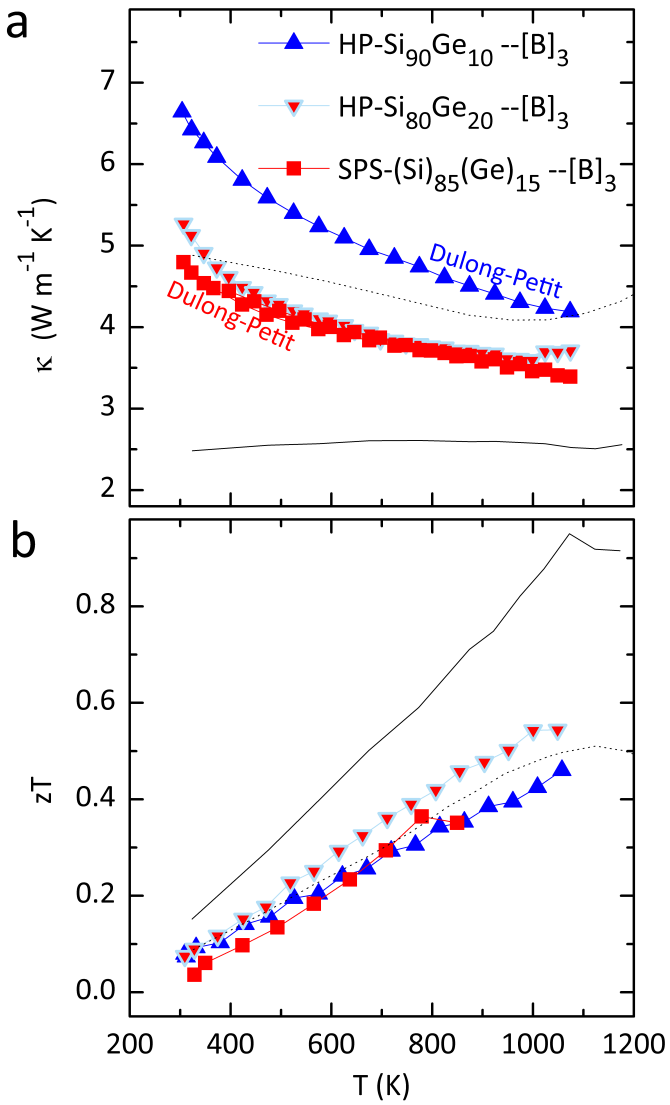

Figure 6.11: Temperature dependence of the (a) thermal conductivity and (b) thermoelectric figure of merit for $Si_{1-x}Ge_x$alloys of varying boron content prepared by magnesiothermic reduction of a silica-germania nanocomposite. The thermal conductivity is calculated from thermal diffusivity, Archimedean density, and the relevant heat capacity (i.e. the literature-reported, temperature-dependent heat capacity of $Si_{80}Ge_{20}$ or the Dulong-Petit value for $Si_{90}Ge_{10}$). The dotted trace represents the data for RTG–$Si_{80}Ge_{20}$ and the solid trace represents the data for BM–$Si_{80}Ge_{20}$.[21] (Adapted with permission from Snedaker et al. [128]. Copyright 2013 American Chemical Society.)

Temperature dependent thermal diffusivity of the SPS–$(Si)_{85}(Ge)_{15}$–$[B]_3$ pellet was measured and combined with the geometric density, and the Dulong-Petit heat capacity for $Si_{95}Ge_5$ to yield the thermal conductivity shown in Figure 6.11a. The thermal conductivity that we estimate is approximately the same as for HP–$Si_{80}Ge_{20}$–$[B]_3$ and with less germanium. "It is known that thermal conductivity of the inhomogeneous material is less than that of the volume averaged thermal conductivity due to the inhomogeneous temperature gradient"[149–151] so perhaps that and more nanostructuring explains why the sample with less germanium has comparable thermal conductivity to the homogeneous $Si_{80}Ge_{20}$ alloy. At high temperatures, the thermal conductivity of SPS–$(Si)_{85}(Ge)_{15}$–$[B]_3$ does not show signs of a bipolar contribution which is likely due to the higher hole density in this sample. The thermal conductivity of SPS–$(Si)_{85}(Ge)_{15}$–$[B]_3$ is greater than than the thermal conductivity of the ball milled $Si_{80}Ge_{20}$ nanocomposite reported by Joshi et al.. The thermoelectric figure of merit of SPS–$(Si)_{85}(Ge)_{15}$–$[B]_3$ is shown in Figure 6.11b– it is less than that of the homogeneous hot pressed $Si_{80}Ge_{20}$–$[B]_3$ due to an unoptimal Seebeck coefficient.

6.2.4 The optimal pressing profile for a silicon germanium nanocomposite powder

Since germanium and silicon have a wide gap in their melting temperatures, the SPS profile must not be as extreme as what was tried here. It may be possible to get homogeneous alloying if the SPS–$(Si)_{85}(Ge)_{15}$–$[B]_3$ pressing takes place at ~50% the melting point of germanium (i.e. ~490 °C).

6.3 Microwave heating to increase the extent of alloying

Conventional microwave ovens have been used to rapidly prepare thermoelectric half-Heusler compounds.[152] Microwave preparation of phosphors for lighting applications and noble metal oxides for catalysis have also been demonstrated.[153–155]

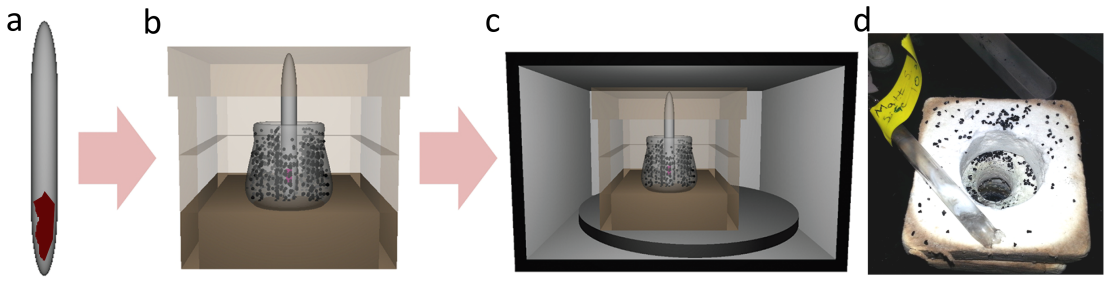

Figure 6.12: Schematic of microwave heating procedure: (a) the $(Si)_{1-x}(Ge)_x$ is placed in an evacuated quartz tube and sealed with an oxygen torch, (b) the tube is placed in a crucible filled with activated carbon, (c) the crucible and fire brick are placed in a conventional microwave oven and set for the desired power level and time. Some microwaving conditions led to (d) a violent explosion of the tube due to outgassing (Fig. 6.12a–c reprinted with permission from Birkel et al. [152]. Copyright 2012 American Chemical Society.)

A typical procedure is to put the powder precursors into a quartz tube, evacuate the tube, and seal it with an oxygen torch as shown in Figure 6.12a. The tube may be placed in a crucible that is filled with activated carbon, the crucible & tube are placed in a protective fire brick, and the microwave power level and time are used as reaction controls. Birkel and Lettiere demonstrated that microwave heating of silicon powder and germanium powder would lead to some alloying between the elements, as shown in Figure 6.13a after 7.5 minutes and then SPS was used to consolidate the powder-alloy mixture. However, a close inspection of the Si(111) reflection of the microwaved and SPS'd product show that that reflection is asymmetric and the alloy is not homogeneous. Regardless, microwave heating

is a potentially useful method for us to alloy our $(Si)_{1-x}(Ge)_x$ powder before the spark plasma sintering process.

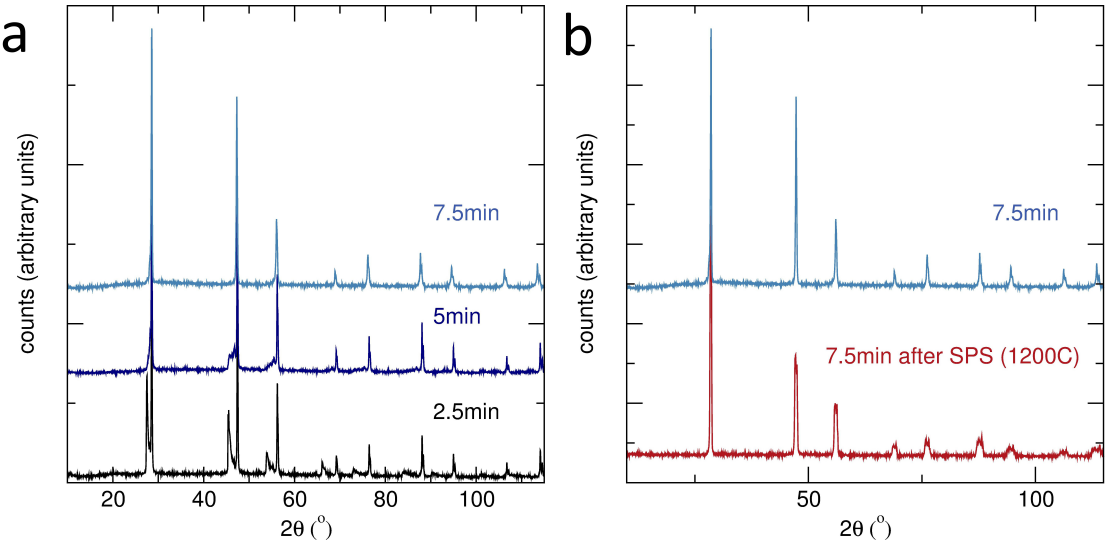

Figure 6.13: The effect of microwave heating and subsequent spark plasma sintering on silicon and germanium powders: (a) powder XRD patterns for a mixture of silicon powder and germanium powder that is microwaved for an increasing amount of time, resulting in some alloying and (b) the XRD pattern after the microwaved, heterogeneous $Si_{1-x}Ge_x$ is spark plasma sintered. (This is unpublished work reproduced with the permission of Birkel and Lettiere [156].)

It is difficult to know the temperature distribution in the microwave oven and at the sample. A pyrometer was used to measure the temperature at the activated carbon under different microwave oven conditions, as is shown in 6.14. The temperature at the activated carbon can be prescribed and it may exceed the melting point of germanium. Some microwave heating conditions were found to cause

outgassing and explosion of the tubes, as shown in Figure 6.12d and sometimes the sides of the tube would get coated in what we believe was germanium.

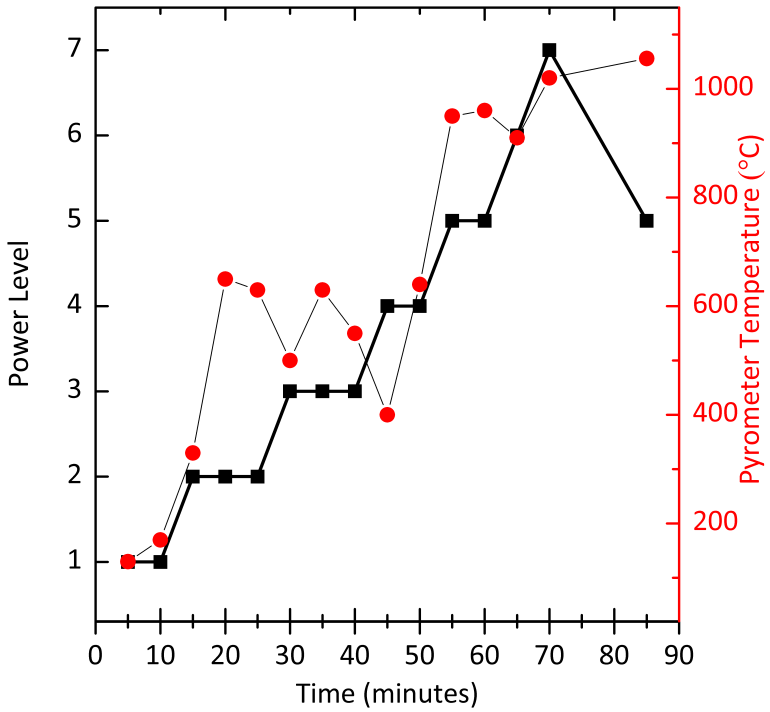

Figure 6.14: Pyrometer temperature measurements of the microwave activator carbon at different power levels.

The $(Si)_{80}(Ge)_{20}$ powder was microwaved sequentially under different conditions and the powder was collected for XRD. Figure 6.15 shows that successive microwave heatings cause the intensity of the Ge(111) reflection to decrease and the Si(111) peak to broaden and shift towards Ge(111), which indicates alloying. There was not much control with this process and it seemed that we would not be able to obtain a lot of homogeneously alloyed $Si_{1-x}Ge_x$ because there was the

risk of the tubes exploding. A nitric acid treatment was used to selectively etch the germanium phase and/or a magnesium fluoride phase, which shows that there is some crystalline $Si_{1-x}Ge_x$ phase present.

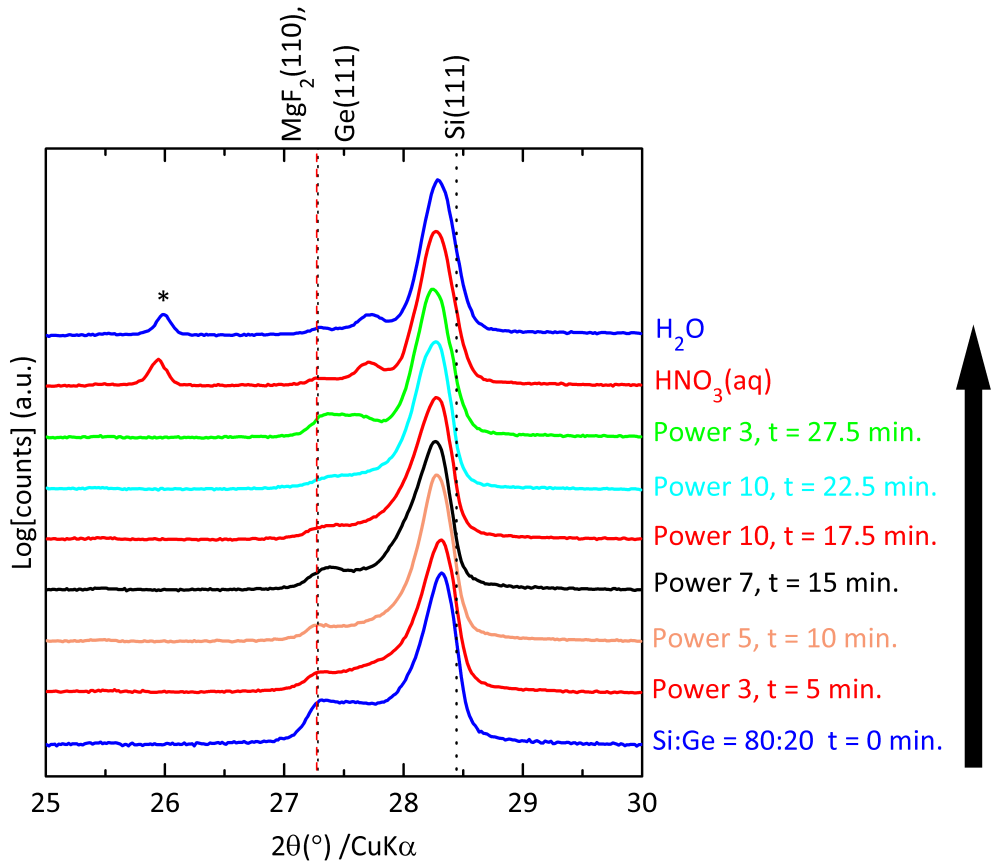

Figure 6.15: The effect of progressive microwave heating on the homogeneity of the $(Si)_{80}(Ge)_{20}$ powder. A nitric acid treatment was used to preferentially etch the magnesium fluoride impurity phase; however, nitric acid will also attack nanostructured Ge.

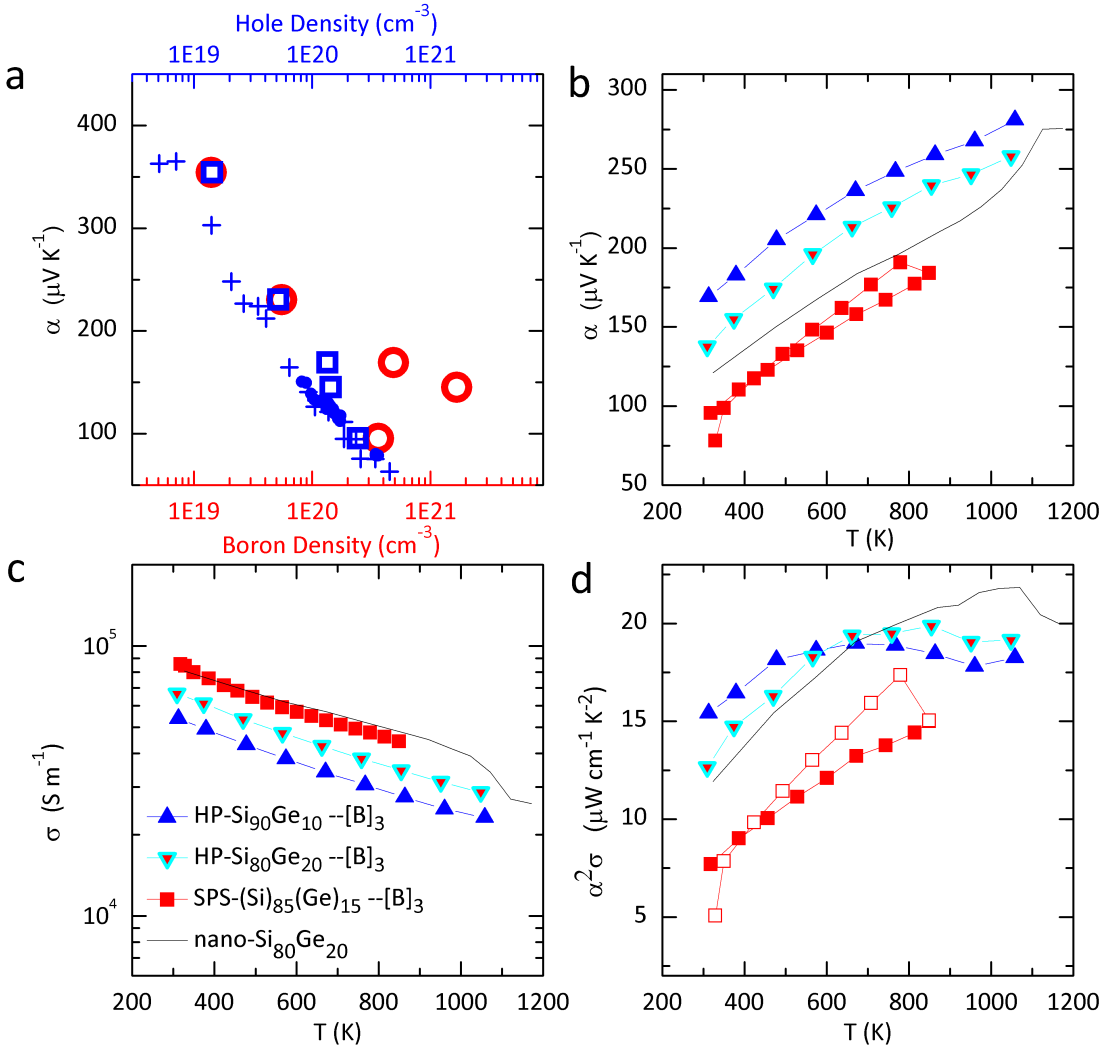

Figure 6.10: (a) Dependence of room-temperature Seebeck coefficient on the boron density (red ring) and the hole density (blue box) for the HP–$Si_{90}Ge_{10}$–$[B]_i$ doping series & HP–$Si_{80}Ge_{20}$–$[B]_3$ & SPS–$(Si)_{85}(Ge)_{15}$–$[B]_3$, including the data reported for p-type $Si_{70}Ge_{30}$ (blue crosses),[137] and p-type $Si_{80}Ge_{20}$ (blue circles).[138] Temperature dependence of the (b) Seebeck coefficient, (c) electrical conductivity, and (d) power factor for bulk-nanostructured $Si_{1-x}Ge_x$ alloys consolidated via hot pressing and SPS. The power factor of the SPS'd sample is shown with the heating values (closed) and cooling values (open). The solid trace represents the data from BM-$Si_{80}Ge_{20}$.[21] (Adapted with permission from Snedaker et al. [128]. Copyright 2013 American Chemical Society.)

Chapter 7

The effect of reduction medium on alloying and grain growth

In Chapters 4, 5, 6, and 7, the reductions of the "Stöber" $(SiO_2)_{1-x}(GeO_2)_x$ were performed with intimate mixing & cold-pressed contact of the magnesium powder and oxide powder. The intimate mixing & cold-pressed contact and the long reaction time used, result in large $(Si)_{1-x}(Ge)_x$ crystallites.

To reduce the lattice thermal conductivity of our $Si_{1-x}Ge_x$ pellets, we must minimize the crystallite size in the $(Si)_{1-x}(Ge)_x$ that we obtain after the magnesiothermic reduction. This can be realized by using a lower furnace temperature (i.e. controlling the vapor pressure of magnesium), shorter reaction time (i.e. controlling grain growth and diffusion time), and using a reaction medium that controls heat dissipation. The difficulty arises that the heat that goes to grain growth and the heat that goes towards forming the alloy are related.

7.1 Reduction of oxides in molten salts

"Pinpoint and bulk electrochemical reduction of insulating silicon dioxide to silicon" was achieved with a LiCl–KCl–$CaCl_2$ molten salt at 500 °C.[157] $CaCl_2$ was also used for reduction of SiO_2 at 1123 K.[158] The use of the LiCl–KCl and NaCl–$MgCl_2$ eutectics for magnesiothermic reduction media was pioneered by Liu et al. [159] (the phase diagrams are shown in Fig. 7.1), who argue that these salts produce solvated electrons that allow the reduction of the oxide to occur. Use of the pure $MgCl_2$ or NaCl will also lead to the formation of Si particles but with a slight difference in particle morphology.[160].

7.1.1 The LiCl–KCl eutectic

For this molten salt system, a molar ratio of $Mg/(SiO_2)_{1-x}(GeO_2)_x = 2.2$ and a weight ratio of $((SiO_2)_{1-x}(GeO_2)_x + Mg)/(salts + (SiO_2)_{1-x}(GeO_2)_x + Mg) = 10\%$ were used and the reductions were performed both in a argon-flow tube furnace and in an alumina crucible that was placed in a nitrogen purged box furnace. Figure 7.2b shows an problem encountered in the tube furnace setup, where the molten salt flows onto the quartz tube and upon cooling, cracks the tube. When the reduction is performed in the box furnace under nitrogen flow, the molten salt flows up the wall of the crucible as seen in Figure 7.2c – this may

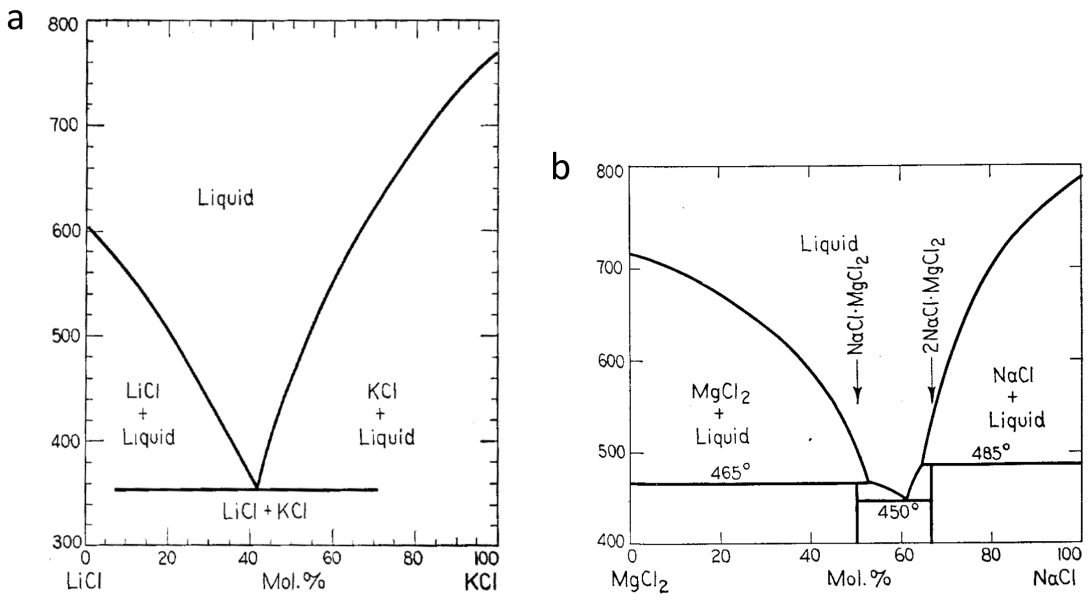

Figure 7.1: Phase diagrams for (a) the LiCl–KCl system as reported by Elchardus and Laffitte and (b) the NaCl–$MgCl_2$ system as reported by Klemm and Weiss.[102, 161, 162] (Reprinted with the permission of The American Ceramic Society, `www.ceramics.org`.)

be avoided using a lower nitrogen flowrate; however, at this flowrate, we observed signifcant oxygen impurity and the crystallite size was much lower than in the tube furnace synthesis. Another complication was the removal of LiCl; although, it is highly soluble in water, there was still residual LiCl with the product after being cleaned and filtered with >1 Liter of water.

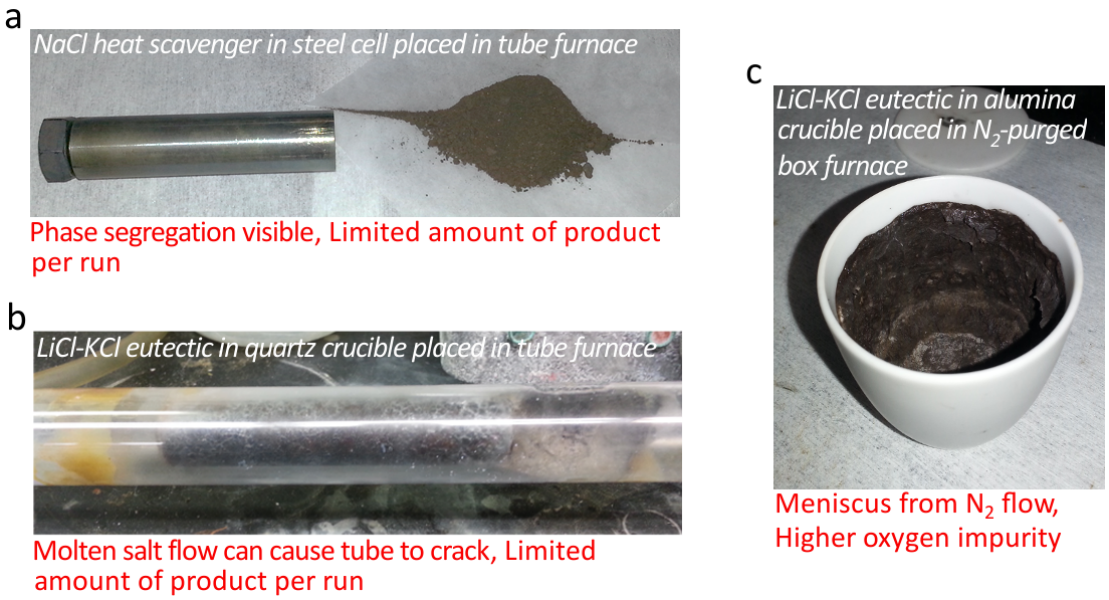

Figure 7.2: Challenges faced with magnesiothermic reductions in the different reduction media and reactors: (a) magnesiothermic reduction in the presence of 1/10 wt.% ratio of oxide to NaCl salt leads to a $(Si)_{1-x}(Ge)_x$ that has phase segregation visible by eye, (b) magnesiothermic reduction in the LiCl–KCl eutectic results in flow of the eutectic, that upon cooling, contracts and cracks quartz, and (c) use of the eutectic in a alumina crucible in a box furnace can yield more product but is more prone to oxidation.

7.1.2 Molten NaCl

Luo et al. reported on the use of NaCl as a heat scavenger during the magnesiothermic reduction of $(SiO_2)_{1-x}(GeO_2)_x$. When we applied that strategy with a 1/10 wt.% ratio of oxide to NaCl salt, we obtained a brown powder (see Fig. 7.2a) with dark flecks visible by eye that indicate phase segregation of germanium. The

removal of the NaCl with water and hydrochloric acid cleans is shown in Figure 7.3 and one advantage of this process is that the NaCl may be recycled.

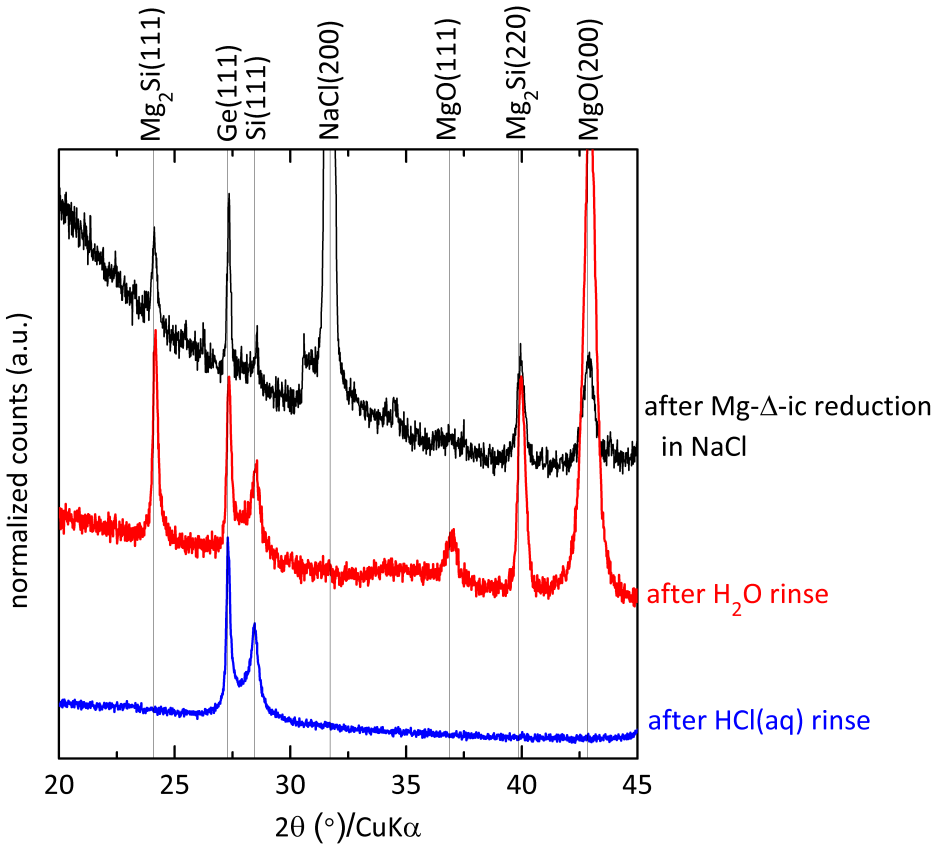

Figure 7.3: Powder XRD patterns of the $(Si)_{80}(Ge)_{20}$ prepared in the molten sodium chloride and after a water and hydrochloric acid clean.

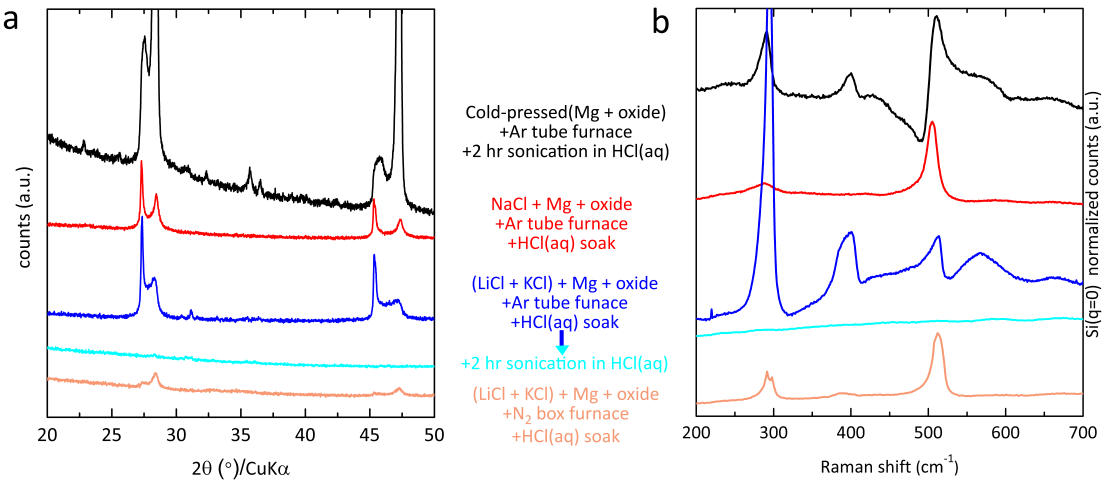

Figure 7.4: (a) Powder XRD patterns and (b) Raman spectra of $(Si)_{80}(Ge)_{20}$ prepared under different magnesiothermic reduction conditions.

7.1.3 Effect of reduction medium on crystallite size and alloying.

The powder XRD patterns and Raman spectra shown in Figure 7.4 allow us to compare the crystal properties and bonding properties in the powders obtained from magnesiothermic reduction in different media. Reduction of the cold-pressed oxide & magnesium results in the largest crystallite sizes and some alloying between the Si–Ge, as seen in the Raman band at ~400 cm^{-1}. Reduction of the oxide mixed with NaCl yields much smaller crystallites, as indicated by the larger breadth of the (111) reflections and it appears that the Si and Ge phases are distinctly segregated, which we confirm by the absence of the Si–Ge band in the

Raman spectrum. This is an important distinction from the results obtained by Luo et al., who claimed retention of phase segregation but present a Raman spectrum that shows the presence of Si–Ge alloy. If NaCl is an efficient heat scavenger, then there should be little to no alloying, as we show. We attribute their result to improper mixing of the precursor oxide, salt, and magnesium.

The reduction of the $(SiO_2)_{80}(GeO_2)_{20}$ in the LiCl–KCl in a tube furnace yields crystallite sizes similar to those in the case of molten NaCl and the breadth of the peaks indicates some alloying of Si–Ge, as confirmed by Raman spectroscopy. The fragility of these nanostructures is evident by the loss of crystallinity and presumed oxidation of the material upon the sonication and acid cleaning procedure that we had employed for the powder purification procedures discussed earlier in the thesis. Although the reactant and salt ratios were the same, reduction in LiCl–KCl that was performed in the nitrogen-purged glovebox leads to a smaller crystallite size, more oxygen impurity, and less Si–Ge alloying.

We attribute the difficulty in controlling crystallite size and the extent of alloying to the difference in the latent heats of crystallization of Ge, $Si_{1-x}Ge_x$, and Si and the heats for alloy formation. Figure 7.5 shows the crystallization transition temperatures and latent heat of crystallization for the $Si_{1-x}Ge_x$ system. It takes much less heat to initiate crystallization of Ge and once initiated, crystallization can be "explosive" according to Takamori et al. [164], Fan et al. [165], and Aydinli

et al. [166]. However, it may be possible to engineer the $(Si)_{1-x}(Ge)_x$structure so that the crystallite sizes are such that a nanocrystalline, homogeneous alloy may be prepared in the appropriate reduction medium.

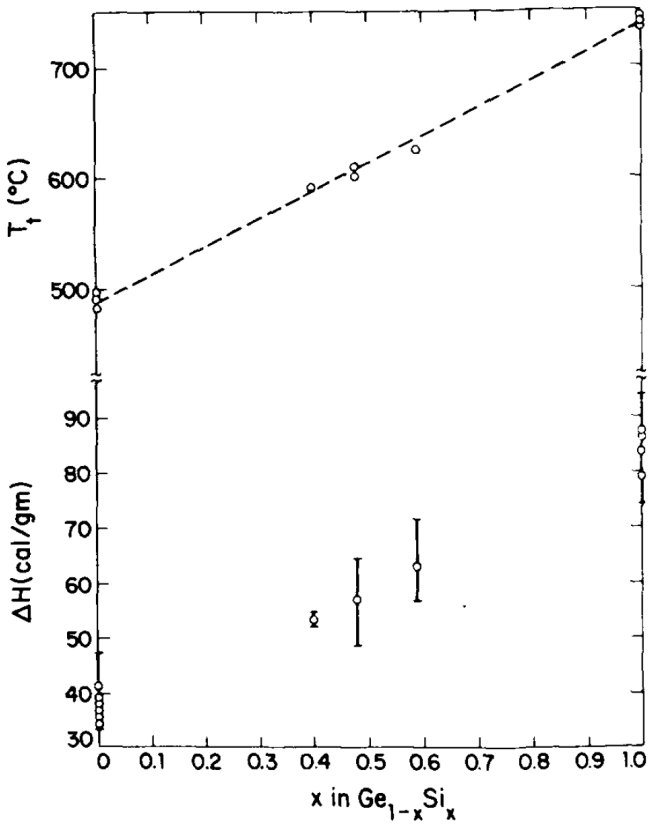

Figure 7.5: Crystallization transition temperature & latent heat of crystallization for the $Si_{1-x}Ge_x$ system. (Reprinted with permission from Fan and Anderson [167]. Copyright 1981, AIP Publishing LLC.)

7.2 Methods for controlling the extent of alloying and the Si/Ge interface

7.2.1 Laser annealing

Laser annealing of amorphous silicon to induce crystallization is used industrially and has been studied by many researchers.[168–171] We observed crystallization of an amorphous silicon component in our LiCl–KCl mediated $(Si)_{80}(Ge)_{20}$ powder after a short time of laser irradiation, as shown in Figure 7.6. Perhaps this type of irradiation treatment may be used to engineer the interface between the Si/Ge interface.

7.2.2 Magnesiothermic reduction at temperatures lower than magnesium's melting point

Shi showed that the temperature of the furnace during the magnesiothermic reduction has a significant impact on the crystallite size, as shown in Figure 7.7. Higher furnace temperatures lead to larger crystallites. Perhaps lower furnace temperatures could yield smaller crystallite sizes that will make it easier to achieve Si–Ge alloying.

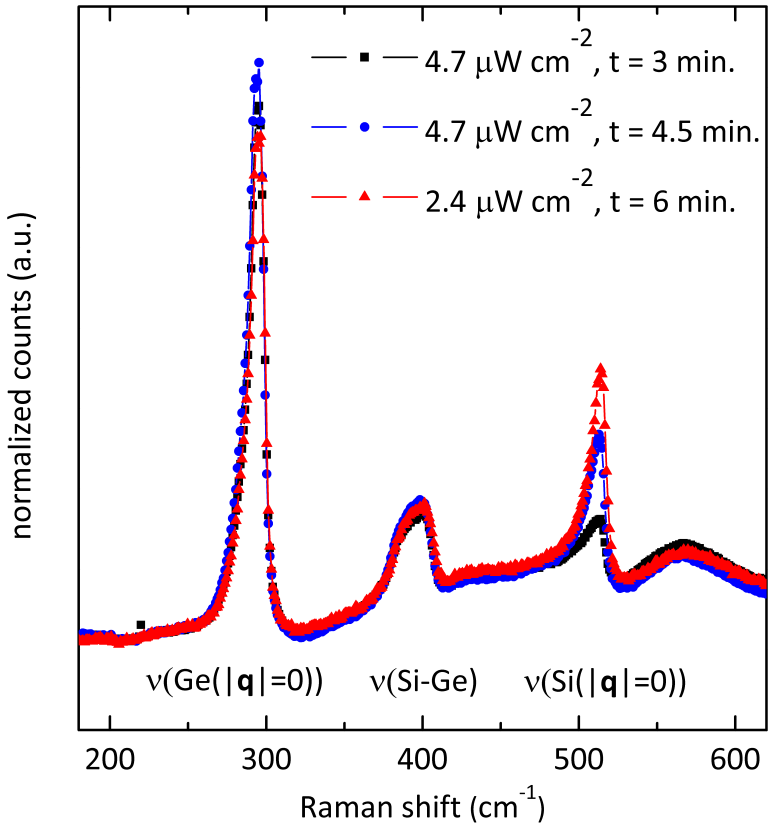

Figure 7.6: Laser annealing of $(Si)_{80}(Ge)_{20}$ prepared in the eutectic LiCl-KCl shows rapid crystallization of amorphous silicon.

7.2.3 Magnesiothermic reduction in the presence of hydrogen gas

The germania phase may be preferentially reduced with hydrogen gas at low temperatures according to equation 8.8.

$$GeO_2(s) + 2H_2(g) \xrightarrow{400\ ^\circ C} Ge(s) + 2H_2O(g)\ . \tag{7.1}$$

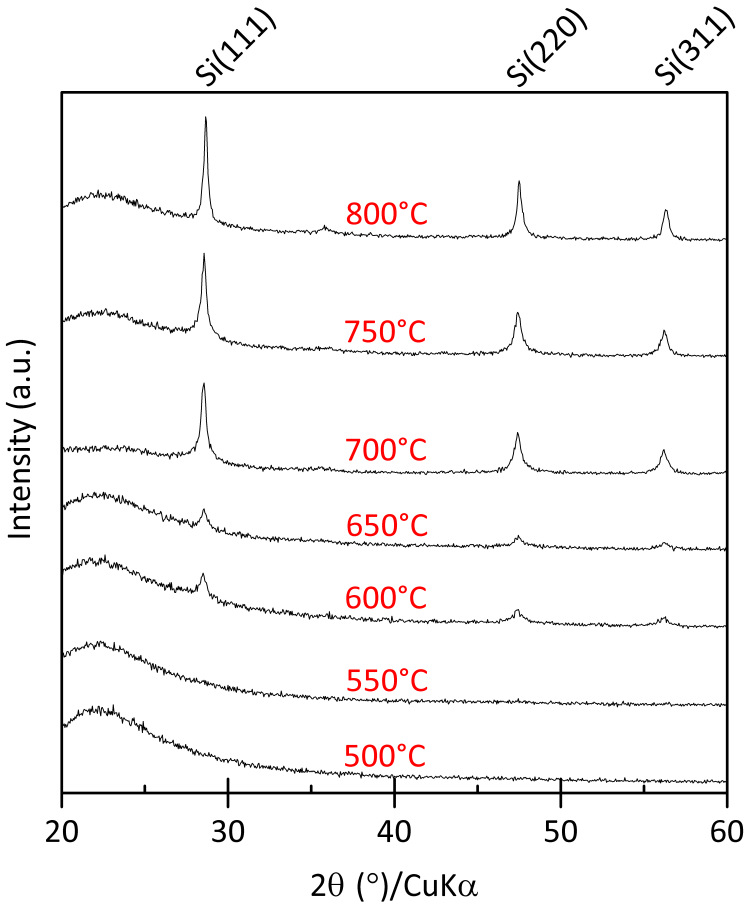

Figure 7.7: Effect of furnace temperature on the silicon crystallite size produced during magnesiothermic reduction (unpublished work by and with permission of Shi [172]).

When we performed the magnesiothermic reduction of $(SiO_2)_{80}(GeO_2)_{20}$ with hydrogen flow present, we observed a change in the Ge(111) reflection's peakshape and breadth as shown in Figure 7.8. Perhaps hydrogen reduction of the germania phase will allow Si/Ge heterostructures to be prepared.

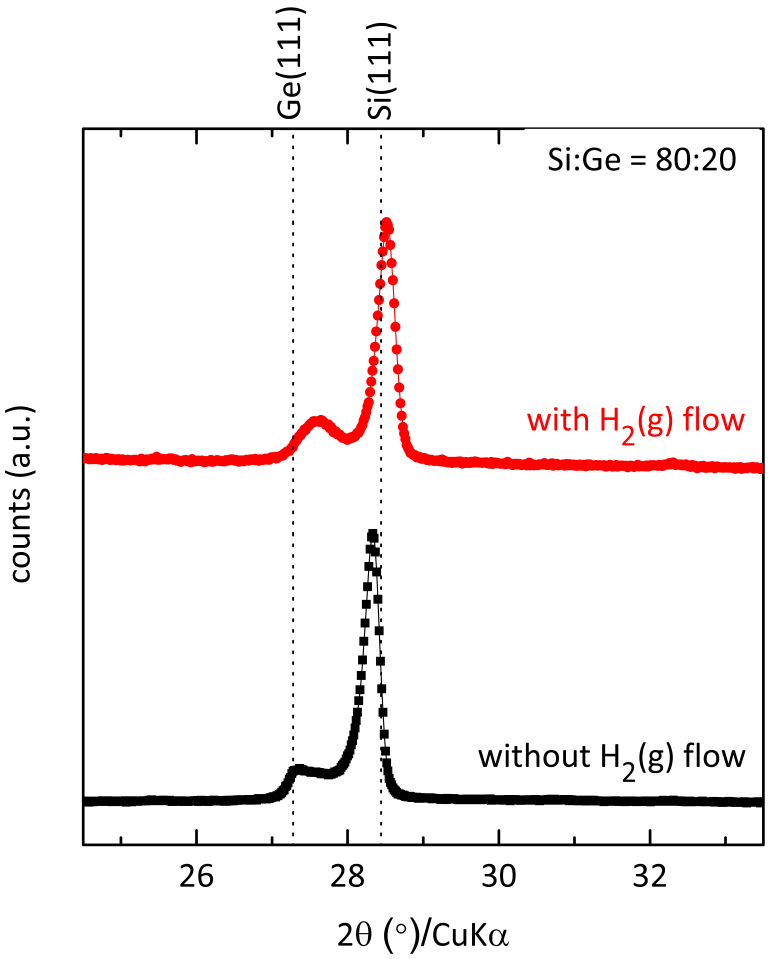

Figure 7.8: XRD patterns of the powder after the magnesiothermic reduction of the $(SiO_2)_{80}(GeO_2)_{20}$ with and without the presence of hydrogen gas.

Chapter 8

Heterostructured PEDOT:PSS/Germanium thermoelectrics

8.1 Introduction

The thermoelectrics research community is plagued by two things: (1) most improvements in zT have been accomplished via reduction of lattice thermal conductivity and (2) "demonstrations" of power factor (i.e. $\alpha^2\sigma$) enhancement, thus far, have been in miscible, inhomogeneous composites, where the interpretation of Hall effect results is not straightforward and the thermal stability of the composite is questionable. Enhancement of thermoelectric power factor in heterostructured SiGe nanocomposites via modulation doping was demonstrated by Zebarjadi et al. [34] and Yu et al. [35]. And Heremans et al. made a convincing argument for enhanced thermoelectric power factor in PbTe due to distortion

of the electronic density of states. Carrier filtering, where the energy derivative of the electrical conductivity is increased due to a mechanism that preferentially scatters low energy carriers, has been proposed as a strategy to enhance the thermoelectric power factor. Zide et al. demonstrated enhanced Seebeck coefficients in $In_{0.53}Ga_{0.47}As/In_{0.53}Ga_{0.28}Al_{0.19}As$ superlattices, which they attribute to energy filtering, where the low energy carriers are blocked and the higher energy carriers are transported, producing a lower electrical conductivity but an increase in the derivative of the conductivity with respect to energy.[39] The concept of energy filtering has also been used to explain the thermoelectric properties of highly-doped nanograined semiconductors.[40] However, claims of carrier energy filtering are difficult to believe and probably can't be directly proven since the energy derivative of the electrical conductivity has not been measured.

A degenerately doped (i.e. metallic) semiconductor's Seebeck coefficient may be described by the Mott equation (see equation 8.1), which relates the Seebeck coefficient to the derivative of the energy dependence of the electrical conductivity, evaluated at the Fermi level. Using the definition of electrical conductivity, $\sigma(E) = q\ n(E)\ \mu(E)$, where q, n, and μ are the majority carrier's charge, the carrier density, and the charge mobility, respectively, the Seebeck coefficient's dependence

on n, μ, and the change (see equation 8.2).

$$\alpha \propto \left\{ \frac{d[ln(\sigma(E)]}{dE} \right\}_{E=E_F} \tag{8.1}$$

$$\propto \left\{ \frac{1}{n}\frac{d\, n(E)}{dE} + \frac{1}{\mu}\frac{d\, \mu(E)}{dE} \right\}_{E=E_F} \tag{8.2}$$

It is not straightforward to attribute the results from a Hall effect measurement for an polycrystalline, inhomogeneous material to a change in the Hall mobility or a change in the carrier density or a combination of both.[173] Indeed, the Hall coefficient may even indicate the wrong carrier type in some materials.[174]

The Hall voltage that is measured for a single carrier type semiconductor is related to the carrier density (and Hall coefficient) and measurement parameters by equation 8.3. However, the Hall mobility and carrier density are also affected by the Hall scattering factor r_{Hall}, which is sensitive to the material's homogeneity and is not necessarily 1.0. Comparison of Hall results for two materials with different homogeneities may lead to improper conclusions if the Hall scattering factor isn't considered.

$$V_{Hall} = -\frac{I\ \|\mathbf{B}\|}{n\ t\ e} \tag{8.3}$$

$$R_{Hall} = -\frac{1}{n\ e} \tag{8.4}$$

$$n_{Hall} = r_{Hall}\ /(R_{Hall}\ e) \tag{8.5}$$

$$\mu_{Hall} = R_{Hall}\ \sigma = r_{Hall}\ \mu_{drift} \tag{8.6}$$

8.2 Claims of carrier filtering in hydrazine-solution-processed chacogenide thermoelectrics are problematic

Ko et al. reported an enhanced Seebeck coefficient in Pt–Sb_2Te_3 nanocomposites due to carrier energy filtering.[175] The summary of their Hall results is shown in Figure 8.1, where the mobility and carrier density could be incorrect since they didn't consider the Hall scattering factor. Also consider that the platinum may be soluble in the Sb_2Te_3 matrix so that the enhancement comes from the better thermoelectric properties of the Pt–Sb_2Te_3. A similar study was reported for Ag-Sb_2Te_3 and Ag/oxide/Sb_2Te_3 films with enhanced thermoelectric power factor that is attributed to carrier filtering.[176, 177] Zhang et al. report the process shown in Figure 8.2a to prepare heterostructure where silver nanoparticles are protected with a barrier deposited by atomic layer deposition (ALD) and the interface of those metal particles to the Sb_2Te_3 produces a Schottky barrier that will filter the low energy holes. However, ALD films are not defect free [178] and as shown in the secondary ion mass spectrum depth profile shown in Figure 8.2b, silver that is supposed to be contained has diffused 40% into the film's thickness. Since silver is a dopant in Sb_2Te_3 it is difficult to believe that carrier filtering is

Table 1. Summary of van der Pauw resistivity, Hall effect, and thermopower measurements on Sb_2Te_3 matrix and $Pt-Sb_2Te_3$ nanocomposite at room temperature[a]

	nanocomposite	Sb_2Te_3
resistivity [$\Omega \cdot$cm]	3.69 ($\pm$0.73) $\times$ 10^{-2}	1.37 ($\pm$0.04) $\times$ 10^{-2}
type of carriers	holes	holes
carrier mobility [$cm^2/(V\ s)$]	11.4 ($\pm$3.0)	28 ($\pm$5.9)
carrier concentration [cm^{-3}]	2.46 ($\pm$0.89) $\times$ 10^{19}	1.67 ($\pm$0.36) $\times$ 10^{19}
thermopower [μV/K]	151.6 $\pm$ 14.8	115.6 $\pm$ 8.3
power factor at 300 K [uW/cmK^2]	1.02 $\pm$ 0.36	0.96 $\pm$ 0.14

Figure 8.1: Electronic properties of a Pt–Sb_2Te_3 nanocomposite with Seebeck coefficient exceeding that of Sb_2Te_3, which the authors attribute to the carrier filtering effect. (Reprinted with permission from Ko et al. [175]. Copyright 2011 American Chemical Society.)

being demonstrated as opposed to modulation doping from the Ag-doped region at the bottom of the film to the top of the film where the electrical contacts for the Hall measurement are placed. Furthermore, the roughness of these films introduces error and potential deviation of the Hall scattering factor.

8.3 The ideal system for the demonstration of carrier filtering

We aim to develop a composite system where component A and component B are immiscible. If A and B mix, then we cannot attribute an observable to

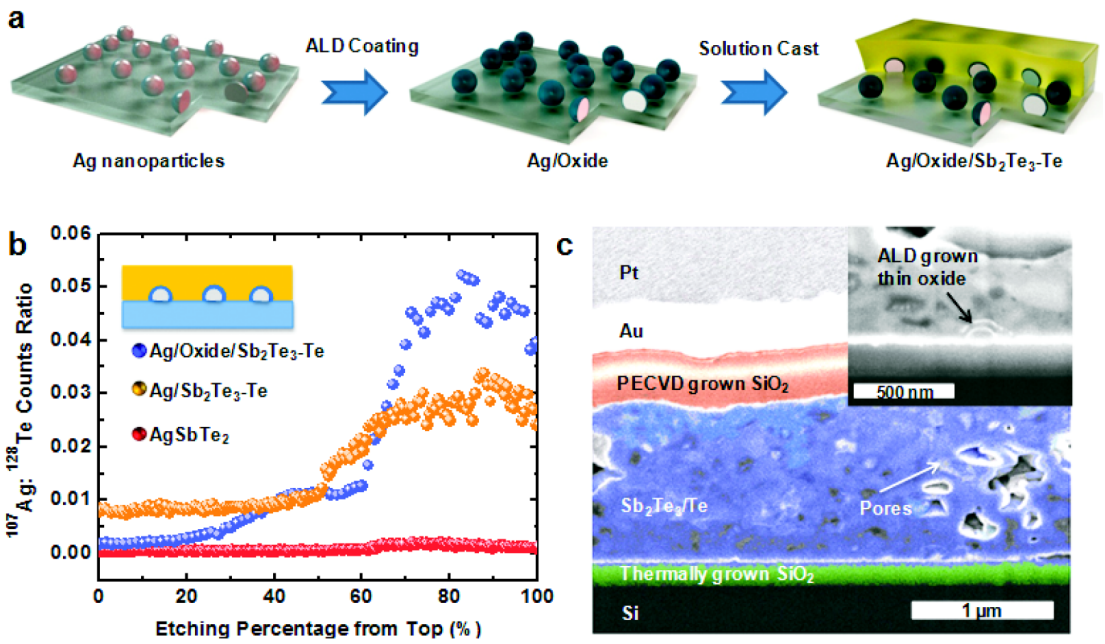

Figure 8.2: Silver distribution in a Ag/oxide/Sb_2Te_3 nanocomposite with Seebeck coefficient exceeding that of Sb_2Te_3, which Zhang et al. attribute to the carrier filtering effect. (a) schematic of the material/device, (b) SIMS depth profile showing silver is not contained by ALD oxide barrier, and (c) cross-sectional SEM image of the material/device (Reprinted with permission from Zhang et al. [177]. Copyright 2014 Zhang et al.. doi:10.1002/adma.201304419)

an interfacial property. The composite should have isotype junctions, where the majority carrier in each phase is of the same type to avoid p-n junctions and trapping. Composite film must be smooth. We would like the composite to have amorphous limited thermal conductivity so that the thermoelectric figure of merit will be higher

8.3.1 Enhanced thermoelectric power factor in organic–inorganic heterostructures is possibly due to the carrier filtering/modulation doping effects

The polymer system poly(3,4-ethylenedioxythiophene) polystyrene sulfonate is also known as PEDOT:PSS and is shown in Figure 8.3. Its thermoelectric properties have been investigated and the mobility has been shown to increase upon addition of co-solvents.[179] Use of the solvents to engineer the doping of the polymer system has resulted in $zT = 0.42$ at room temperature.

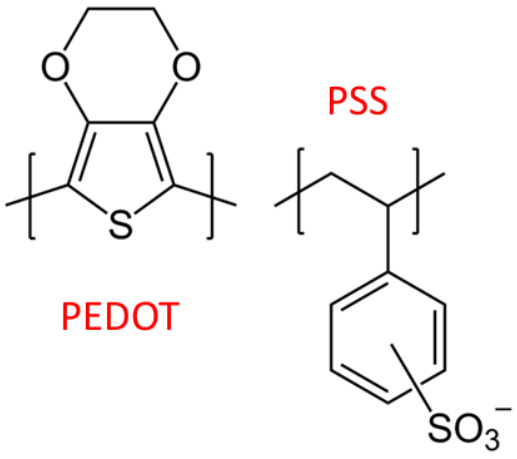

Figure 8.3: Poly(3,4-ethylenedioxythiophene) Polystyrene sulfonate aka PEDOT:PSS.

Coates et al. and Yee et al. prepared a nanocomposite of the PEDOT:PSS with tellurium nanowires and the composite exhibited a huge enhancement in the thermoelectric power factor, as shown in Figure 8.4.[181] It is unclear if enhance-

ment is due to a carrier filtering effect or ordering of the polymer at the interface. However, this is a model system because there will not be any alloying between the organic and the inorganic phases.

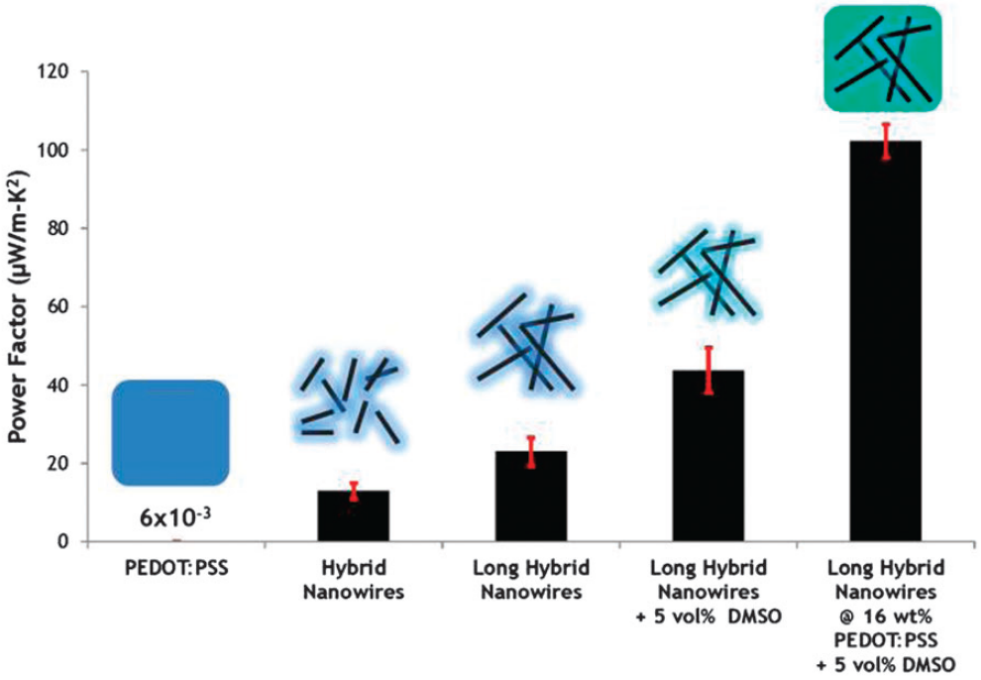

Figure 8.4: Yee et al. demonstrated enhanced thermoelectric power factor in an organic-inorganic hybrid thermoelectric. (Reproduced from Yee et al. [181] with permission of the PCCP Owner Societies. doi:10.1039/C3CP44558E)

A PEDOT:PSS/Germanium heterostructure that may exhibit a superior thermoelectric power factor

Germanium would be preferable to tellurium since it is more earth abundant, less toxic, exhibits a higher hole mobility, the doping control to tune the Fermi energy is more easily accomplished, and processing of germanium is more devel-

oped. In fact, there was a recent study on enhanced power factor in PEDOT:PSS mixed with germanium powder.[182] However, we have developed a method that will give us more control over the interface, structure, and band alignment in the heterostructured composite.

The intrinsic Fermi level (μ_i) of germanium may be calculated from equation 8.7, where E_v is the valence band edge energy, E_g is the bandgap, k_B is the Boltzmann constant, T is the absolute temperature, m_v is the effective mass at the valence band, and m_c is the effective mass at the conduction band. Using this with the electron affinity and work functions available in the literature for PEDOT:PSS and Ge, we can sketch the band alignment and band bending in PEDOT:PSS/i-Ge/PEDOT:PSS heterostructures, as shown in 8.5a & b.

$$\mu_i = E_v + \frac{1}{2}E_g + \frac{3}{4}k_B T \ln\left(\frac{m_v}{m_c}\right) \tag{8.7}$$

The utility of the PEDOT:PSS/i-Ge/PEDOT:PSS heterostructure is that a hole gas will form in the germanium phase and it will be highly mobile, giving rise to a modulation doping effect and the presence of the Schottky barrier will make it so that only the high energy holes can tunnel to the germanium, where they will be rapidly transported. The consequence is that you have a structure with modulation doping and carrier filtering.

We could dope the germanium phase with acceptor impurities to shift the Fermi level towards Ge's valence band to yield the alignment and band bending

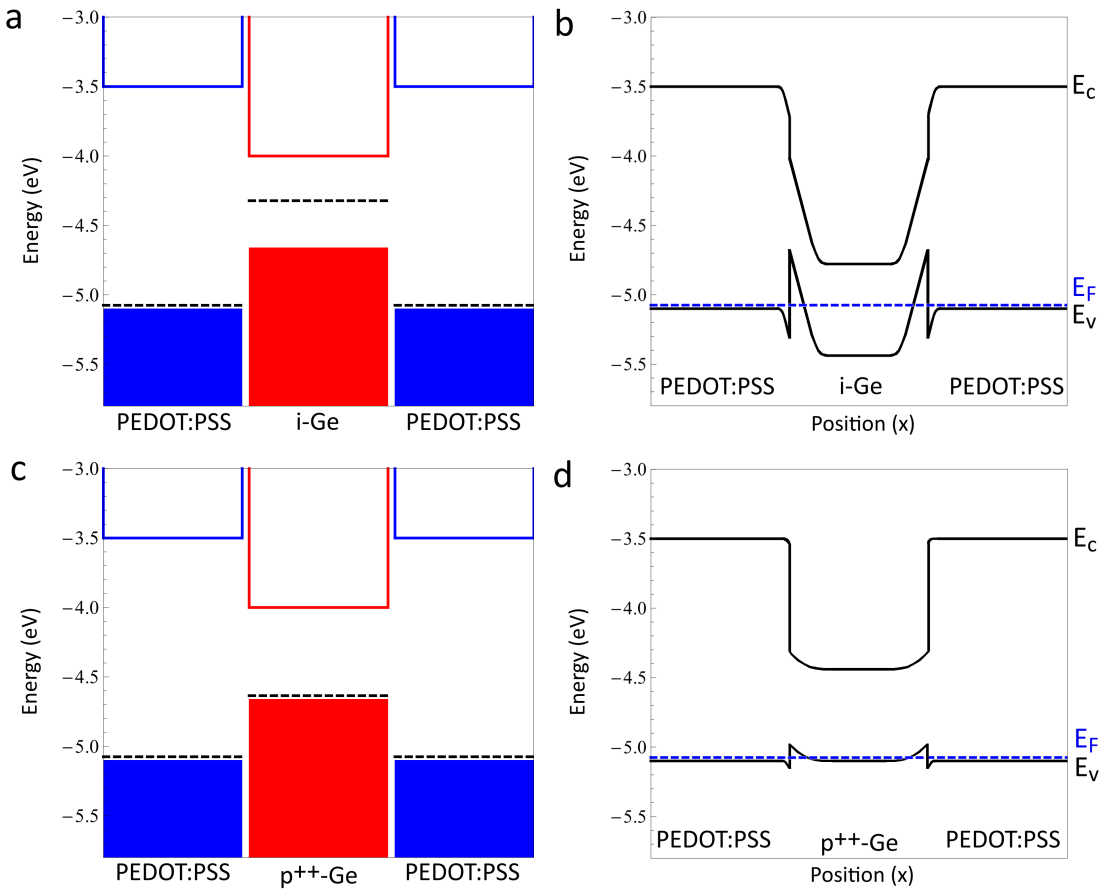

Figure 8.5: (a) Band alignment and (b) band bending in a PEDOT:PSS/i-Ge heterostructure. (c) Band alignment and (d) band bending in a PEDOT:PSS/p^{++}-Ge heterostructure.

sketched in Figure 8.5c & d. The utility of the PEDOT:PSS/p^{++}-Ge/PEDOT:PSS heterostructure is that the Schottky barrier may be tuned so that the energy filter can be variable to test the limit and connection between modulation doping and carrier filtering.

8.3.2 Preliminary data: Thermoelectric properties and Raman measurements

A silica germania nanocomposite was prepared by a sol-gel synthesis. The structure of the material is shown in Figure 8.6, where the GeO_2 dots are embedded within the silica matrix. The GeO_2 may be selectively reduced to size-controlled germanium nanocrystals according to equation 8.8.

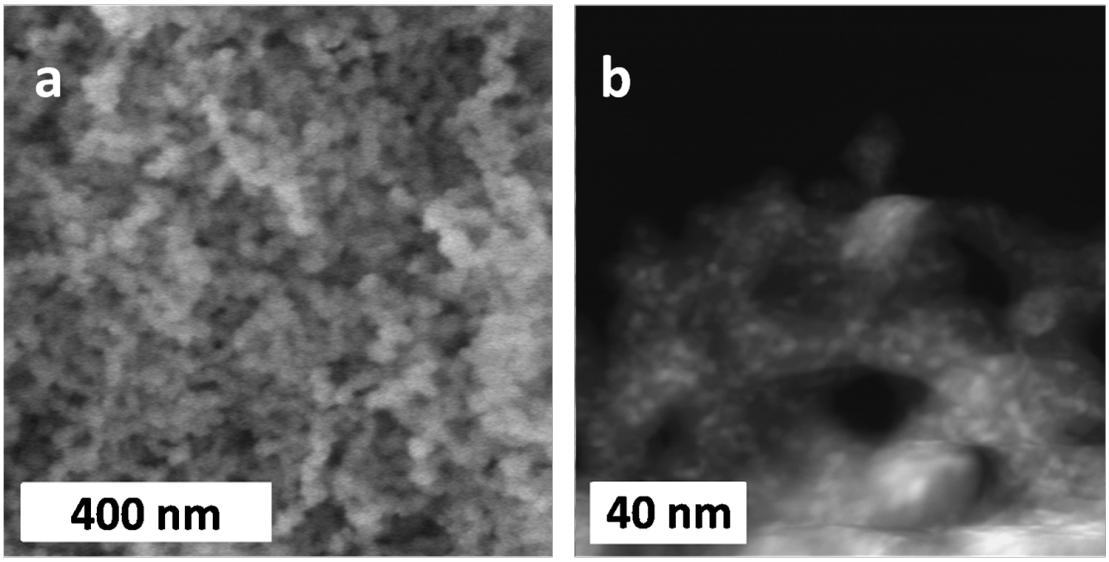

Figure 8.6: (a) SEM image and (b) HAADF–STEM image of the $(SiO_2)_{90}(GeO_2)_{10}$ composite before calcination, which indicates the presence of germania particles (~3 nm diameter) embedded in the silica nanoparticle matrix.

$$GeO_2(s) + 2H_2(g) \xrightarrow{400\ ^\circ C} Ge(s) + 2H_2O(g) \tag{8.8}$$

The germanium nanocrystals were isolated by oxide stripping and drying the powder. The germanium nanoparticles were mixed with PEDOT:PSS solutions and spincast onto glass slides to yield a film with thickness of ~40 nm. An ethylene glycol treatment of the film was used to improve the dopant activation of the PEDOT:PSS. Raman spectra of the PEDOT:PSS film and the PEDOT:PSS/Ge film are shown in Figure 8.7, which indicate an enhancement effect due to the presence of the germanium nanocrystals. Germanium has a large excitonic Bohr radius of 24.3 nm so the electronic structure at this scale may prove usefull.

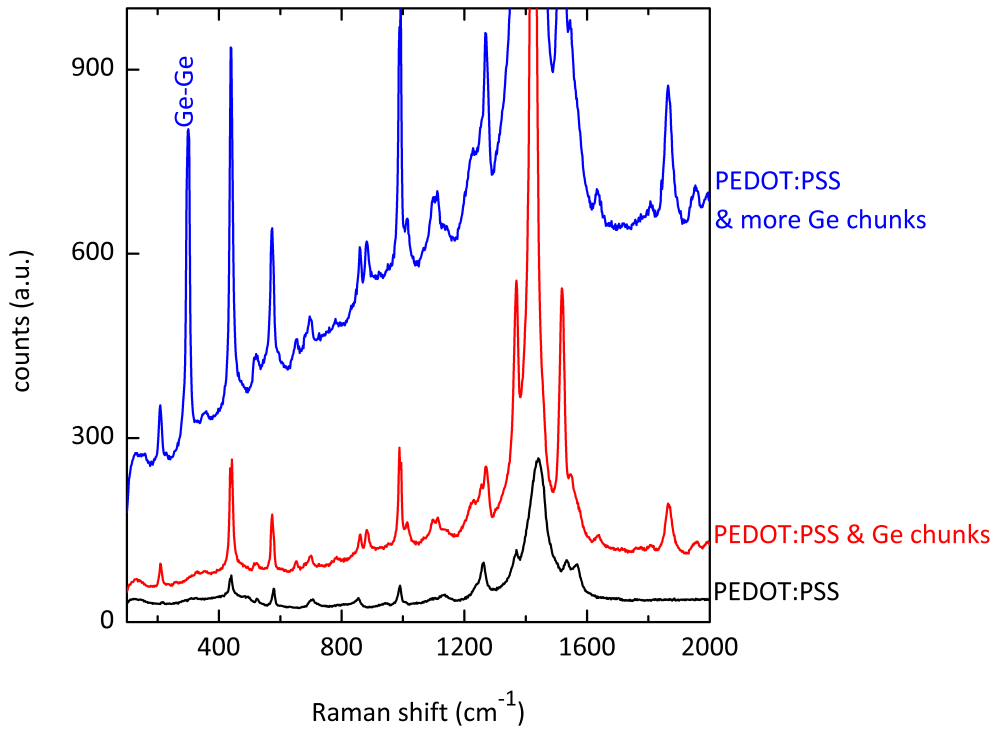

Figure 8.7: Raman spectra of PEDOT:PSS/Ge nanocrystal films indicate a Raman scattering enhancement due to the germanium nanocrystals.

Electrical resistivity was determined according to the van der Pauw method.[62] And Seebeck coefficients were measured; however the preliminary PEDOT:PSS and PEDOT:PSS/Ge films exhibited approximately the same thermoelectric power factor due to the high and unoptimized carrier density of the PEDOT:PSS and low weight percent of germanium used.

Furthermore, our preliminary processing method introduced extended defects like the fiber shown in Figure 8.8. Microscope analysis of this fiber indicated that this fiber was slightly elevated above the average film thickness and a Raman linescan indicated that this fiber had more scattering from the PEDOT band that is assigned to the ring C–C stretching vibration that is attributed to "neutral parts existing between localized elementary excitations such as positive polarons or bipolarons generated upon doping."[183, 184]

8.3.3 Proposal

We will:

- Improve the film processing so that the film doesn't appear to have phase segregated regions or fibers.

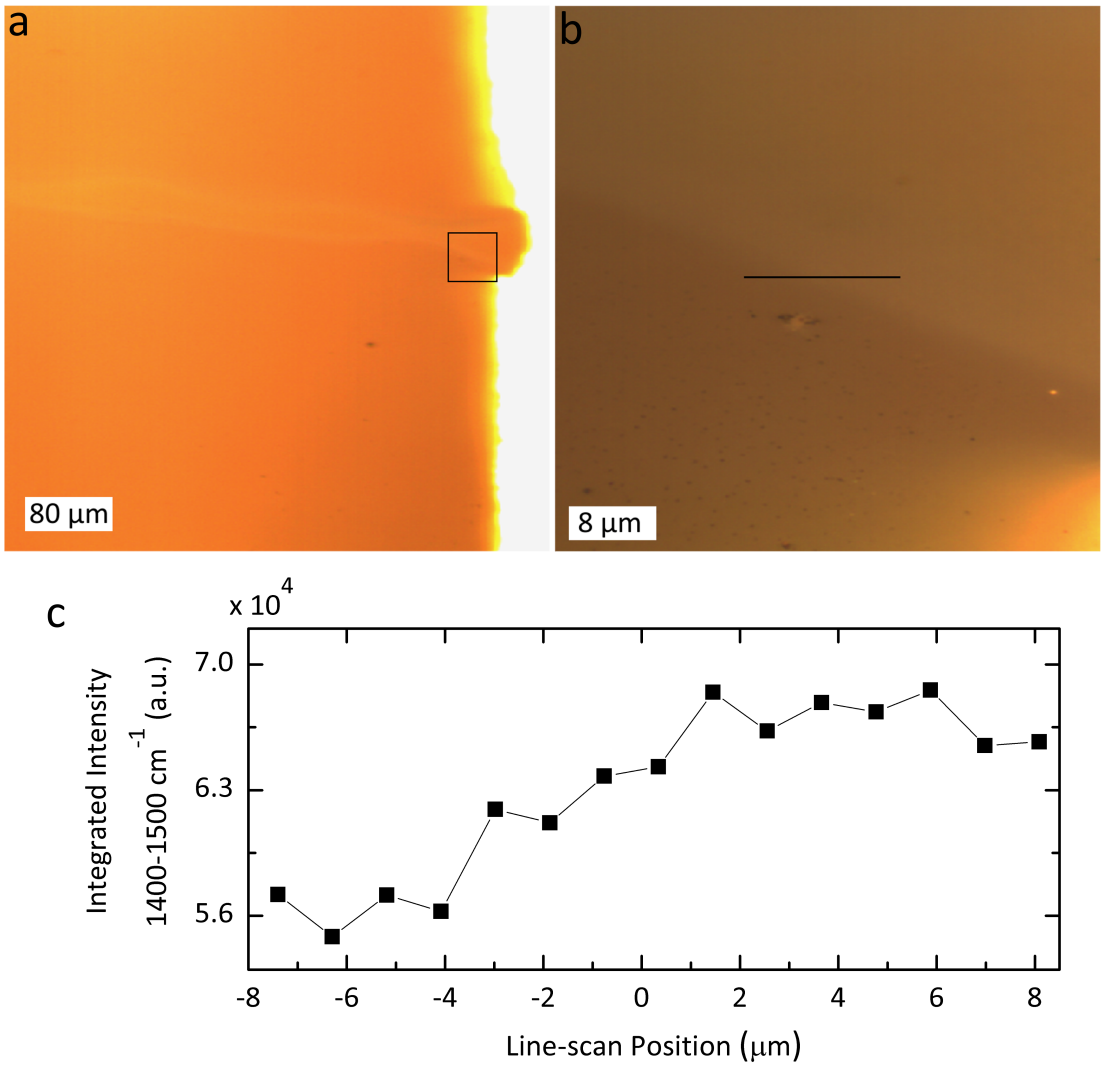

Figure 8.8: (a) Optical micrograph of a fiber-like region in the ethylene glycol treated PEDOT:PSS/Ge film, (b) higher magnification of the boxed region in (a) and the direction of the (c) Raman linescan that shows chemical inhomogeneity.

- Develop diborane doping procedure for the germanium so that we can control the germanium's Fermi level and therefore, the Schottky barrier height/energy filter.

- Demonstrate hole gas transport in the PEDOT:PSS/i-Ge/PEDOT:PSS structure.

- Tune the interfacial potential by functionalizing the Ge surface [185] and/or electropolymerizing the PEDOT:PSS directly onto the Ge.

- Prepare various mesoporous Ge films for controllable interfaces and determine the ideal phase domain size to enhance the thermoelectric properties. We have experience preparing various mesoporous oxides, as shown in Figure 8.9 and we can reduce those oxides to the elemental state, whilst maintaining the original microstructure.

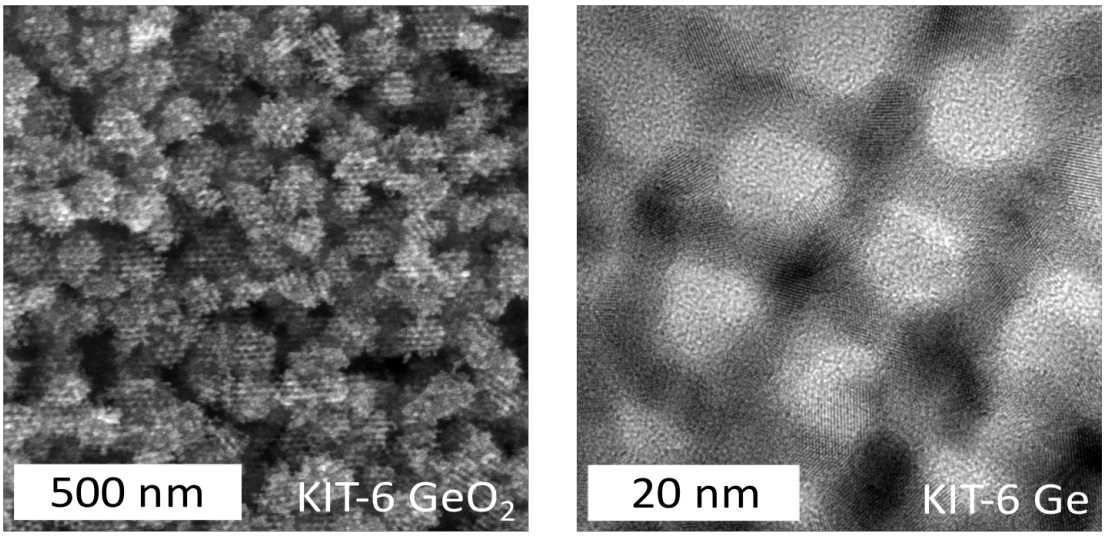

Figure 8.9: Mesoporous KIT-6 GeO_2 that was then reduced to a nanocrystalline, mesoporous Ge by a low temperature H_2 treatment. (Unpublished results by and with permission of Shi [186].)

Chapter 9

Conclusions

9.1 Overview and Summary

We have demonstrated that conversion of dilute borosilicate-germanates and phosphosilicate-germanates to doped silicon germanium nanocomposites by the magnesiothermic reduction is an effective method to prepare functional $Si_{1-x}Ge_x$ for thermoelectric conversion.

As Figure 9.1a shows, we have been able to produce p-type and n-type $Si_{1-x}Ge_x$ and have demonstrated Seebeck coefficients competitive with the literature record for ball milled and hot pressed $Si_{80}Ge_{20}$ nanocomposites.

We have optimized the p-type $Si_{1-x}Ge_x$ to have an electrical conductivity that is competitive with the literature record for ball milled and hot pressed $Si_{80}Ge_{20}$ nanocomposites (see Fig. 9.1b); however, our n-type $Si_{1-x}Ge_x$ suffers

from compensation due to an unintentional boron doping, which is currently limiting the electrical conductivity of those alloys.

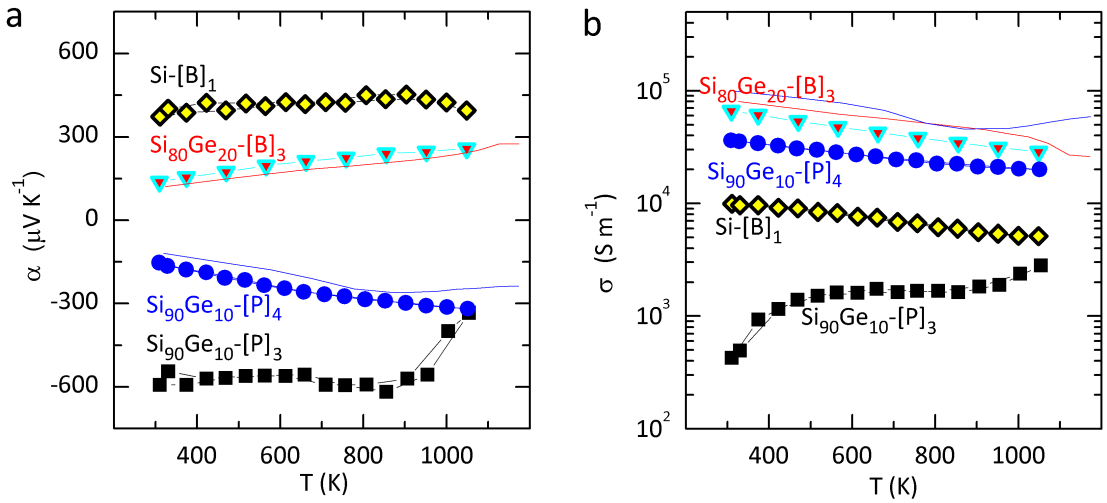

Figure 9.1: Summary of the doping control that we have developed to optimize (a) Seebeck coefficient and (b) electrical conductivity by controlling the doping during the sol-gel synthesis of dilute borosilicate-germanates and phosphosilicate-germanates. The blue trace is the data for n-type $Si_{80}Ge_{20}$ nanocomposite reported by Wang et al. and the red trace is the p-type $Si_{80}Ge_{20}$ nanocomposite data reported by Joshi et al..[20, 21] (Adapted with permission from Snedaker et al. [128]. Copyright 2013 American Chemical Society.)

We have demonstrated the effect of rapid consolidation on our $(Si)_{1-x}(Ge)_x$, which produces a heterogeneous alloy with a reduction in lattice thermal conductivity. However, that process is not optimized and the thermoelectric figure of merit should be improved with a higher germanium content, more alloy homogeneity, and a lower carrier density (see Fig. 9.2).

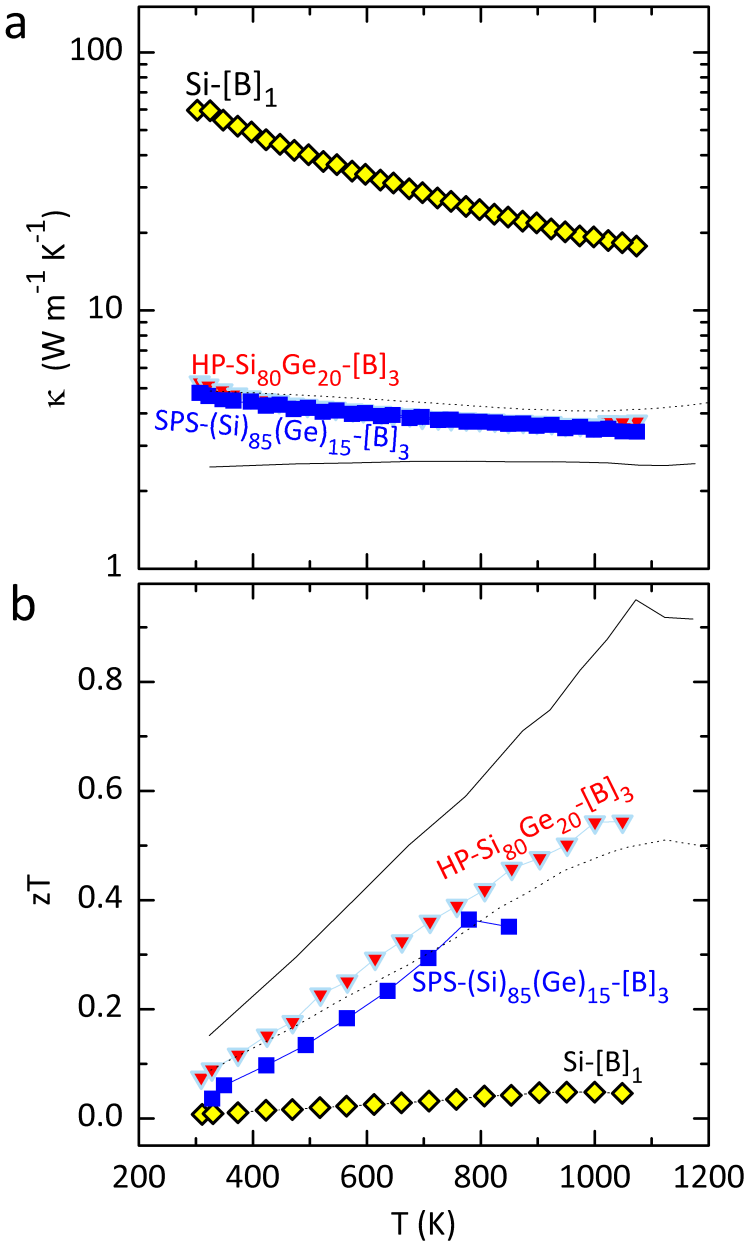

Figure 9.2: Summary of the control that we have demonstrated over (a) thermal conductivity and (b) the thermoelectric figure of merit through the magnesiothermic reduction of a silica-germania nanocomposite. The solid trace is the data for the p-type $Si_{80}Ge_{20}$ nanocomposite data reported by Joshi et al. and the RTG-$Si_{80}Ge_{20}$ that they compare to is shown with a dotted trace.[21] (Adapted with permission from Snedaker et al. [128]. Copyright 2013 American Chemical Society.)

We have demonstrated the effect that the reduction medium of molten salts has on the extent of alloying and grain growth. If the reduction conditions are properly engineered it may be possible to prepare $Si_{1-x}Ge_x$ nanostructures with the desired dopant distribution in arbitrary shapes and sizes.

9.2 Outlook

9.2.1 Cost

Using the cost of the precursors that we use compared to the cost of the metallurgical grade silicon and germanium from Alfa Aesar, we see that our process method is more expensive than the conventional, carbothermal reduction route. However, the price of the alkoxide precursors is likely more expensive because the demand for silicon has resulted in the industry and economy that makes metallurgical grade silicon less expensive.

9.2.2 Diatom factory farms?

It would be neat if the bioengineering of diatoms was advanced such that silica structures could be prepared with the desired porosity, structure, and impurity compositions necessary to yield functional polycrystalline doped-$Si_{1-x}Ge_x$.

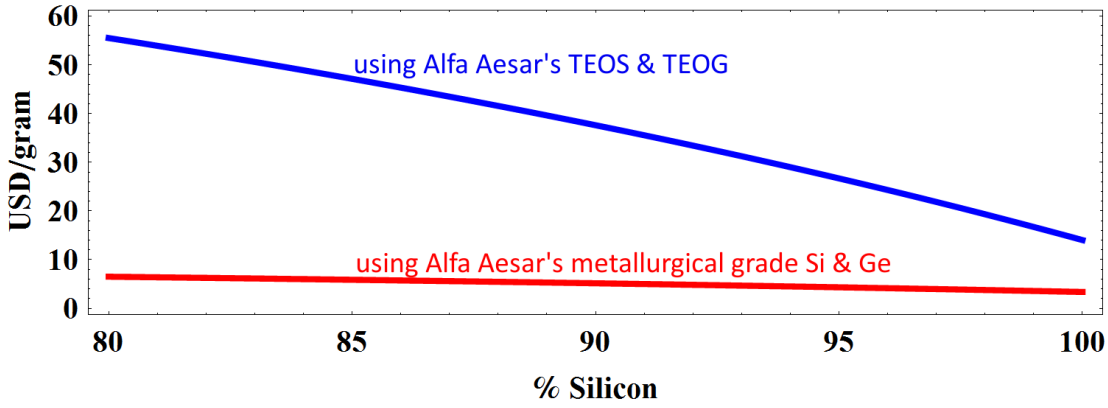

Figure 9.3: The cost of this alternative process based on the cost of Alfa Aesar's alkoxide precursors and metallurgical grade Si & Ge.

9.2.3 The allotropes of silicon

Silicon is amazing since it's so Earth abundant and we've learned how to control its properties down to the scale where it is no longer semiconducting. Our semiconductor industry has been made possible by silicon in the diamond cubic structure; however, there are allotropes of silicon that exhibit different properties. Although it is metastable at ambient pressure, silicon that crystallizes in the wurtzite or recently discovered orthorhombic structure can be stable for some period of time. Allotropes of silicon have received growing interest because they exhibit a quasidirect bandgap and can emit light! [187–190].

Appendices

Appendix A

Effective medium model for electrical conductivity:

This effective medium calculation for electrical conductivity of the host matrix in the hot pressed $Si_{1-x}Ge_x$ is performed according to previous considerations of electrical transport in porous materials.[30, 191, 192]

$$\sigma_{effective} = \sigma_{host}\frac{2-3\Phi}{2} \qquad \Phi \equiv \frac{pore\ volume}{total\ volume}$$

$$\frac{\sigma_{effective,\ Sample\ A}}{\sigma_{effective,\ Sample\ B}} = \frac{\sigma_{host,\ Sample\ A}}{\sigma_{host,\ Sample\ B}}\frac{2-3\Phi_{\ Sample\ A}}{2-3\Phi_{\ Sample\ B}}$$

$$\Phi_{Si_{90}Ge_{10}-[B]_2} \approx 0.04$$

$$\Phi_{Si_{90}Ge_{10}-[B]_4} \approx 0.02$$

$$\frac{\sigma_{effective,\ Si_{90}Ge_{10}-[B]_2}}{\sigma_{effective,\ Si_{90}Ge_{10}-[B]_4}} = \frac{\sigma_{host,\ Si_{90}Ge_{10}-[B]_2}}{\sigma_{host,\ Si_{90}Ge_{10}-[B]_4}} \times 0.969$$

$$\sigma_{effective,\ Si_{90}Ge_{10}-[B]_2}(T = 300\ K) \approx 2.2 \times 10^4\ S/m$$

$$\sigma_{effective,\ Si_{90}Ge_{10}-[B]_4}(T = 300\ K) \approx 6.0 \times 10^4\ S/m$$

$$\frac{2.2 \times 10^4\ S/m}{6 \times 10^4\ S/m} = 0.367 \approx \frac{\sigma_{host,\ Si_{90}Ge_{10}-[B]_2}}{\sigma_{host,\ Si_{90}Ge_{10}-[B]_4}} \times 0.969$$

$$\frac{\sigma_{host,\ Si_{90}Ge_{10}-[B]_2}}{\sigma_{host,\ Si_{90}Ge_{10}-[B]_4}} \approx 0.378$$

$\therefore$ The electrical conductivity of the $Si_{90}Ge_{10}-[B]_2$ host matrix (i.e. the conducting phase) is about 38% of the electrical conductivity of the $Si_{90}Ge_{10}-[B]_4$ host matrix at room temperature. Variation in the thermoelectric properties of our samples is not due to a density/porosity effect. The modulation of the electronic properties was achieved by tuning the carrier density.

Consider our results from the room temperature Hall effect measurements:

$$\frac{\sigma_{effective,\ Si_{90}Ge_{10}-[B]_2}}{\sigma_{effective,\ Si_{90}Ge_{10}-[B]_4}} = \frac{p_{Si_{90}Ge_{10}-[B]_2}\ \mu_{Si_{90}Ge_{10}-[B]_2}}{p_{Si_{90}Ge_{10}-[B]_4}\ \mu_{Si_{90}Ge_{10}-[B]_4}} = 0.386$$

The discrepancy between the effective electrical conductivities and host electrical conductivities of the two samples with the most different densities (94.7% vs. 98.0%) is due to different carrier densities in the conducting SiGe host matrix. The $\sim$2% discrepancy between effective and host electrical conductivities may be attibuted to a difference in densities or sample quality.

Bibliography

[1] Snyder, G. J.; Toberer, E. S. Complex thermoelectric materials. *Nature Materials* **2008**, *7*, 105–114.

[2] Nolas, G. S.; Sharp, J.; Goldsmid, H. J. In *Thermoelectrics: basic principles and new materials developments*; Zunger, A., Osgood Jr., R. M., Hull, R., Sakaki, H., Eds.; Springer-Verlag Berlin Heidelberg, 2010.

[3] Curtin, B. M. Improvement and Integration of Silicon Nanowires for Thermoelectric Applications. 2014; `http://search.proquest.com/docview/1530436324?accountid=14522`, Copyright - Copyright ProQuest, UMI Dissertations Publishing 2014; Last updated - 2014-06-24; First page - n/a.

[4] Vining, C. B. An inconvenient truth about thermoelectrics. *Nature Materials* **2009**, *8*, 83–85.

[5] Dames, C. MRS 2008 Fall (unpublished figure); adapted from Dames, C & Chen, G., "Thermal conductivity of nanostructured thermoelectric materials," invited chapter in Thermoelectrics Handbook: Macro to Nano, Chapter 42, CRC Press, ed. D. Rowe, 2005.

[6] Rowe, D. *Thermoelectrics Handbook: Macro to Nano*; Taylor & Francis, 2005.

[7] Haxel, G. B.; Boore, S.; Mayfield, S.; User:michbich, Relative abundance of elements in the Earth's upper crust. online (USGS and wikipedia), 2003; `http://commons.wikimedia.org/wiki/File:Elemental_abundances.svg`.

[8] Zhang, H.; Liu, C.-X.; Qi, X.-L.; Dai, X.; Fang, Z.; Zhang, S.-C. Topological insulators in Bi_2Se_3, Bi_2Te_3 and Sb_2Te_3 with a single Dirac cone on the surface. *Nature Physics* **2009**, *5*, 438–442.

[9] Moore, J. E. The birth of topological insulators. *Nature* **2010**, *464*, 194–198.

[10] Qi, X.-L.; Zhang, S.-C. Topological insulators and superconductors. *Rev. Mod. Phys.* **2011**, *83*, 1057–1110.

[11] Minnich, A. J.; Dresselhaus, M. S.; Ren, Z. F.; Chen, G. Bulk nanostructured thermoelectric materials: current research and future prospects. *Energy & Environmental Science* **2009**, *2*, 466–479.

[12] Bux, S. K.; Rodriguez, M.; Yeung, M. T.; Yang, C.; Makhluf, A.; Blair, R. G.; Fleurial, J.-P.; Kaner, R. B. Rapid Solid-State Synthesis of Nanostructured Silicon. *Chemistry of Materials* **2010**, *22*, 2534–2540.

[13] Kaner, R.; Bux, S.; Fleurial, J.; Rodriguez, M. Rapid solid-state metathesis routes to nanostructured silicon-germainum. 2011; `http://www.google.com/patents/US20110318250`, US Patent App. 13/155,853.

[14] Ikeda, T.; Haviez, L.; Li, Y.; Snyder, G. J. Nanostructuring of Thermoelectric Mg_2Si via a Nonequilibrium Intermediate State. *Small* **2012**, *8*, 2350–2355.

[15] Yi, T.; Chen, S.; Li, S.; Yang, H.; Bux, S.; Bian, Z.; Katcho, N. A.; Shakouri, A.; Mingo, N.; Fleurial, J.-P.; Browning, N. D.; Kauzlarich, S. M. Synthesis and characterization of Mg_2Si/Si nanocomposites prepared from MgH_2 and silicon, and their thermoelectric properties. *Journal of Materials Chemistry* **2012**, *22*, 24805–24813.

[16] Dresselhaus, M.; Chen, G.; Tang, M.; Yang, R.; Lee, H.; Wang, D.; Ren, Z.; Fleurial, J.-P.; Gogna, P. New Directions for Low-Dimensional Thermoelectric Materials. *Advanced Materials* **2007**, *19*, 1043–1053.

[17] Rowe, D. M.; Shukla, V. S.; Savvides, N. Phonon scattering at grain boundaries in heavily doped fine-grained silicon-germanium alloys. *Nature* **1981**, *290*, 765–766.

[18] Zhu, G. H.; Lee, H.; Lan, Y. C.; Wang, X. W.; Joshi, G.; Wang, D. Z.; Yang, J.; Vashaee, D.; Guilbert, H.; Pillitteri, A.; Dresselhaus, M. S.; Chen, G.; Ren, Z. F. Increased Phonon Scattering by Nanograins and Point Defects in Nanostructured Silicon with a Low Concentration of Germanium. *Physical Review Letters* **2009**, *102*, 196803.

[19] Bux, S. K.; Blair, R. G.; Gogna, P. K.; Lee, H.; Chen, G.; Dresselhaus, M. S.; Kaner, R. B.; Fleurial, J.-P. Nanostructured Bulk Silicon as an Effective Thermoelectric Material. *Advanced Functional Materials* **2009**, *19*, 2445–2452.

[20] Wang, X. W.; Lee, H.; Lan, Y. C.; Zhu, G. H.; Joshi, G.; Wang, D. Z.; Yang, J.; Muto, A. J.; Tang, M. Y.; Klatsky, J.; Song, S.; Dresselhaus, M. S.; Chen, G.; Ren, Z. F. Enhanced thermoelectric figure of merit in nanostructured n-type silicon germanium bulk alloy. *Applied Physics Letters* **2008**, *93*, 193121.

[21] Joshi, G.; Lee, H.; Lan, Y.; Wang, X.; Zhu, G.; Wang, D.; Gould, R. W.; Cuff, D. C.; Tang, M. Y.; Dresselhaus, M. S.; Chen, G.; Ren, Z. Enhanced Thermoelectric Figure-of-Merit in Nanostructured p-type Silicon Germanium Bulk Alloys. *Nano Letters* **2008**, *8*, 4670–4674, PMID: 18973391.

[22] Hochbaum, A. I.; Chen, R.; Delgado, R. D.; Liang, W.; Garnett, E. C.; Najarian, M.; Majumdar, A.; Yang, P. Enhanced thermoelectric performance of rough silicon nanowires. *Nature* **2008**, *451*, 163–167.

[23] Boukai, A. I.; Bunimovich, Y.; Tahir-Kheli, J.; Yu, J.-K.; Goddard III, W. A.; Heath, J. R. Silicon nanowires as efficient thermoelectric materials. *Nature* **2008**, *451*, 168–171.

[24] Tang, J.; Wang, H.-T.; Lee, D. H.; Fardy, M.; Huo, Z.; Russell, T. P.; Yang, P. Holey Silicon as an Efficient Thermoelectric Material. *Nano Letters* **2010**, *10*, 4279–4283, PMID: 20839780.

[25] Curtin, B. M.; Fang, E. W.; Bowers, J. E. Highly Ordered Vertical Silicon Nanowire Array Composite Thin Films for Thermoelectric Devices. *Journal of Electronic Materials* **2012**, *41*, 887–894.

[26] Curtin, B. M.; Bowers, J. E. Thermoelectric Properties of Silicon Nanowire Array and Spin-on Glass Composites Fabricated with CMOS-compatible Techniques. Symposium BB – Functional Nanowires and Nanotubes. 2012.

[27] Stahlkocher, Monokristalines Silizium für die Waferherstellung. online (German Wikipedia), 2004; `http://upload.wikimedia.org/wikipedia/commons/2/23/Monokristalines_Silizium_f%C3%BCr_die_Waferherstellung.jpg`.

[28] Lee, J.-H.; Galli, G. A.; Grossman, J. C. Nanoporous Si as an Efficient Thermoelectric Material. *Nano Letters* **2008**, *8*, 3750–3754, PMID: 18947211.

[29] Lee, J.-H.; Grossman, J. C. Thermoelectric properties of nanoporous Ge. *Applied Physics Letters* **2009**, *95*.

[30] Lee, H.; Vashaee, D.; Wang, D. Z.; Dresselhaus, M. S.; Ren, Z. F.; Chen, G. Effects of nanoscale porosity on thermoelectric properties of SiGe. *Journal of Applied Physics* **2010**, *107*, 094308.

[31] Yang, L.; Yang, N.; Li, B. Reduction of Thermal Conductivity by Nanoscale 3D Phononic Crystal. *Scientific Reports* **2013**, *3*, 1–5.

[32] Mingo, N.; Hauser, D.; Kobayashi, N. P.; Plissonnier, M.; Shakouri, A. "Nanoparticle-in-Alloy" Approach to Efficient Thermoelectrics: Silicides in SiGe. *Nano Letters* **2009**, *9*, 711–715, PMID: 19128146.

[33] Heremans, J. P.; Jovovic, V.; Toberer, E. S.; Saramat, A.; Kurosaki, K.; Charoenphakdee, A.; Yamanaka, S.; Snyder, G. J. Enhancement of Thermoelectric Efficiency in PbTe by Distortion of the Electronic Density of States. *Science* **2008**, *321*, 554–557.

[34] Zebarjadi, M.; Joshi, G.; Zhu, G.; Yu, B.; Minnich, A.; Lan, Y.; Wang, X.; Dresselhaus, M.; Ren, Z.; Chen, G. Power Factor Enhancement by Modulation Doping in Bulk Nanocomposites. *Nano Letters* **2011**, *11*, 2225–2230, PMID: 21553899.

[35] Yu, B.; Zebarjadi, M.; Wang, H.; Lukas, K.; Wang, H.; Wang, D.; Opeil, C.; Dresselhaus, M.; Chen, G.; Ren, Z. Enhancement of Thermoelectric Properties by Modulation-Doping in Silicon Germanium Alloy Nanocomposites. *Nano Letters* **2012**, *12*, 2077–2082, PMID: 22435933.

[36] Moon, J.; Kim, J.-H.; Chen, Z. C.; Xiang, J.; Chen, R. Gate-Modulated Thermoelectric Power Factor of Hole Gas in Ge-Si Core-Shell Nanowires. *Nano Letters* **2013**, *13*, 1196–1202, PMID: 23394480.

[37] Curtin, B. M.; Codecido, E. A.; Kraemer, S.; Bowers, J. E. Field-Effect Modulation of Thermoelectric Properties in Multigated Silicon Nanowires. *Nano Letters* **2013**, *13*, 5503–5508, PMID: 24138582.

[38] Curtin, B. M.; Bowers, J. E. Thermoelectric power factor enhancement with gate-all-around silicon nanowires. *Journal of Applied Physics* **2014**, *115*, 143704.

[39] Zide, J.; Vashaee, D.; Bian, Z.; Zeng, G.; Bowers, J.; Shakouri, A.; Gossard, A. Demonstration of electron filtering to increase the Seebeck coefficient in $In_{0.53}Ga_{0.47}As/In_{0.53}Ga_{0.28}Al_{0.19}As$ superlattices. *Phys. Rev. B* **2006**, *74*, 205335.

[40] Narduccia, D.; Seleznevaa, E.; Cerofolinia, G.; Frabbonic, S.; Ottavianic, G. Impact of energy filtering and carrier localization on the thermoelectric properties of granular semiconductors. *Journal of Solid State Chemistry* **2012**, *193*, 19–25.

[41] Van de Walle, C.; Martin, R. Theoretical calculations of heterojunction discontinuities in the Si/Ge system. *Phys. Rev. B* **1986**, *34*, 5621–5634.

[42] Wang, K.; Thomas, S.; Tanner, M. SiGe band engineering for MOS, CMOS and quantum effect devices. *Journal of Materials Science: Materials in Electronics* **1995**, *6*, 311–324.

[43] Lu, W.; Xiang, J.; Timko, B. P.; Wu, Y.; Lieber, C. M. One-dimensional hole gas in germanium/silicon nanowire heterostructures. *Proceedings of the National Academy of Sciences of the United States of America* **2005**, *102*, 10046–10051.

[44] Xiang, J.; Lu, W.; Hu, Y.; Wu, Y.; Yan, H.; Lieber, C. M. Ge/Si nanowire heterostructures as high-performance field-effect transistors. *Nature* **2006**, *441*, 489–493.

[45] Zhang, Y. Chemical Approaches for Hetero-structured Thermoelectric Materials. 2013; `http://search.proquest.com/docview/1445013891?accountid=14522`, Copyright - Copyright ProQuest, UMI Dissertations Publishing 2013; Last updated - 2014-01-21; First page - n/a.

[46] Coelho, A. TOPAS Academic, Version 4.1. Coelho Software: Brisbane, Australia, 2007.

[47] Stöhr, H.; Klemm, W. Uber Zweistoffsysteme mit Germanium. I. Germanium/Aluminium, Germanium/Zinn und Germanium/Silicium. *Zeitschrift für anorganische und allgemeine Chemie* **1939**, *241*, 305–323.

[48] Yim, W. M.; Paff, R. J. Thermal expansion of AlN, sapphire, and silicon. *Journal of Applied Physics* **1974**, *45*, 1456–1457.

[49] Okhotin, A. S.; Pushkarskii, A. S.; Gorbachev, V. V. In *Thermophysical Properties of Semiconductors*; Okhotin, A. S., Pushkarskii, A. S., Gorbachev, V. V., Eds.; "Atom" Publ. House: Moscow, Russia, 1972.

[50] Shanks, H.; Maycock, P.; Sidles, P.; Danielson, G. Thermal Conductivity of Silicon from 300 to 1400K. *Phys. Rev.* **1963**, *130*, 1743–1748.

[51] Glassbrenner, C.; Slack, G. Thermal Conductivity of Silicon and Germanium from 3K to the Melting Point. *Phys. Rev.* **1964**, *134*, A1058–A1069.

[52] Desai, P. D. Thermodynamic Properties of Iron and Silicon. *Journal of Physical and Chemical Reference Data* **1986**, *15*, 967–983.

[53] Stöhr, H.; Klemm, W. *Z. Anorg. Allg. Chem.* **1954**, *241*, 304, I am not certain if this German study was properly cited, as I haven't been able to find it but it is cited as this in subsequent studies.

[54] Levinshtein, M.; Rumyantsev, S.; Shur, M. *Properties of Advanced Semiconductor Materials: GaN, AIN, InN, BN, SiC, SiGe*; A Wiley-Interscience publication; John Wiley and Sons, 2001.

[55] Abeles, B.; Beers, D.; Cody, G.; Dismukes, J. Thermal Conductivity of Ge-Si Alloys at High Temperatures. *Phys. Rev.* **1962**, *125*, 44–46.

[56] Abeles, B. Lattice Thermal Conductivity of Disordered Semiconductor Alloys at High Temperatures. *Phys. Rev.* **1963**, *131*, 1906–1911.

[57] Garg, J.; Bonini, N.; Kozinsky, B.; Marzari, N. Role of Disorder and Anharmonicity in the Thermal Conductivity of Silicon-Germanium Alloys: A First-Principles Study. *Phys. Rev. Lett.* **2011**, *106*, 045901.

[58] Vick, G. L.; Whittle, K. M. Solid Solubility and Diffusion Coefficients of Boron in Silicon. *Journal of The Electrochemical Society* **1969**, *116*, 1142–1144.

[59] Samsonov, G.; Sleptsov, V. M. Investigation of the Solubility of Boron in Silicon. *Zh. Neorg. Khim. (Russian)* **1963**, *8*, 2009–2011, 2E20 B cm^{-3} in c-Si at 900C.

[60] Hull, R. In *Properties of Crystalline Silicon*; Hull, R., Ed.; EMIS datareviews series; INSPEC, the Institution of Electrical Engineers, 1999; Chapter 10: 3E20 P cm^{-3} in c-Si at 900C.

[61] Sze, S.; Irvin, J. Resistivity, mobility and impurity levels in GaAs, Ge, and Si at 300K. *Solid-State Electronics* **1968**, *11*, 599–602.

[62] van der Pauw, L. J. A Method of Measuring Specific Resistivity and Hall Effect of Discs of Arbitrary Shapes. *Philips Research Reports* **1958**, *13*, 1–9.

[63] Uhlir, A. Electrolytic Shaping of Germanium and Silicon. *Bell System Technical Journal* **1956**, *35*, 333–347.

[64] Canham, L. T. Silicon quantum wire array fabrication by electrochemical and chemical dissolution of wafers. *Applied Physics Letters* **1990**, *57*, 1046–1048.

[65] Gesele, G.; Linsmeier, J.; Drach, V.; Fricke, J.; Arens-Fischer, R. Temperature-dependent thermal conductivity of porous silicon. *Journal of Physics D: Applied Physics* **1997**, *30*, 2911, The measured thermal conductivities were three to five orders of magnitude smaller than the values for bulk silicon.

[66] Canham, L. *Properties of Porous Silicon*; EMIS datareviews series : Electronic Materials Information Service datareviews series; INSPEC, 1997; Chapter 1: Drying of porous silicon; Chapter 3: Skeleton Structure; Chapter 6: Resistivity of porous silicon; Chapter 8: Dopants in porous silicon.

[67] Sailor, M. J. Electrochemical etching cell used to prepare porous Si from single crystal Si wafers. online, 2003; `http://sailorgroup.ucsd.edu/research/porous_Si_intro.html`.

[68] Zwick, A.; Carles, R. Multiple-order Raman scattering in crystalline and amorphous silicon. *Phys. Rev. B* **1993**, *48*, 6024–6032.

[69] Lin, V. S.-Y.; Motesharei, K.; Dancil, K.-P. S.; Sailor, M. J.; Ghadiri, M. R. A Porous Silicon-Based Optical Interferometric Biosensor. *Science* **1997**, *278*, 840–843.

[70] Park, J.-H.; Gu, L.; von Maltzahn, G.; Ruoslahti, E.; Bhatia, S. N.; Sailor, M. J. Biodegradable luminescent porous silicon nanoparticles for in vivo applications. *Nature Materials* **2009**, *8*, 331–336.

[71] Ruminski, A. M.; Barillaro, G.; Chaffin, C.; Sailor, M. J. Internally Referenced Remote Sensors for HF and Cl_2 Using Reactive Porous Silicon Photonic Crystals. *Advanced Functional Materials* **2011**, *21*, 1511–1525.

[72] Gu, L.; Hall, D. J.; Qin, Z.; Anglin, E.; Joo, J.; Mooney, D. J.; Howell, S. B.; Sailor, M. J. In Vivo Time-gated Fluorescence Imaging with Biodegradable Luminescent Porous Silicon Nanoparticles. *Nature Communications* **2013**, *4*.

[73] Sailor, M. J. *Porous Silicon in Practice*; Wiley-VCH Verlag GmbH & Co. KGaA, 2011; pp I–XII.

[74] Shi, Y.; Zhang, F.; Hu, Y.-S.; Sun, X.; Zhang, Y.; Lee, H. I.; Chen, L.; Stucky, G. D. Low-Temperature Pseudomorphic Transformation of Ordered Hierarchical Macro-mesoporous SiO_2/C Nanocomposite to SiC via Magnesiothermic Reduction. *Journal of the American Chemical Society* **2010**, *132*, 5552–5553, PMID: 20356306.

[75] Fang, J.; Kang, C. B.; Huang, Y.; Tolbert, S. H.; Pilon, L. Thermal Conductivity of Ordered Mesoporous Nanocrystalline Silicon Thin Films Made from Magnesium Reduction of Polymer-Templated Silica. *The Journal of Physical Chemistry C* **2012**, *116*, 12926–12933.

[76] Bao, Z.; Weatherspoon, M. R.; Shian, S.; Cai, Y.; Graham, P. D.; Allan, S. M.; Ahmad, G.; Dickerson, M. B.; Church, B. C.; Kang, Z.; Abernathy III, H. W.; Summers, C. J.; Liu, M.; Sandhage, K. H. Chemical reduction of three-dimensional silica micro-assemblies into microporous silicon replicas. *Nature* **2007**, *446*, 172–175.

[77] Szczech, J. R.; Jin, S. Mg_2Si nanocomposite converted from diatomaceous earth as a potential thermoelectric nanomaterial. *Journal of Solid State Chemistry* **2008**, *181*, 1565–1570.

[78] Liu, N.; Huo, K.; McDowell, M. T.; Zhao, J.; Cui, Y. Rice husks as a sustainable source of nanostructured silicon for high performance Li-ion battery anodes. *Scientific Reports* **2013**, *3*.

[79] Favors, Z.; Wang, W.; Bay, H. H.; Mutlu, Z.; Ahmed, K.; Liu, C.; Ozkan, M.; Ozkana, C. S. Scalable Synthesis of Nano-Silicon from Beach Sand for Long Cycle Life Li-ion Batteries. *Scientific Reports* **2014**, *4*.

[80] Jung, D. S.; Ryou, M.-H.; Sung, Y. J.; Park, S. B.; Choi, J. W. Recycling rice husks for high-capacity lithium battery anodes. *Proceedings of the National Academy of Sciences of the United States of America* **2013**, *110*, 12229–12234, "Rice is one of the most widespread food crops for human sustenance", "silica accounts for 15–20 wt.

[81] Deyhle, A.; Hodge, V.; Lewin, R. A. 33 Boron in diatoms. *Journal of Phycology* **2003**, *39*, 12–13.

[82] Stoll, H.; Mejia-Ramirez, L. M.; Isensee, K.; Mendez-Vicente, A.; Pisonero, J. Diatom biomineralization reflected in diatom B/Si. EGU General Assembly Conference Abstracts. 2012; p 3310.

[83] Lewin, J. Silicon Metabolism in Diatoms. V. Germanium Dioxide, a Specific Inhibitor of Diatom Growth. *Phycologia* **1966**, *6*, 1–12.

[84] Shea, R.; Chopin, T. Effects of germanium dioxide, an inhibitor of diatom growth, on the microscopic laboratory cultivation stage of the kelp, Laminaria saccharina. *Journal of Applied Phycology* **2007**, *19*, 27–32.

[85] Azam, F.; Hemmingsen, B.; Volcani, B. Germanium incorporation into the silica of diatom cell walls. *Archiv für Mikrobiologie* **1973**, *92*, 11–20.

[86] Rorrer, G. L.; Chang, C.-H.; Liu, S.-H.; Jeffryes, C.; Jiao, J.; Hedberg, J. A. Biosynthesis of Silicon Germanium Oxide Nanocomposites by the Marine Diatom Nitzschia frustulum. *Journal of Nanoscience and Nanotechnology* **2005**, *5*, 41–49.

[87] Shi, Y. Unpublished data, 2009.

[88] Reed, T. *Free Energy of Formation of Binary Compounds: An Atlas of Charts for High-temperature Chemical Calculations*; Biomass Energy Foundation Press, 2000.

[89] Zhao, D.; Feng, J.; Huo, Q.; Melosh, N.; Fredrickson, G. H.; Chmelka, B. F.; Stucky, G. D. Triblock Copolymer Syntheses of Mesoporous Silica with Periodic 50 to 300 Angstrom Pores. *Science* **1998**, *279*, 548–552.

[90] van Grieken, R.; Escola, J.; Moreno, J.; Rodríguez, R. Direct synthesis of mesoporous M-SBA-15 (M = Al, Fe, B, Cr) and application to 1-hexene oligomerization. *Chemical Engineering Journal* **2009**, *155*, 442–450.

[91] Shibata, S. Sol-gel-derived silica preforms for optical fibers. *Journal of Non-Crystalline Solids* **1994**, *178*, 272–283.

[92] Susa, K.; Matsuyama, I.; Satoh, S.; Suganuma, T. Sol-gel derived Ge-doped silica glass for optical fiber application: I. Preparation of gel and glass and their characterization. *Journal of Non-Crystalline Solids* **1990**, *119*, 21–28.

[93] Chen, D.-G.; Potter, B.; Simmons, J. GeO_2-SiO_2 thin films for planar waveguide applications. *Journal of Non-Crystalline Solids* **1994**, *178*, 135–147.

[94] Kirkbir, F.; Raychaudhuri, S. Sol-gel process for forming a germania-doped silica glass rod. 1993; `http://www.google.com/patents/US5254508`, US Patent 5,254,508.

[95] Majérusa, O.; Cormiera, L.; Neuvilleb, D.; Galoisya, L.; Calas, G. The structure of SiO_2-GeO_2 glasses: A spectroscopic study. *Journal of Non-Crystalline Solids* **2008**, *354*, 2004–2009.

[96] Costacurta, S.; Malfatti, L.; Kidchob, T.; Takahashi, M.; Mattei, G.; Bello, V.; Maurizio, C.; Innocenzi, P. Self-Assembled Mesoporous Silica-Germania Films. *Chemistry of Materials* **2008**, *20*, 3259–3265.

[97] Hosono, H.; Kawamura, K.-i.; Kawazoe, H.; Nishii, J. Nanometer-scale heterogeneity in SiO_2-GeO_2 glass preforms and fibers prepared by vapor phase axial deposition method. *Journal of Applied Physics* **1996**, *80*, 3115–3117.

[98] Hosono, H.; Kawamura, K.-i.; Kameshima, Y.; Kawazoe, H.; Matsunami, N.; Muta, K.-i. Nanometer-sized Ge particles in GeO_2-SiO_2 glasses produced by proton implantation: Combined effects of electronic excitation and chemical reaction. *Journal of Applied Physics* **1997**, *82*, 4232–4235.

[99] Nogami, M.; Abe, Y. Sol-gel method for synthesizing visible photoluminescent nanosized Ge-crystal-doped silica glasses. *Applied Physics Letters* **1994**, *65*, 2545–2547.

[100] Murthy, M. K.; Hill, H. Studies in Germanium Oxide Systems: III, Solubility of Germania in Water. *Journal of the American Ceramic Society* **1965**, *48*, 109–110.

[101] Shafer, E. C.; Roy, R. System GeO_2-SiO_2. Qtz = quartz; Trid = tridymite. *U.S. Army Signal Corps* **1956**, *Contract DA 36-039*, 63099.

[102] Levin, E.; Robbins, C.; Murdie, H.; Reser, M. *Phase Diagrams for Ceramists. 1969 Supplement*; Phase Diagrams for Ceramists: 1969 Supplement; The American Ceramic Society, 1969.

[103] Yan, N.; Wang, F.; Zhong, H.; Li, Y.; Wang, Y.; Hu, L.; Chen, Q. Hollow Porous SiO_2 Nanocubes Towards High-performance Anodes for Lithium-ion Batteries. *Scientifc Reports* **2013**, *3*, 3–6.

[104] Favors, Z.; Wang, W.; Bay, H. H.; George, A.; Ozkan, M.; Ozkan, C. S. Stable Cycling of SiO_2 Nanotubes as High-Performance Anodes for Lithium-Ion Batteries. *Scientific Reports* **2014**, *4*, 1–7.

[105] Jahel, A.; Darwiche, A.; Ghimbeu, C. M.; Vix-Guterl, C.; Monconduit, L. High cycleability nano-GeO_2/mesoporous carbon composite as enhanced energy storage anode material in Li-ion batteries. *Journal of Power Sources* **2014**, *269*, 755 – 759.

[106] Lv, D.; Gordin, M. L.; Yi, R.; Xu, T.; Song, J.; Jiang, Y.-B.; Choi, D.; Wang, D. GeO_x/Reduced Graphene Oxide Composite as an Anode for Li-Ion Batteries: Enhanced Capacity via Reversible Utilization of Li_2O along with Improved Rate Performance. *Advanced Functional Materials* **2014**, *24*, 1059–1066.

[107] Alonso, M.; Winer, K. Raman spectra of c -$Si_{1-x}Ge_x$ alloys. *Phys. Rev. B* **1989**, *39*, 10056–10062.

[108] Temple, P.; Hathaway, C. Multiphonon Raman Spectrum of Silicon. *Phys. Rev. B* **1973**, *7*, 3685–3697.

[109] Weinstein, B.; Piermarini, G. Raman scattering and phonon dispersion in Si and GaP at very high pressure. *Phys. Rev. B* **1975**, *12*, 1172–1186.

[110] Osswald, S.; Mochalin, V.; Havel, M.; Yushin, G.; Gogotsi, Y. Phonon confinement effects in the Raman spectrum of nanodiamond. *Phys. Rev. B* **2009**, *80*, 075419.

[111] Stöber, W.; Fink, A.; Bohn, E. Controlled growth of monodisperse silica spheres in the micron size range. *Journal of Colloid and Interface Science* **1968**, *26*, 62–69.

[112] Strandwitz, N. C.; Stucky, G. D. Hollow Microporous Cerium Oxide Spheres Templated By Colloidal Silica. *Chemistry of Materials* **2009**, *21*, 4577–4582.

[113] National Institute of Standards and Technology, Composition of Pyrex Glass. online, Retrieved on December 6, 2014; `http://physics.nist.gov/cgi-bin/Star/compos.pl?matno=169`.

[114] Shelby, J. E. Properties and structure of B_2O_3-GeO_2 glasses. *Journal of Applied Physics* **1974**, *45*, 5272–5277.

[115] Parashar, V. K.; Orhan, J.-B.; Sayah, A.; Cantoni, M.; Gijs, M. A. M. Borosilicate nanoparticles prepared by exothermic phase separation. *Nature Nanotechnology* **2008**, *3*, 589–594.

[116] Tian, F.; Pan, L.; Wu, X.; Wu, F. The {NMR} studies of the P_2O_5-SiO_2 sol and gel chemistry. *Journal of Non-Crystalline Solids* **1988**, *104*, 129 – 134.

[117] Kim, Y.; Tressler, R. Microstructural evolution of sol-gel-derived phosphosilicate gel with heat treatment. *Journal of Materials Science* **1994**, *29*, 2531–2535.

[118] Massiot, P.; Centeno, M.; Carrizosa, I.; Odriozola, J. Thermal evolution of sol-gel-obtained phosphosilicate solids (SiPO). *Journal of Non-Crystalline Solids* **2001**, *292*, 158 – 166.

[119] Aronne, A.; Turco, M.; Bagnasco, G.; Pernice, P.; Di Serio, M.; Clayden, N. J.; Marenna, E.; Fanelli, E. Synthesis of High Surface Area Phosphosilicate Glasses by a Modified Sol-Gel Method. *Chemistry of Materials* **2005**, *17*, 2081–2090.

[120] Cireli, A.; Onar, N.; Ebeoglugil, M. F.; Kayatekin, I.; Kutlu, B.; Culha, O.; Celik, E. Development of flame retardancy properties of new halogen-free phosphorous doped SiO_2 thin films on fabrics. *Journal of Applied Polymer Science* **2007**, *105*, 3748–3756.

[121] Yaman, N. Preparation and flammability properties of hybrid materials containing phosphorous compounds via sol-gel process. *Fibers and Polymers* **2009**, *10*, 413–418.

[122] Brancatelli, G.; Colleoni, C.; Massafra, M.; Rosace, G. Effect of hybrid phosphorus-doped silica thin films produced by sol-gel method on the thermal behavior of cotton fabrics. *Polymer Degradation and Stability* **2011**, *96*, 483 – 490.

[123] Anastasescu, M.; Gartner, M.; Ghita, A.; Predoana, L.; Todan, L.; Zaharescu, M.; Vasiliu, C.; Grigorescu, C.; Negrila, C. Loss of phosphorous in silica-phosphate sol-gel films. *Journal of Sol-Gel Science and Technology* **2006**, *40*, 325–333.

[124] Livage, J.; Barboux, P.; Vandenborre, M.; Schmutz, C.; Taulelle, F. Sol-gel synthesis of phosphates. *Journal of Non-Crystalline Solids* **1992**, *147-148*, 18 – 23, Advanced Materials from Gels Proceedings of the Sixth International Workshop on Glasses and Ceramics from Gels.

[125] Fernandez-Lorenzo, C.; Esquivias, L.; Barboux, P.; Maquet, J.; Taulelle, F. Sol-gel synthesis of SiO_2-P_2O_5 glasses. *Journal of Non-Crystalline Solids* **1994**, *176*, 189 – 199.

[126] Szu, S.-P.; Klein, L.; Greenblatt, M. Effect of precursors on the structure of phosphosilicate gels: ^{29}Si and ^{31}P MAS-NMR study. *Journal of Non-Crystalline Solids* **1992**, *143*, 21–30.

[127] Clayden, N. J.; Esposito, S.; Pernice, P.; Aronne, A. Solid state ^{2}9Si and ^{3}1P NMR study of gel derived phosphosilicate glasses. *J. Mater. Chem.* **2001**, *11*, 936–943.

[128] Snedaker, M. L.; Zhang, Y.; Birkel, C. S.; Wang, H.; Day, T.; Shi, Y.; Ji, X.; Kraemer, S.; Mills, C. E.; Moosazadeh, A.; Moskovits, M.; Snyder, G. J.; Stucky, G. D. Silicon-Based Thermoelectrics Made from a Boron-Doped Silicon Dioxide Nanocomposite. *Chemistry of Materials* **2013**, *25*, 4867–4873.

[129] Liu, Y.; Liu, X. H.; Nguyen, B.-M.; Yoo, J.; Sullivan, J. P.; Picraux, S. T.; Huang, J. Y.; Dayeh, S. A. Tailoring Lithiation Behavior by Interface and Bandgap Engineering at the Nanoscale. *Nano Letters* **2013**, *13*, 4876–4883, PMID: 24000810.

[130] Ji, X.; He, G.; Andrei, C.; Nazar, L. F. Gentle reduction of SBA-15 silica to its silicon replica with retention of morphology. *RSC Adv.* **2014**, *4*, 22048–22052.

[131] Craig, B.; Anderson, D.; International, A. *Handbook of Corrosion Data*; Materials data series; ASM International, 1994.

[132] Szczech, J. R.; Lukowski, M. A.; Jin, S. Synthesis of mesoporous $Si_{1-x}Ge_xO_2$ ($0.10 \leq \times \leq 0.31$) using a nonionic block copolymer template. *J. Mater. Chem.* **2010**, *20*, 8389–8393.

[133] Richman, E. K.; Kang, C. B.; Brezesinski, T.; Tolbert, S. H. Ordered Mesoporous Silicon through Magnesium Reduction of Polymer Templated Silica Thin Films. *Nano Letters* **2008**, *8*, 3075–3079, PMID: 18702552.

[134] Dennis, L. M.; Tressler, K. M.; Hance, F. E. GERMANIUM.1 VI. METALLIC GERMANIUM. REDUCTION OF GERMANIUM DIOXIDE. PREPARATION OF FUSED GERMANIUM. PHYSICAL AND CHEMICAL PROPERTIES. *Journal of the American Chemical Society* **1923**, *45*, 2033–2047.

[135] Dismukes, J. P.; Ekstrom, L.; Paff, R. J. Lattice Parameter and Density in Germanium-Silicon Alloys. *The Journal of Physical Chemistry* **1964**, *68*, 3021–3027.

[136] Ausserer, W. A.; Ling, Y. C.; Chandra, S.; Morrison, G. H. Quantitative imaging of boron, calcium, magnesium, potassium, and sodium distributions

in cultured cells with ion microscopy. *Analytical Chemistry* **1989**, *61*, 2690–2695, PMID: 2619055.

[137] Slack, G. A.; Hussain, M. A. The maximum possible conversion efficiency of silicon-germanium thermoelectric generators. *Journal of Applied Physics* **1991**, *70*, 2694–2718.

[138] Vining, C. B.; Laskow, W.; Hanson, J. O.; Van der Beck, R. R.; Gorsuch, P. D. Thermoelectric properties of pressure-sintered $Si_{0.8}Ge_{0.2}$ thermoelectric alloys. *Journal of Applied Physics* **1991**, *69*, 4333–4340.

[139] Minnich, A. J.; Lee, H.; Wang, X.; Joshi, G.; Dresselhaus, M.; Ren, Z.; Chen, G.; Vashaee, D. Modeling study of thermoelectric SiGe nanocomposites. *Phys. Rev. B* **2009**, *80*, 155327.

[140] Amano, T.; Beaudry, B. J.; Gschneidner, K. A.; Hartman, R.; Vining, C. B.; Alexander, C. A. High-temperature heat contents, thermal diffusivities, densities, and thermal conductivities of n-type SiGe(GaP), p-type SiGe(GaP), and p-type SiGe alloys. *Journal of Applied Physics* **1987**, *62*, 819–823.

[141] Steigmeier, E.; Abeles, B. Scattering of Phonons by Electrons in Germanium-Silicon Alloys. *Phys. Rev.* **1964**, *136*, A1149–A1155.

[142] LaLonde, A. D.; Ikeda, T.; Snyder, G. J. Rapid consolidation of powdered materials by induction hot pressing. *Review of Scientific Instruments* **2011**, *82*, 025104.

[143] Tokita, M. Mechanism of Spark Plasma Sintering and its application to ceramics. *Nyn Seramikkasu* **1997**, *10*, 43–53.

[144] Garay, J. Current-Activated, Pressure-Assisted Densification of Materials. *Annual Review of Materials Research* **2010**, *40*, 445–468.

[145] Birkel, C. S.; Douglas, J. E.; Lettiere, B. R.; Seward, G.; Verma, N.; Zhang, Y.; Pollock, T. M.; Seshadri, R.; Stucky, G. D. Improving the thermoelectric properties of half-Heusler TiNiSn through inclusion of a second full-Heusler phase: microwave preparation and spark plasma sintering of $TiNi_{1+x}Sn$. *Phys. Chem. Chem. Phys.* **2013**, *15*, 6990–6997.

[146] Kieslich, G.; Birkel, C. S.; Douglas, J. E.; Gaultois, M.; Veremchuk, I.; Seshadri, R.; Stucky, G. D.; Grin, Y.; Tremel, W. SPS-assisted preparation of the Magneli phase $WO_{2.90}$ for thermoelectric applications. *J. Mater. Chem. A* **2013**, *1*, 13050–13054.

[147] Kieslich, G.; Burkhardt, U.; Birkel, C. S.; Veremchuk, I.; Douglas, J. E.; Gaultois, M. W.; Lieberwirth, I.; Seshadri, R.; Stucky, G. D.; Grin, Y.; Tremel, W. Enhanced thermoelectric properties of the n-type Magneli phase $WO_{2.90}$: reduced thermal conductivity through microstructure engineering. *J. Mater. Chem. A* **2014**, *2*, 13492–13497.

[148] Yamini, S. A.; Ikeda, T.; Lalonde, A.; Pei, Y.; Dou, S. X.; Snyder, G. J. Rational design of p-type thermoelectric PbTe: temperature dependent sodium solubility. *J. Mater. Chem. A* **2013**, *1*, 8725–8730.

[149] Klemens, P. Thermal conductivity of inhomogeneous materials. *International Journal of Thermophysics* **1989**, *10*, 1213–1219.

[150] Klemens, P. Electrical resistivity of inhomogeneous alloys. *Journal of Applied Physics* **1991**, *70*, 4322–4325.

[151] Klemens, P. Thermal conductivity of inhomogeneous media. *High Temperature - High Pressures* **1991**, *23*, 241–248.

[152] Birkel, C. S.; Zeier, W. G.; Douglas, J. E.; Lettiere, B. R.; Mills, C. E.; Seward, G.; Birkel, A.; Snedaker, M. L.; Zhang, Y.; Snyder, G. J.; Pollock, T. M.; Seshadri, R.; Stucky, G. D. Rapid Microwave Preparation of Thermoelectric TiNiSn and TiCoSb Half-Heusler Compounds. *Chemistry of Materials* **2012**, *24*, 2558–2565.

[153] Brgoch, J.; Borg, C. K.; Denault, K. A.; Douglas, J. R.; Strom, T. A.; DenBaars, S. P.; Seshadri, R. Rapid microwave preparation of cerium-substituted sodium yttrium silicate phosphors for solid state white lighting. *Solid State Sciences* **2013**, *26*, 115 – 120.

[154] Brgoch, J.; Kloß, S. D.; Denault, K. A.; Seshadri, R. Accessing $(Ba_{1-x}Sr_x)Al_2Si_2O_8$:Eu Phosphors for Solid State White Lighting via Microwave-assisted Preparation: Tuning Emission Color by Coordination Environment. *Zeitschrift fur anorganische und allgemeine Chemie* **2014**, *640*, 1182–1189.

[155] Misch, L. M.; Brgoch, J.; Birkel, A.; Mates, T. E.; Stucky, G. D.; Seshadri, R. Rapid Microwave Preparation and ab Initio Studies of the Stability of the Complex Noble Metal Oxides La_2BaPdO_5 and La_2BaPtO_5. *Inorganic Chemistry* **2014**, *53*, 2628–2634, PMID: 24517630.

[156] Birkel, C. S.; Lettiere, B. R. Unpublished data, 2012.

[157] Nohira, T.; Yasuda, K.; Ito, Y. Pinpoint and bulk electrochemical reduction of insulating silicon dioxide to silicon. *Nature Materials* **2003**, *2*, 397–401.

[158] Yasuda, K.; Nohira, T.; Takahashi, K.; Hagiwara, R.; Ogata, Y. H. Electrolytic Reduction of a Powder-Molded SiO_2 Pellet in Molten $CaCl_2$ and Acceleration of Reduction by Si Addition to the Pellet. *Journal of The Electrochemical Society* **2005**, *152*, D232–D237.

[159] Liu, X.; Giordano, C.; Antonietti, M. A molten-salt route for synthesis of Si and Ge nanoparticles: chemical reduction of oxides by electrons solvated in salt melt. *J. Mater. Chem.* **2012**, *22*, 5454–5459.

[160] Liu, X. private communication, 2014.

[161] Elchardus, E.; Laffitte, P. The KCl–LiCl system. *Bull. soc. chim. France* **1932**, *65*, 406.

[162] Klemm, W.; Weiss, P. The NaCl–$MgCl_2$ System. *Z. Anorg. Allg. Chem.* **1940**, *245*, 281.

[163] Luo, W.; Wang, X.; Meyers, C.; Wannenmacher, N.; Sirisaksoontorn, W.; Lerner, M. M.; Ji, X. Efficient Fabrication of Nanoporous Si and Si/Ge Enabled by a Heat Scavenger in Magnesiothermic Reactions. *Scientific Reports* **2013**, *3*, 1–7.

[164] Takamori, T.; Messier, R.; Roy, R. New Noncrystalline Germanium which Crystallizes “Explosively"; at Room Temperature. *Applied Physics Letters* **1972**, *20*, 201–203.

[165] Fan, J. C. C.; Zeiger, H. J.; Gale, R. P.; Chapman, R. L. Solid-phase growth of large aligned grains during scanned laser crystallization of amorphous Ge films on fused silica. *Applied Physics Letters* **1980**, *36*, 158–161.

[166] Aydinli, A.; Berti, M.; Drigo, A. V.; Lotti, R.; Merli, P. G. Explosive crystallization of dilute amorphous Si–Ge alloys. *Journal of Applied Physics* **1988**, *64*, 3301–3303.

[167] Fan, J. C.; Anderson, C. H. Transition temperatures and heats of crystallization of amorphous Ge, Si, and $Ge_{1-x}Si_x$ alloys determined by scanning calorimetry. *Journal of Applied Physics* **1981**, *52*, 4003–4006.

[168] Auston, D. H.; Surko, C. M.; Venkatesan, T. N. C.; Slusher, R. E.; Golovchenko, J. A. Time-resolved reflectivity of ion-implanted silicon during laser annealing. *Applied Physics Letters* **1978**, *33*, 437–440.

[169] Baeri, P.; Rimini, E. Laser annealing of silicon. *Materials Chemistry and Physics* **1996**, *46*, 169 – 177.

[170] Sera, K.; Okumura, F.; Uchida, H.; Itoh, S.; Kaneko, S.; Hotta, K. High-performance TFTs fabricated by XeCl excimer laser annealing of hydrogenated amorphous-silicon film. *Electron Devices, IEEE Transactions on* **1989**, *36*, 2868–2872.

[171] Nickel, N. *Laser Crystallization of Silicon - Fundamentals to Devices*; Semiconductors and semimetals; Elsevier Science, 2003.

[172] Shi, Y. Unpublished data, 2009.

[173] Orton, J. W.; Powell, M. J. The Hall effect in polycrystalline and powdered semiconductors. *Reports on Progress in Physics* **1980**, *43*, 1263.

[174] Ohgaki, T.; Ohashi, N.; Sugimura, S.; Ryoken, H.; Sakaguchi, I.; Adachi, Y.; Haneda, H. Positive Hall coefficients obtained from contact misplacement on evident n-type ZnO films and crystals. *Journal of Materials Research* **2008**, *23*, 2293–2295.

[175] Ko, D.-K.; Kang, Y.; Murray, C. B. Enhanced Thermopower via Carrier Energy Filtering in Solution-Processable Pt-Sb_2Te_3 Nanocomposites. *Nano Letters* **2011**, *11*, 2841–2844.

[176] Zhang, Y.; Snedaker, M. L.; Birkel, C. S.; Mubeen, S.; Ji, X.; Shi, Y.; Liu, D.; Liu, X.; Moskovits, M.; Stucky, G. D. Silver-Based Intermetallic Heterostructures in Sb_2Te_3 Thick Films with Enhanced Thermoelectric Power Factors. *Nano Letters* **2012**, *12*, 1075–1080.

[177] Zhang, Y.; Bahk, J.-H.; Lee, J.; Birkel, C. S.; Snedaker, M. L.; Liu, D.; Zeng, H.; Moskovits, M.; Shakouri, A.; Stucky, G. D. Hot Carrier Filtering in Solution Processed Heterostructures: A Paradigm for Improving Thermoelectric Efficiency. *Advanced Materials* **2014**, *26*, 2755–2761.

[178] Sztein, A. Unpublished data, 2013.

[179] Wei, Q.; Mukaida, M.; Naitoh, Y.; Ishida, T. Morphological Change and Mobility Enhancement in PEDOT:PSS by Adding Co-solvents. *Advanced Materials* **2013**, *25*, 2831–2836.

[180] Coates, N. E.; Yee, S. K.; McCulloch, B.; See, K. C.; Majumdar, A.; Segalman, R. A.; Urban, J. J. Effect of Interfacial Properties on Polymer-Nanocrystal Thermoelectric Transport. *Advanced Materials* **2013**, *25*, 1629–1633.

[181] Yee, S. K.; Coates, N. E.; Majumdar, A.; Urban, J. J.; Segalman, R. A. Thermoelectric power factor optimization in PEDOT:PSS tellurium nanowire hybrid composites. *Phys. Chem. Chem. Phys.* **2013**, *15*, 4024–4032.

[182] Park, G. O.; Roh, J. W.; Kim, J.; Lee, K. Y.; Jang, B.; Lee, K. H.; Lee, W. Enhanced thermoelectric properties of germanium powder/poly(3,4-ethylenedioxythiophene):poly(4-styrenesulfonate) composites. *Thin Solid Films* **2014**, *566*, 14 – 18.

[183] Sakamoto, S.; Okumura, M.; Zhao, Z.; Furukawa, Y. Raman spectral changes of PEDOT:PSS in polymer light-emitting diodes upon operation. *Chemical Physics Letters* **2005**, *412*, 395 – 398.

[184] Garreau, S.; Louarn, G.; Buisson, J. P.; Froyer, G.; Lefrant, S. In Situ Spectroelectrochemical Raman Studies of Poly(3,4-ethylenedioxythiophene) (PEDT). *Macromolecules* **1999**, *32*, 6807–6812.

[185] Wong, K. T.; Chopra, S. N.; Bent, S. F. Dissociative Adsorption of Dimethyl Sulfoxide at the Ge(100)-2 $\times$ 1 Surface. *Journal of Physical Chemistry C* **2012**, *116*, 26422–26430.

[186] Shi, Y. Unpublished data, 2009.

[187] Jennings, H. M.; Richman, M. H. A Hexagonal (Wurtzite) Form of Silicon. *Science* **1976**, *193*, 1242–1243.

[188] Fabbri, F.; Rotunno, E.; Lazzarini, L.; Fukata, N.; Salviati, G. Visible and Infra-red Light Emission in Boron-Doped Wurtzite Silicon Nanowires. *Scientific Reports* **2013**, *4*, 1–7.

[189] Fabbri, F.; Rotunno, E.; Lazzarini, L.; Cavalcoli, D.; Castaldini, A.; Fukata, N.; Sato, K.; Salviati, G.; Cavallini, A. Preparing the Way for Doping Wurtzite Silicon Nanowires while Retaining the Phase. *Nano Letters* **2013**, *13*, 5900–5906, PMID: 24224918.

[190] Kim, D.; Stefanoski, S.; Kurakevych, O. O.; Strobel, T. A. Synthesis of an open-framework allotrope of silicon. *Nature Materials* **2014**, *4140*, 1–5.

[191] Bergman, D.; Levy, O. Thermoelectric properties of a composite medium. *Journal of Applied Physics* **1991**, *70*, 6821–6833.

[192] Landauer, R. In *Electrical Transport and Optical Properties of Inhomogeneous Media*; Landauer, R., Ed.; American Institute of Physics: New York City, New York, 1978; pp. 2–45.